RF-Bracket Design

Mass reduction of a mechanical bracket by redesigning the bracket without compromising on thermal, structural and EMC aspects

R.M.J. Caenen 4011872

Master Thesis

Report

TU Delft Delft University of Technology

Aerospace Engineering

March 16, 2018

RF-BRACKET DESIGN

MASS REDUCTION OF A MECHANICAL BRACKET BY REDESIGNING THE BRACKET WITHOUT COMPROMISING ON THERMAL, STRUCTURAL AND EMC ASPECTS

by

R.M.J. Caenen

Master Thesis

at Delft University of Technology

Mentor:	ing. J.F. Zwart	SRON - Engineering
Mentor:	ing. J.B. van Schaijk	SRON - Engineering
Supervisor:	Dr. A. Menicucci	TU Delft - Space Systems Engineering

TU Delft Delft University of Technology

PREFACE

This preface is more than just the last piece of my master thesis, it marks the ending of years of study at the Delft University of Technology. During this period I have not only increased my technical skills, but more importantly, I have grown as a person. Finishing this thesis feels great and rewarding, but it also ends an amazing period of my life.

Regarding this thesis, I would like to thank my supervisor Alessandra for guidance, support and feedback on my activities. Furhtermore, I would like to thank my mentors at SRON; Frans and Jan. Their enthusiastic coaching, feedback and hands on design approach pushed my at times when I needed it. Another word of thanks is for Rob, who helped me with the thermal testing and modelling.

Most importantly, I would like to thank my family and friends for their unconditional support, and for making my student time incredible.

SUMMARY

SRON Netherlands Insitute for Space Research, is developing a new superconducting infrared photon detector called Microwave Kinetic Inductance Detector (MKID). The MKID architecture exists of digital electronics, Radio Frequency (RF) electronics and a MKID array operated at 100 mK [1]. For this project, the interest lies in the RF electronics which consist of a single multilayer Printed Circuit Board (PCB) and a supporting bracket. With a current mass of 920 g, the supporting bracket is too heavy for space applications. The main goal of the project is identified as the mass reduction of the mechanical bracket without compromising on performance aspects.

In chapter 2 an analysis is made of the thermo-elastic effects in the structure. A mismatch between the CTE of the PCB and the CTE of the mechanical bracket, cause a curvature of the entire board. To analyse this CTE mismatch effect, Timoshenko's theory [2] is used to determine the deflection of two bonded strips with materials. Simple test showed that Timoshenko's model can be used to predict the deflection. An extension to Timoshenko's theory is made by Chen [3], who determines the normal and shear stress in the solder layer. This analysis showed that stress concentrations are to be expected at both ends of the strip.

The next chapter, chapter 3, presents a model of the thermal heat transfer of the LO board. The LO board is chosen as analysis case, because a lighter aluminum bracket was already designed for this board. The LO board is divided into nodes, and for each node the conduction, convection and radiation heat flows are defined. This heat transfer model is validated by test and can be used to predict the temperature distribution over the LO board, with an accuracy of $\pm 3\ ^{\circ}C$.

Chapter 4 focuses on the material selection for electronic packaging. The by industry frequently used metal alloys and new advanced composites are analyzed on their material performance. The material performance is analyzed using the deflection, solder layer stress and thermal heat transfer models. From this, a numerical trade off is made showing that aluminum, aluminum silicon and aluminum silicon carbide would perform best. A graphical trade off, which also includes manufacturing aspects, is performed on these materials. This graphical trade-off showed that aluminum silicon is the most promising material for electronic packaging.

The next step is to design a bracket for the 2-4 GHz board, which is done in chapter 5. The bracket, which will be made of aluminum silicon, will be optimized for its mass. While doing so, the temperature of components, EMC resonances, manufacturing and assembly aspects need to be taken into account. The final design has a mass of 74 g. The bracket will be soldered to the PCB, and this assembly will be subjected to a thermal test to verify that the thermal performance is as expected. This test showed that the predicted temperatures are typically 4 $^{\circ}C$ lower than the measured temperatures.

NOMENCLATURE

ABBREVIATIONS

Abbreviation	*Description*
AHP	Analytical Hierarchy Process
Al	Aluminum
CI	Critical Index
CR	Critical Ratio
CTE	Coefficient of Thermal Expansion
Cu	Copper
DAC	Digital-Analog Converter
ECSS	European Cooperation for Space Standardization
EMC	Electromagnetic Compatibility
EMI	Electomagnetic Interference
ESA	European Space Agency
FEM	Finite Element Method
LO	Local Oscilator
Mg	Magnesium
MKID	Microwave Kinetic Inductance Detector
MMCs	Metal Matrix Composites
Mo	Molybdenum
PCB	Printed Circuit Board
RF	Radio Frequency
RI	Random Index
Si	Silicon
SiC	Silicon Carbide
Ti	Titanium

CONTENTS

1

INTRODUCTION

1.1. RESEARCH CONTEXT

SRON is a space research institute that aims to design and develop world-class innovative space instruments for astrophysical, earth-oriented and exoplanet research and to analyze the data obtained by these instruments for advanced research [4]. SRON scientists and engineers have developed a new superconducting infrared photon detector called Microwave Kinetic Inductance Detector (MKID) with electrical readout frequencies in the 2-4 GHz range. The MKID architecture exists of digital electronics, Radio Frequency (RF) electronics and a MKID array operated at 100 mK [1]. More information on the working principle of the MKID can be found in appendix A.

For this project, the interest lies in the RF electronics which consist of a single multilayer Printed Circuit Board (PCB) and a supporting bracket. The PCB contains several electronic blocks, including a power block, several amplifiers, several mixers and an oscillation splitter [1]. This PCB board is supported by a gold plated copper bracket, which is fully soldered to the PCB. Soldering the bracket to the PCB is a new and promising design concept, which will be developed over the coming years. The mechanical bracket provides structural integrity, thermal conduction and electromagnetic interference shielding. Figure 1.1 shows a picture of the integrated RF electronics.

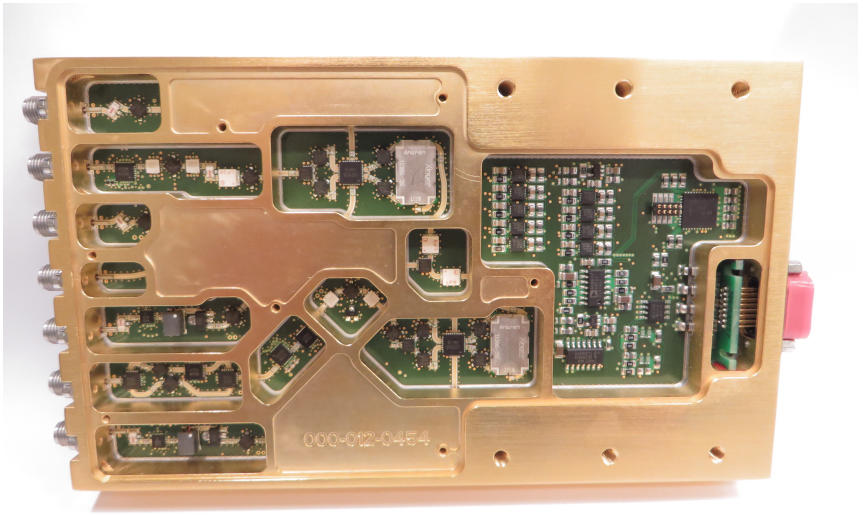

Figure 1.1: A picture of the current RF electronics.

The current mechanical bracket is recognized to be too heavy for space applications, thus the next step in the development of this RF-board is to design a lighter, more flight ready version. As the mass of the RF-board is mainly made up by the gold platted copper bracket, the mass reduction of the mechanical bracket will be central in this thesis.

1.2. RESEARCH QUESTIONS

With a current mass of 920 g, the supporting bracket is too heavy for space applications. The main goal of the project is identified as the mass reduction of the mechanical bracket without compromising on performance aspects, which leads to the following research objective:

The research objective is to improve the current design of the RF-system by redesigning the mechanical bracket to significantly reduce its mass, while keeping similar performance with respect to the current bracket design.

To achieve this objective, the main research question is defined as:

How much mass reduction can be achieved by redesigning the mechanical bracket without compromising on structural, thermal and electromagnetic compatibility performance?

To answer the main research question, several sub-questions are formulated:

- *What is the effect of a CTE mismatch between bracket and PCB?*
- *What is the impact of the mechanical bracket on the thermal housekeeping?*
- *Which material is best suited for the mechanical bracket?*
- *Which electromagnetic compatibility aspects influence the design of the mechanical bracket?*
- *How can all design aspects be incorporated in the structural design of a low mass mechanical bracket?*

1.3. DESIGN APPROACH

As the disciplines of thermal design, structural design and Electromagnetic Compatibility (EMC) design are very complex, performing a proper analysis for each discipline within the time span of this project would be extremely hard. Due to the time restrictions on a thesis project, it was decided to focus on the thermal design of the bracket, and were possible to include aspects of the structural and EMC design.

The thermal design covers two main areas; the bending due to the mismatch in Coefficient of Thermal Expansion (CTE) between materials, and the thermal heat transfer of the PCB to maintain the electrical components within acceptable limits. The CTE mismatch, presented in chapter 2, includes two analytical models, one for the deflection due to bending which will be validated by a test, and one for the solder layer stresses which will be verified by a FEM model. Chapter 3 shows the analysis of the heat transfer of a PCB the Local Oscillator (LO) board is used. This is an already existing board with an aluminum bracket, which will be used to built and validate the heat transfer model.

These thermal models are used to evaluate the performance of different materials in chapter 4. During a literature review the thermal and EMC performance of different advanced materials with possible space applications were studied. A selection of these materials are now evaluated for possible applications in the bracket design. A pre-selection of these materials is made using a trade-off on material performance. After this, a second and final trade-off based on the manufacturability, reworkability and risk is made to select the final material.

Chapter 5 presents the last step in the project; the design of the RF-bracket. The thermal heat transfer model of the LO board is adjusted such that it meets the specifications of the 2-4 GHz board. With the material known, this thermal model can be optimized for the lowest mass. While performing this optimization, other aspects such as EMC performance, manufacturing and assembly aspects are included in the design. This design will be checked by mechanical, electrical and assembly engineers. The mechanical bracket will be manufactured externally. When the bracket returns, it will be soldered to a PCB and tested for its thermal performance.

2

CTE ANALYSIS

An important structural aspect of the bracket design will be the Coefficient of Thermal Expansion (CTE) mismatch between the bracket and PCB. This mismatch in CTE will cause visual deformation, in the form of bending and twisting, of the PCB assembly. Besides the deformation, a CTE mismatch will cause pre-stresses in the solder layer. Such pre-stresses decrease the amount of (thermal and/or vibrational) load cycles the PCB assembly can handle, and are therefore undesired. This chapter will present models which can predict the deflections and solder layer stresses generated by CTE mismatches.

2.1. DEFLECTION MODEL

2.1.1. MODEL DESCRIPTION

The analysis of the deflection of a strip containing two bonded materials, with different CTE, is based on the analysis of Timoshenko [2]. This analysis contains a general theory of bending on a bi-metal strip submitted to uniform heating. The theory is based on several ideal conditions, such as a constant CTE of the materials during heating, friction at the supports can be neglected and the width of the strip is considered to be very small when compared to the length of the strip. In the analysis, this width is taken to be unity.

The model is for a narrow strip of two metals which are bonded together and is uniformly heated. The difference in CTE between the two metals will let the strip experience bending, as can be seen in figure 2.1.

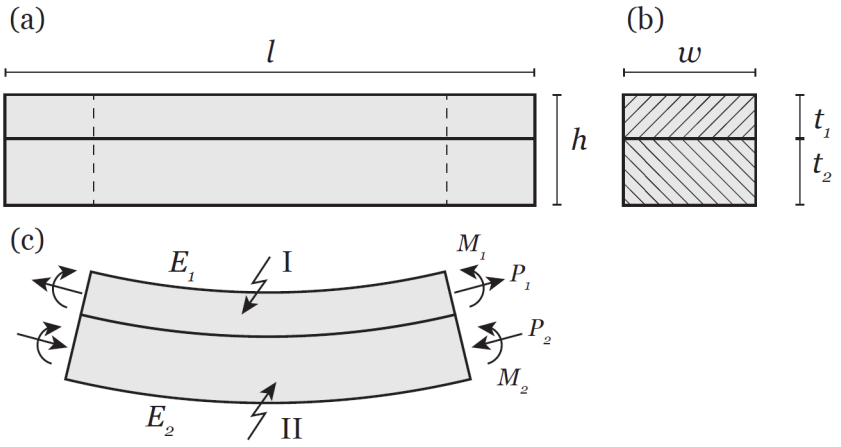

Figure 2.1: Deflection of a bi-metal strip while uniformly heated. [2]

Applying force and moment equilibrium to this problem, in combination with the unit elongation at the bearing surface of each layer results in an expression for the radius of curvature ρ [m]. The equation for the radius of curvature is shown in 2.1, the entire derivation of this equation can be found in appendix B.1.

$$\frac{1}{\rho} = \frac{6(\alpha_2 - \alpha_1)(1+m)^2 \Delta T}{h\left(3(1+m)^2 + (1+mn)\left(m^2 + \frac{1}{mn}\right)\right)} \tag{2.1}$$

With constants:

$$m = \frac{t_1}{t_2}, n = \frac{E_1}{E_2} \tag{2.2}$$

In these equations the CTE is represented by α [$1/K$], the temperature difference by ΔT [K], the total thickness of the bonded strips h [m], the thickness of each layer t [m] and the Young's modulus E [MPa]. The subscripts 1 and 2 refer to layer 1 and layer 2 respectively.

The next step is to convert this radius of curvature to a deflection of the bonded strip. Figure 2.2 depicts the bending of the bonded strip.

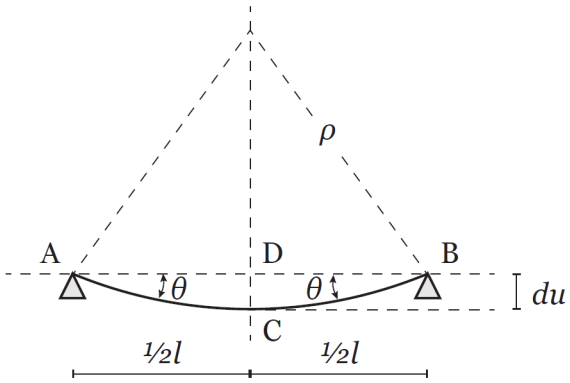

Figure 2.2: Deflection of a strip. [2]

The deflection of the strip will be small when compared to the length of the strip. Therefore the small angle approximation is applied, which assumes that the arc length of the strip is equal to the horizontal length of the strip. With this assumption, the deflection du [m] can be determined by equation 2.3.

$$du = \rho - \sqrt{\rho^2 - l^2} \tag{2.3}$$

2.1.2. MODEL RESULTS

To validate the model presented above, several strips of copper and aluminum will be soldered together. Copper and aluminum are chosen because of the in-house availability at SRON and because of the known material properties: the E-modulus of copper is 118 GPa and CTE is 16.8 ppm/K [5], aluminum has an E-modulus of 68.9 GPa and CTE 23.6 ppm/K [6]. The copper strips have a thickness of 1 or 2 mm, and the aluminum strips have thicknesses of 1.5, 3 or 5 mm. This results in a total of 6 different bonded strips. The eutectic soldering temperature is 183 $^{\circ}C$, details on the soldering process are described in section 2.1.3. The deflection du is determined in the middle of the strip, which gives the maximum deflection. Table 2.1 shows the predicted deflection results for these 6 bonded strips.

Table 2.1: Model results

Al [mm]	Cu [mm]	du [mm]
1.5	1	2.19
3	1	1.20
5	1	0.66
1.5	2	1.42
3	2	1.09
5	2	0.72

2.1.3. TEST SETUP

The copper and aluminum strips are cut from large sheets of material. The length of these strokes is 15 cm and the width 1 cm. Thus cutting results in slightly bent and twisted strips. After the cutting, the strokes are sent to an external company to receive nickel and gold plating. The by the cutting induced bending and twisting of the strip is manually removed before soldering.

The solder paste is applied using a stencil creating a solder paste thickness of 130 μm. The solder material is 63Sn37Pb, which consists of 63% tin and 37% lead, and has an eutectic solder temperature of 183 $^{\circ}C$. Soldering this solder directly to the gold layer would cause a very fragile solder layer. To prevent this, the gold layer is pre-tinned. This process causes the gold to dissolve into the tin, creating an intermetallic layer. The solder can attach to this intermetallic layer nicely, creating a robust connection.

The soldering takes place in a vapour phase reflow oven. At the bottom of the oven, a liquid is heated to its boiling point of 215 $^{\circ}C$. This creates a vapour of 215 $^{\circ}C$ which will rise in the oven. When this heated vapour reaches the strips, it will start to uniformly heat up the strips. After the strips have reached the 215$^{\circ}C$ temperature, the vapour will rise again. At the top of the oven the temperature is measured, when this measurement shows 215 $^{\circ}C$ the entire oven is heated and will be shut down. The vapour and liquid will slowly cool down back to room temperature. During this cooling down, at exactly 183 $^{\circ}C$, the solder will solidify and form the solder layer.

After soldering, six strips of soldered copper and aluminum remain. The thicknesses correspond with table 2.1. To measure the deflection, a dial indicator is used. The strips are placed on a workbench, with the deflection pointing upwards. The dial indicator is calibrated at 0 mm at the sides. The strip is then moved such that the dial indicator can measure the deflection, as can be seen in figure 2.3.

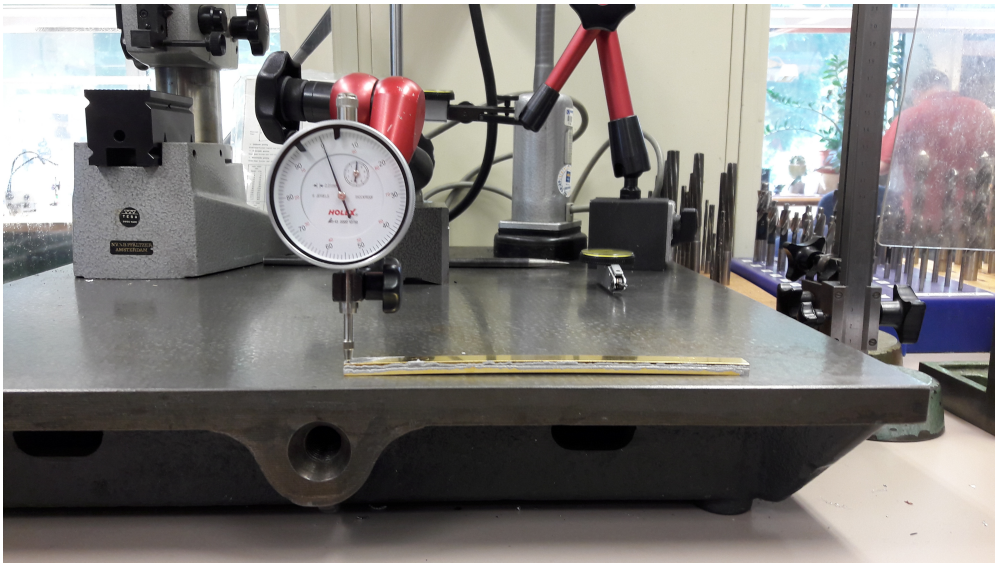

Figure 2.3: Deflection measurements.

2.1.4. TEST RESULTS

The strips of copper and aluminum are solder together according to the test setup explained above. The deflection of these strips, combined with the model predictions, are given in table 2.2. This is followed by a discussion on the differences between the model and test results, and an analysis of the test results.

Table 2.2: Model results

Al [mm]	Cu [mm]	Model: du [mm]	Test: du [mm]
1.5	1	2.19	2.00
3	1	1.20	1.40
5	1	0.66	0.59
1.5	2	1.42	1.36
3	2	1.09	0.99
5	2	0.72	0.70

DIFFERENCES MODEL AND TEST

The deflection model, but also the joint-stress model presented later in this chapter, can not account for several processes occurring during the manufacturing and soldering of the strips. Therefore, the test results will not match the model predictions exactly.

For the deflection test, the largest uncertainty is due to the manufacturing of the strips. The manufacturing process yielded slightly bent and twisted strips, which were manually removed. However, this will not result in perfectly straight strips which is assumed in the model. The difference between the model and test results is on the sub-mm scale, which is an accuracy that can not be achieved by manual removal of the induced bending and twist.

During the soldering, several other processes occur which are not accounted for in the model. The solder paste is applied with a stencil with a thickness of 130 μm. However this solder paste still contains a lot of air. When the solder reaches a temperature of 183 $^{\circ}C$, several processes start. The air contained in the stencil will disappear from the solder layer. This escaping air decreases the thickness of the solder layer, and it can cause voids in the solder layer. This means that the strips are not attached over the entire surface. Besides the escaping air, the solder itself will start to flow when liquidized. This causes some of the solder to attach

at the sides of the strips (this effect can be seen in figure 2.3). Therefore, the exact thickness of the solder paste stencil is known but the exact thickness of the actual solder layer is unknown. Also the thickness of this solder layer is not constant over the length of the strip. The solder is still slightly deformable around the solder temperature, thus the bending of the strip forces the solder towards the sides. This causes a slightly thicker layer at the ends of the strip.

The model is for a pure 2D bending case, which is not the case in the test. The difference between the 2D model and 3D test introduces several small errors. The test strips have a width of 1 cm which introduces twist. The effect of this twist should be minimal, because the length of the strip is much larger than the width. Also, the flowing of the solder introduces another effect. The strip laying on top of this flowing solder, will not keep its original position above the bottom layer due to the movement of the solder. The strips are therefore not exactly aligned when they are bonded, although this effect will be minimal. All these differences, including the manufacturing and soldering uncertainties, will cause the maximum bending of the strip not to be exactly in the middle of the strip.

DEFLECTION TEST ANALYSIS

The test showed that the deflection is directed upwards when the copper layer is on top. Which, at first, seems contradictory because the CTE of copper is lower than the CTE of aluminum. When heated, the aluminum will expand more and should thus be the top layer when the deflection is directed upwards. This is still true, however, the starting point for the deflection is in this case not at room temperature. When the copper strip, aluminum strip and solder are heated in the oven the copper and aluminum strip will expand individually, because they are not bonded yet. The bonding process, the soldering, happens at 183 $^{\circ}C$. This is the starting point were no deflection and solder layer stresses are present. When cooled to room temperature, the strips will start to bend. Due to the higher CTE of aluminum, the aluminum layer will contract more during cooling. This yields that the deflection will be in upward direction with the copper layer on top.

Table 2.2 indicates that the combined thickness and the height ratio of the different layers determine the maximum deflection. If the combined thickness is larger, the deflection decreases. Thicker strips have a larger moment of inertia, and are thus more resilient to bending. This holds true for the 'thinner' strips. However, when one strip is significantly larger than the other, the height ratio becomes more important. Looking at the deflection of the 5 mm Al with 1 and 2 mm Cu strips, one can see that for the 1 mm Cu strip the deflection is smaller. This shows that for larger height ratios, the thicker layer becomes more dominant.

2.2. STRESS IN JOINT MODEL

2.2.1. MODEL DESCRIPTION

An extension to the Timoshenko theory is provided by Chen [3]. This extension determines the normal and shear stress in a joint between the layers of the strip. Chen's theory will be used to determine the stresses in the joint. Chen considers the case where the layers are separated by an amount η. This gap is filled with a material capable of deforming under shear and tension, figure 2.4 shows the model.

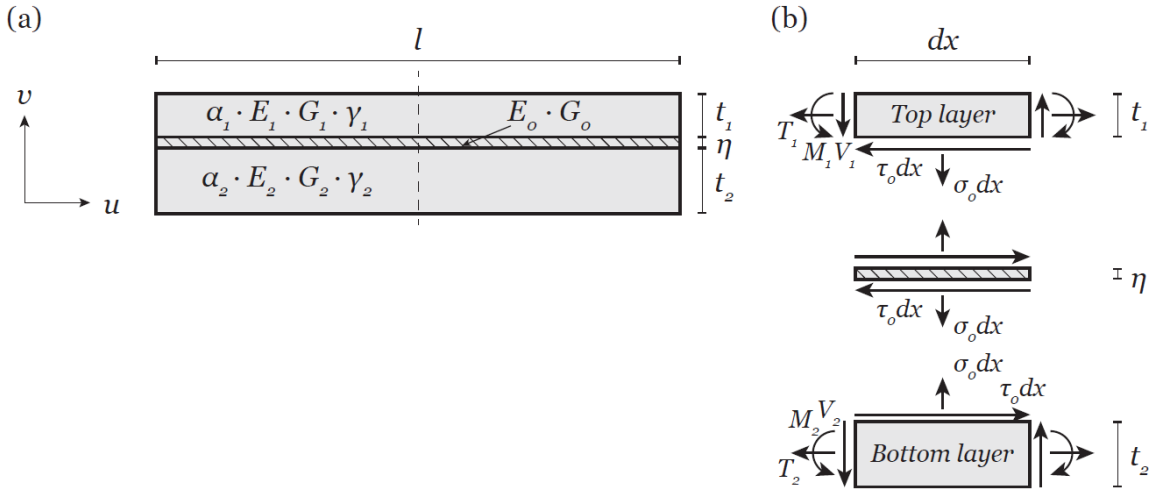

Figure 2.4: (a) Chen's model setup. (b) The forces and moments acting on each a section dx. (c) The applicable axis system. [3]

Chen's model can be used to find expressions for the normal stress σ_0 $[MPa]$ and the shear stress τ_0 $[MPa]$ in the solder layer. The derivation of these terms can be found in appendix B, this section will only show the resulting expressions for σ_0 and τ_0 in equations 2.4 and 2.5 respectively.

$$\sigma_0 = A_1 cosh(\beta_1 x) + A_3 cosh(\beta_H x) cos(\beta_V x) + A_5 sinh(\beta_H x) sin(\beta_V x) \tag{2.4}$$

$$\tau_0 = C_1 sinh(\beta_1 x) + C_2 sinh(\beta_H x) cos(\beta_V x) + C_3 cosh(\beta_H x) sin(\beta_V x) \tag{2.5}$$

The equations show that the normal and shear stress depend on the location x on the beam, where x can vary between 0 and l. This is because the equations are symmetrical around the plane x=0, shown as the center line in figure 2.4(a). The expressions for β_1, β_H, β_V, A_1, A_3, A_5, C_1, C_2 and C_3 can be found in appendix B.

2.2.2. MODEL RESULTS

VARYING THE SOLDER LAYER THICKNESS

Chen's model predicts the shear and normal stress in the joint. This model requires several input parameters: the material properties, length of the strips, thickness of the strips and thickness of the solder layer. For this analysis the length and thicknesses of the strips are equal to those used in the test described in section 2.1.3. The only unknown is the solder layer thickness, which as described before, needs to be estimated. Figures 2.5 and 2.6 shows the effect of varying the solder layer thickness, for the case of 1mm Copper soldered to 5mm Aluminum.

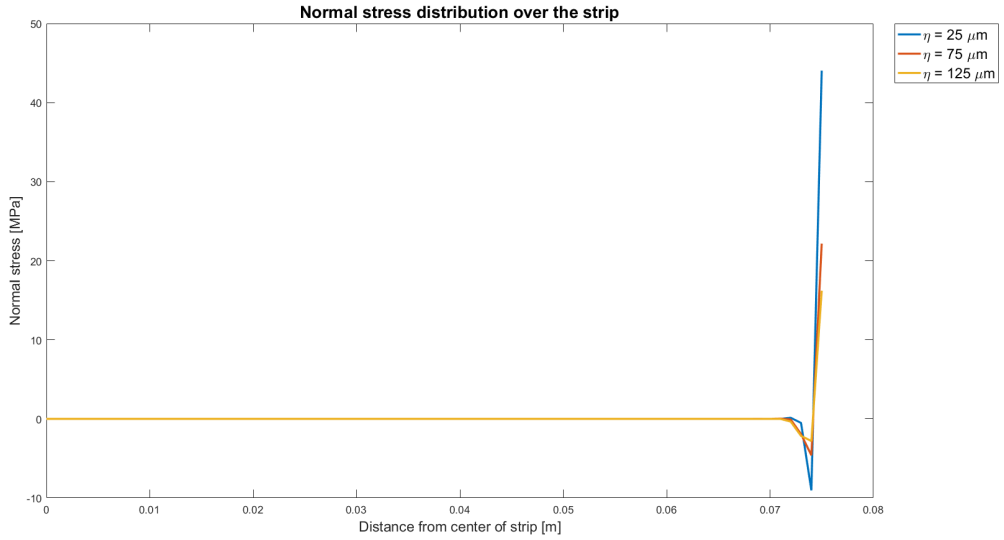

Figure 2.5: The influence of varying the solder layer thickness η on the normal stress. These results are for the case were 1mm Copper is soldered to 5mm Aluminum. Three layer thicknesses are taken, an η of 25, 75 and 125 μm.

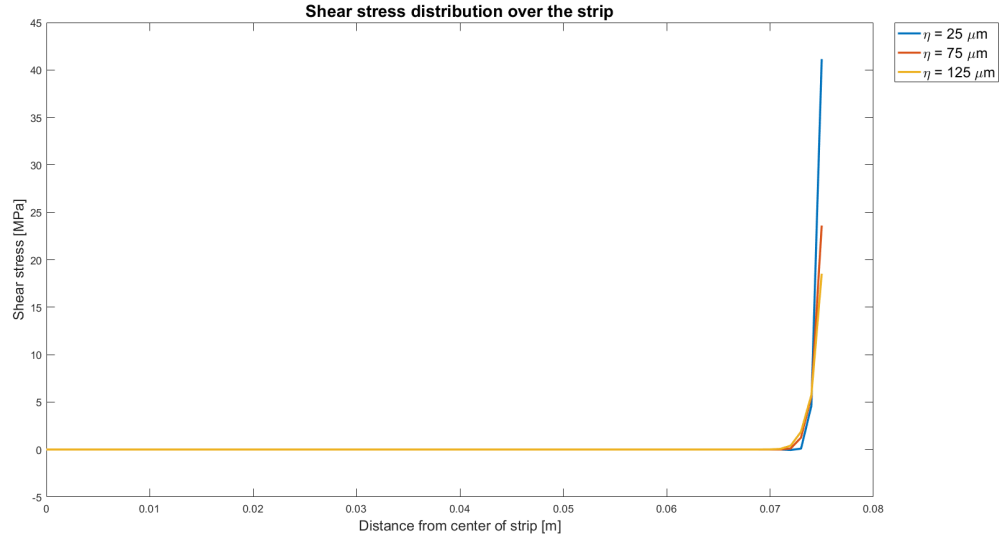

Figure 2.6: The influence of varying the solder layer thickness η on the shear stress. These results are for the case were 1mm Copper is soldered to 5mm Aluminum. Three layer thicknesses are taken, an η of 25, 75 and 125 μm.

Both figure 2.5 and 2.6 clearly show that both stresses in the larger part of the solder layer are equal to zero, and rise steeply in the 5 cm of the strip. This is because the stresses are derivatives of the horizontal and vertical force, as shown be equation 2.6 and 2.7. If a derivative is equal to zero, the function is either a constant or zero. Which means that for this case, the horizontal and vertical force in the solder layer remain constant in the first part of the strip. Because the end of the strip is not fixed, the vertical and horizontal force will be zero there. This results that in the last 5 cm of the strip the forces will rapidly go to zero, causing the large spikes in the stress figures.

$$\frac{dT}{dx} = \tau_0 \tag{2.6}$$

$$\frac{dV}{dx} = \sigma_0 \tag{2.7}$$

The normal stress experiences first a dip, which indicates that the solder layer will be compressed, before it starts to increase drastically. This can be explained by peel stress, which means that the strips slightly bend upwards near the end. Increasing the thickness of the solder layer results in a lower maximum normal stress. For the shear stress, one can see that over the last 5 mm the shear stress increases drastically. Similar to the normal stress, when the solder layer thickness increases the maximum shear stress will decrease.

FEM MODEL

To verify the analytical model results, the software package Creo was used to built a Finite Element Method (FEM) model. This was done by a mechanical engineer at SRON. The analytical model is verified for the 1 mm copper, 5 mm aluminum and a solder layer thickness of 75 μm and a strip length of 15 cm. Due to symmetry, only the right half is shown. The FEM model is a 3D model, the width is specified as 1 cm. The results are shown in figures 2.7 and 2.9. The stresses in the FEM model are determined for three locations; the top of the solder layer, the middle of the solder and the bottom of the solder layer.

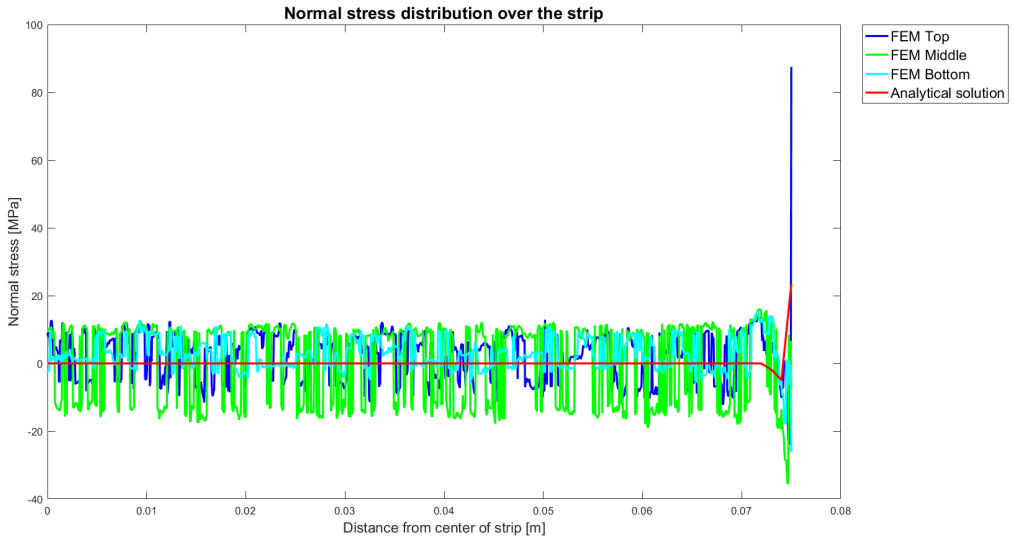

Figure 2.7: Analytical and FEM results for the normal stress of the solder layer for an aluminum thickness of 5 mm, copper thickness of 1 mm and solder layer thickness of 75 μm.

All three FEM models for the normal stress fluctuate around zero for the larger part of the strip. Towards the end, the peel stress shows differently in the top and bottom of the solder layer. This is due to the definition of positive (tensile) stress, which is shown in figure 2.8. The upward bending due to the peel stress, will cause a negative normal stress at the bottom layer.

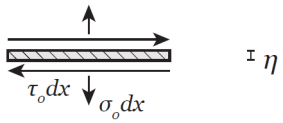

Figure 2.8: Normal and shear stress directions on the solder layer.

Figure 2.8 shows the shear stress over the strip. The shear stress is positive for all thee locations in the solder layer, which is again due to the definition of positive shear stress. The higher peaks, which could also be seen in the normal stress, are due to the nature of the FEM model. The FEM model generates an automatic grid, with more nodes at areas the software thinks are relevant. This results in a lot of nodes around the solder layer, while this layer only has a thickness of 75 μm. This effect can cause peaks in the FEM software, which might not be accurate.

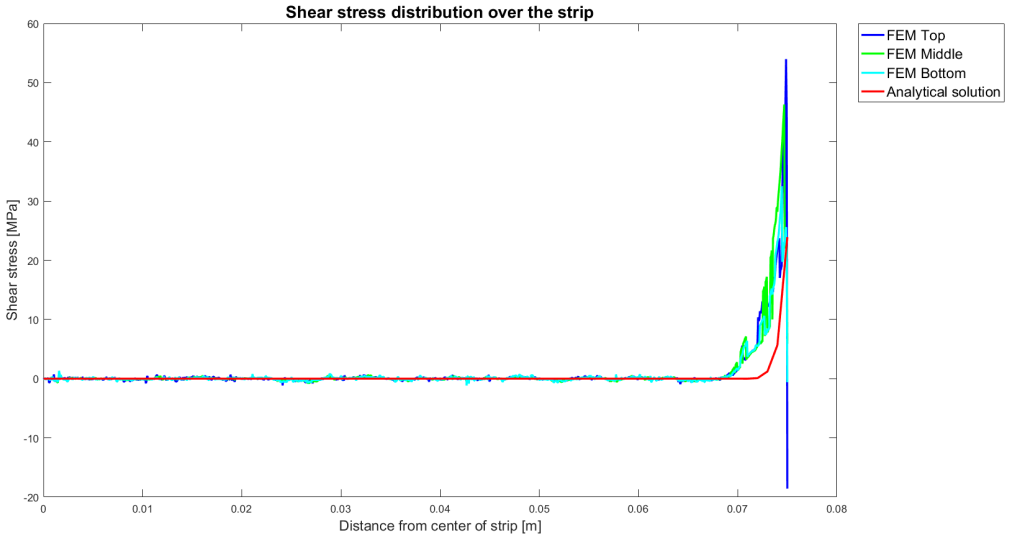

Figure 2.9: Analytical and FEM results for the shear stress of the solder layer for an aluminum thickness of 5 mm, copper thickness of 1 mm and solder layer thickness of 75 μm.

VARYING THE MATERIAL THICKNESSES

In this section the impact of varying material thickness on the normal and shear stress is determined. First, the analytical results for the normal stress are analyzed. Figure 2.10 shows a constant copper thickness of 1 mm while figure 2.11 shows a constant copeer thickness of 2 mm. Both figures have a η of 75 μm, and the aluminum thicknesses will be varied.

Both figures show the expected graph for the normal stress; zero normal stress over the main part of the strip, a small dip which is followed by a high tensile stress. The figures show that increasing the aluminum thickness increases the normal stress. Looking back at section 2.1.4, increasing the aluminum thickness decreased the deflection of the strip. This indicates a connection between the deflection and the solder layer normal stress; the energy 'used' to deflect the strip will not be contained in the solder layer. Thus a smaller deflection yields a higher normal stress and vise verse.

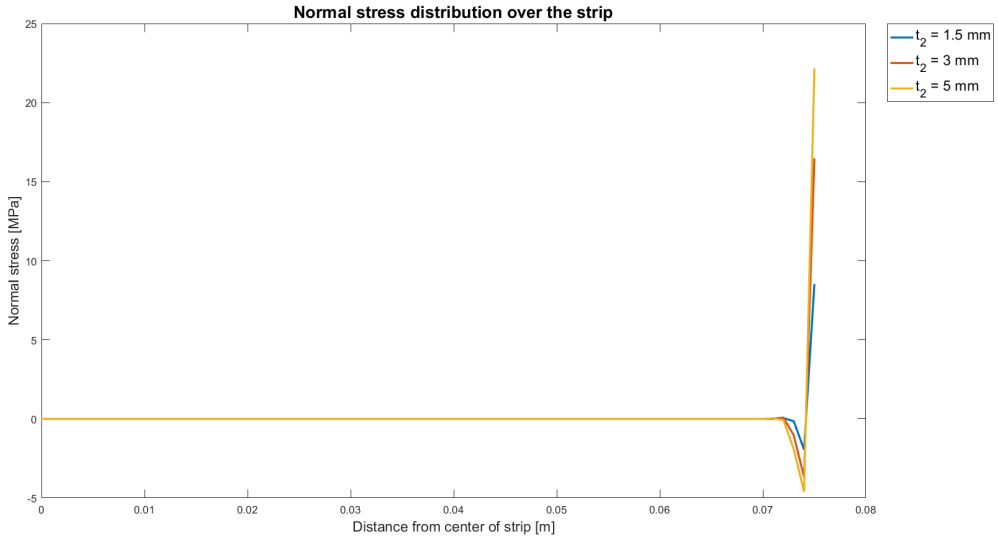

Figure 2.10: The normal stress of the analytical model for a copper thickness of 1 mm, solder layer thickness of 75 μm and varying aluminum thicknesses.

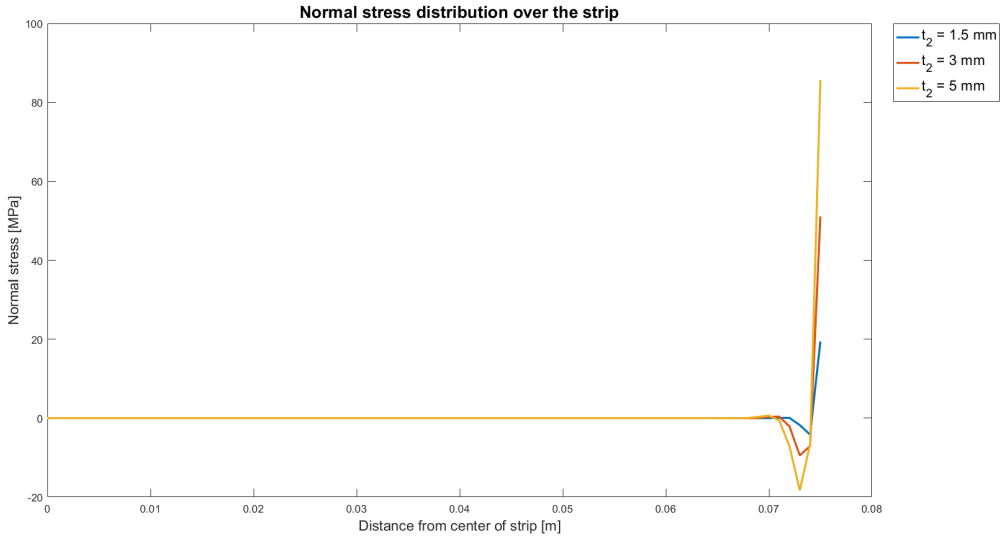

Figure 2.11: The normal stress of the analytical model for a copper thickness of 2 mm, solder layer thickness of 75 μm and varying aluminum thicknesses.

The analytical results for the shear stress are presented in figures 2.12 and 2.13. The first figure has a constant copper thickness of 1 mm, the second figure of 2 mm. The solder layer η is 75 $/mum$ and the aluminum thicknesses will be varied.

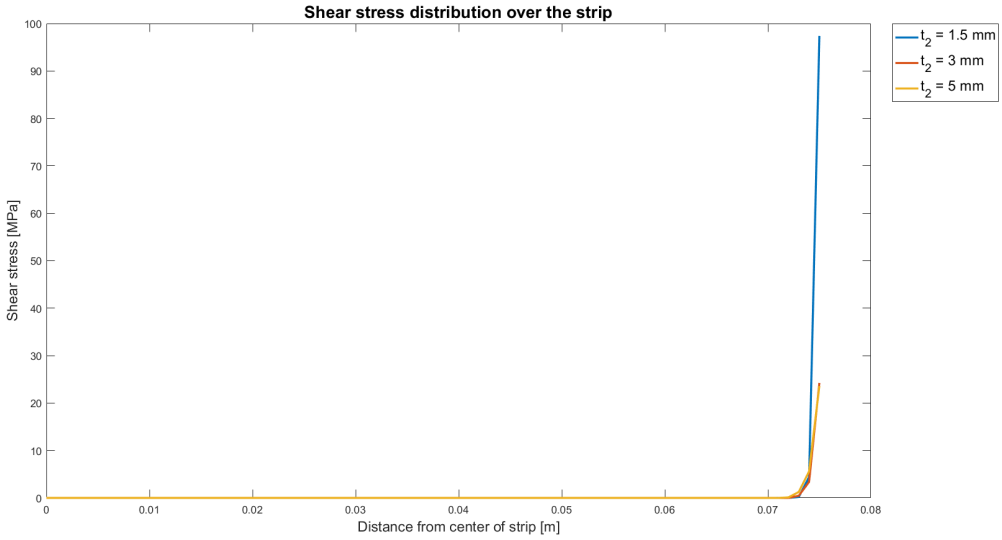

Figure 2.12: The shear stress of the analytical model for a copper thickness of 1 mm, solder layer thickness of 75 μm and varying aluminum thicknesses.

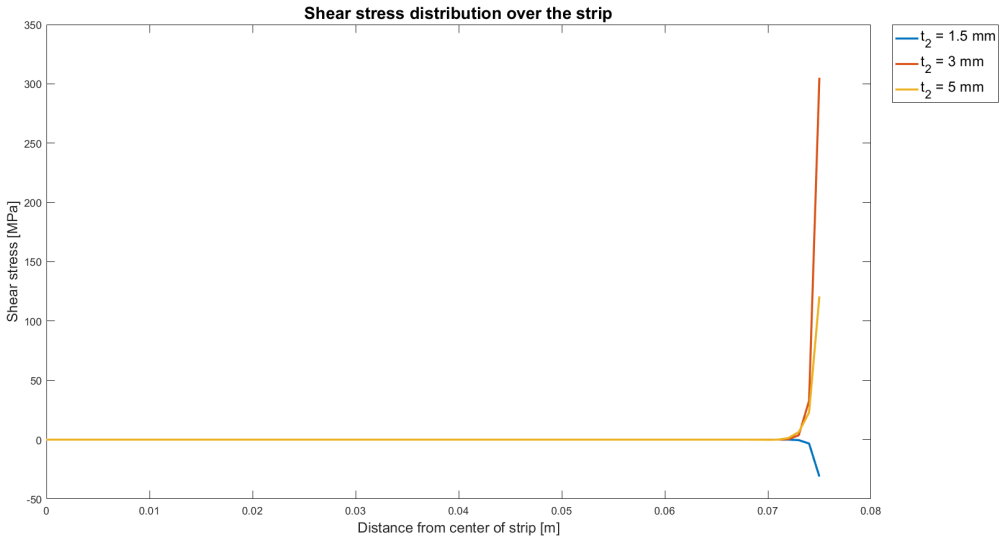

Figure 2.13: The shear stress of the analytical model for a copper thickness of 2 mm, solder layer thickness of 75 μm and varying aluminum thicknesses.

Figure 2.12 shows the expected form of the graphs, however the maximum shear stress for an aluminum thickness of 1.5 mm seems high. When looking at figure 2.13, the results are not as expected. A negative shear stress is found for an aluminum thickness of 1.5 mm, and an extremely positive value is found for an aluminum thickness of 3 mm. To verify these results, FEM models are created for the deviating results. These FEM model results are shown in figures 2.14 and 2.15.

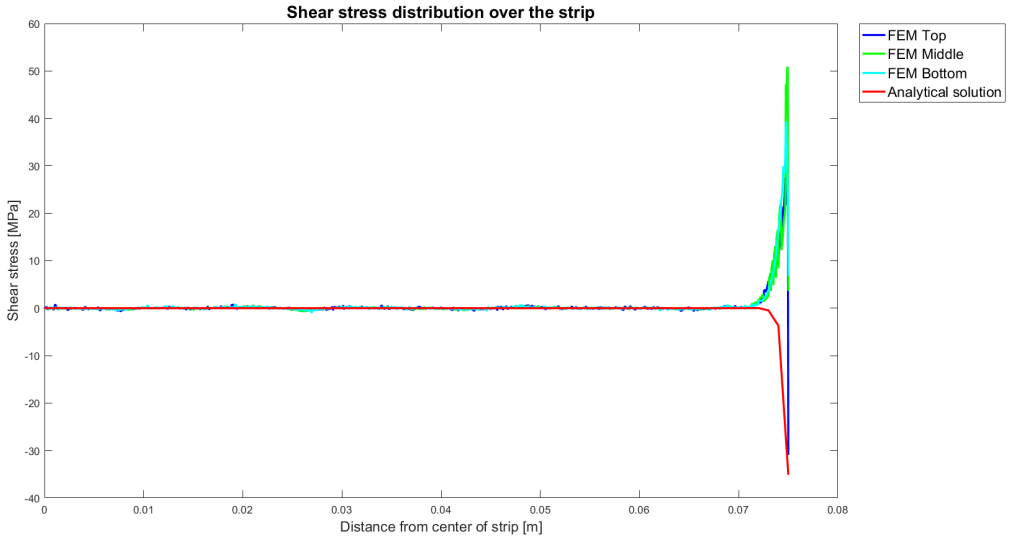

Figure 2.14: Analytical and FEM results for the shear stress of the solder layer for an aluminum thickness of 1.5 mm, copper thickness of 2 mm and solder layer thickness of 75 μm.

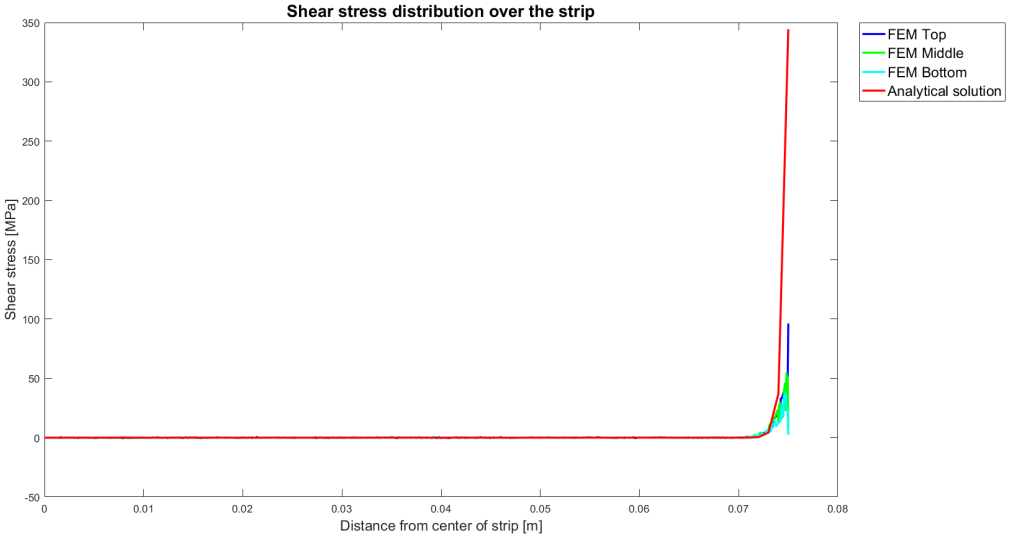

Figure 2.15: Analytical and FEM results for the shear stress of the solder layer for an aluminum thickness of 3 mm, copper thickness of 2 mm and solder layer thickness of 75 μm.

Both FEM models predict different shear stress results than the analytical model. The FEM models show more consistent results. Investigating the analytical model showed that for aluminum thicknesses smaller than the copper thickness the shear stress will become negative. If the thickness of aluminum is 1.4 times that of copper, an enormous stress peak is calculated. However, at larger thickness ratios the results match the FEM models again, as can be seen in figure 2.9. For the remainder of this thesis, the thickness ratios will be much larger thus using the analytical model will not influence the results of this thesis. It should however be noted, that the analytical model for shear stress is not accurate at low thickness ratios and should therefore be investigated more.

3

THERMAL HEAT TRANSFER

The 2-4 GHz board will have several high power dissipating components, which require passive thermal cooling. This will be achieved by a mechanical bracket which will be soldered to the PCB. In this chapter a thermal heat transfer model of such a PCB assembly will be shown, which can predict the temperatures of the bracket and power dissipating components. The thermal heat transfer model is developed using an existing frame, that of the Local Oscillator (LO) board. The aluminum bracket design of the LO board is already much lighter than the massive copper design of the existing 2-4 GHz board, which gives a good starting point for determining the performance of light weight brackets. Figure 3.1 shows a picture the LO board used for testing, the dimensions of the bracket are specified in the technical drawings in appendix C.1.

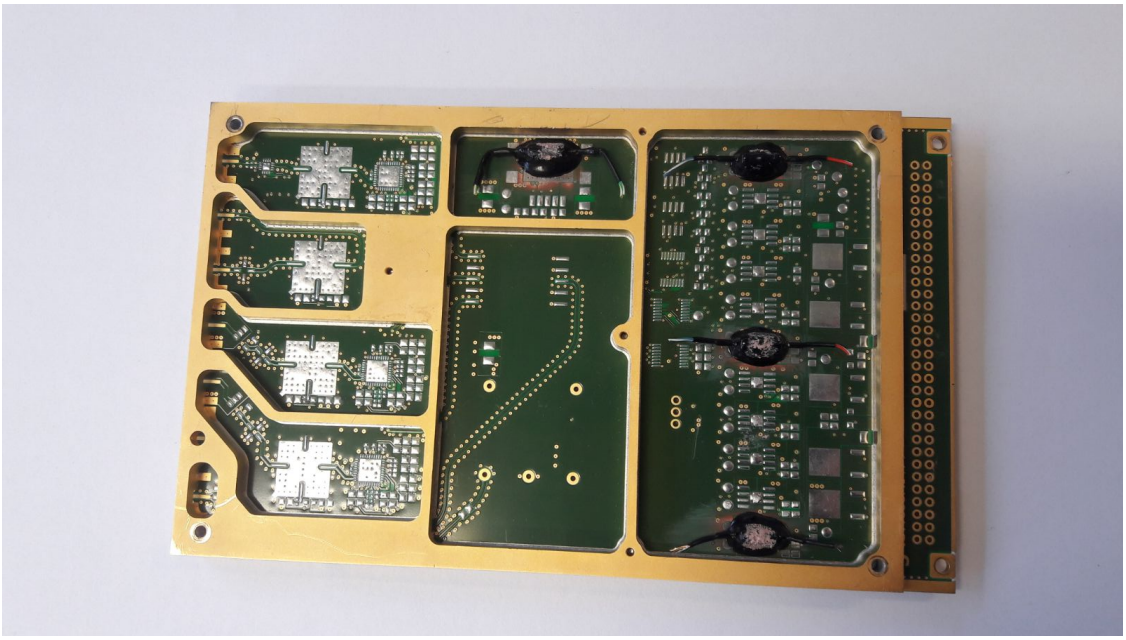

Figure 3.1: Picture of the LO board.

3.1. HEAT TRANSFER MECHANISMS

Thermal cooling of the LO board can be achieved via conduction, convection and radiation. In section 3.1.1 - 3.1.3 these concepts will be described.

3.1.1. CONDUCTION

Conduction is a form of heat transfer through a solid, liquid or gas that is in close contact. The process involves the transfer of kinetic thermal energy between electrons. Heat conduction can mathematically

expressed by the Fourier's equation for one dimensional, steady state heat flow in case of conduction [7, p.28]:

$$q = kA\frac{\Delta T}{L} \tag{3.1}$$

With the rate of heat transfer q (W), the thermal conductivity k (W/mK), the cross sectional transfer area A (m^2) , the length L (m) and the temperature difference ΔT (K). Thermal conductivity k is the material's ability to conduct heat, this is a property of homogeneous materials. For non-homogeneous materials, relative thermal conductivity should be used because orientation and thickness of layers will influence the thermal conductivity [7, p.29].

Another material thermal property is the thermal resistance R (K/W), which is the ability of a material to resist the flow of heat [8, p.10]. The mathematical expression can be derived from equation 3.1 [7, p.29]:

$$R = \frac{\Delta T}{q} = \frac{L}{kA} \tag{3.2}$$

3.1.2. CONVECTION

Convection is the transfer of heat from one place to another by the movement of fluids. This heat transfer mechanism will be important for the on ground analysis, where the air acts as fluid. However, in vacuum the air can not act as fluid and this heat transfer mechanism will disappear. The mathematical expression of convection is:

$$q = h_{conv}A(T_{loc} - T_{amb}) \tag{3.3}$$

With the heat transfer rate q (W), the convection heat transfer coefficient h_{conv} (W/m^2L), the surface area A (m^2), the local temperature T_{loc} (K) and the ambient temperature T_{amb} (K). The convection heat transfer coefficients applicable for PCB's can be found in table C.1.

Table 3.1: Convection heat transfer coefficients [9]

Geometry	$[W/m^2K]$
Horizontal Plate	
a) Hot surface facing up	$h_{conv} = 1.32\left(\frac{\Delta T}{L_c}\right)^{0.25}$ (3.4)
b) Hot surface facing down	$h_{conv} = 0.59\left(\frac{\Delta T}{L_c}\right)^{0.25}$ (3.5)
Components on a circuit board	$h_{conv} = 2.44\left(\frac{\Delta T}{L_c}\right)^{0.25}$ (3.6)

With the temperature difference ΔT (K), which is equal to $T_{loc} - T_{amb}$ from equation 3.3. The parameter L_c (m) depends on the surface area A (m^2) and perimeter p (m), and can be expressed as:

$$L_c = \frac{4A}{p} \tag{3.7}$$

3.1.3. RADIATION

Thermal radiation is the energy transfer by the emission of electromagnetic waves which carry energy away from the object. The Stefan-Boltzmann Law, given in equation 3.8, gives the net radiation between the object and its surroundings.

$$q = A\epsilon\sigma(T_{loc}^4 - T_{amb}^4) \tag{3.8}$$

In this equation q (W) is the heat transfer, A (m^2) the radiation surface, ϵ $(-)$ the emissivity of the surface, σ $(W/m^2/K^4)$ the Stefan-Boltzmann constant, T_{loc} (K) the local temperature of the object and T_{amb} (K) the ambient temperature.

3.2. MODEL DESCRIPTION

The conduction, convection and radiation theories will be applied in a thermal model of the LO board and bracket. In this analysis we only use the most dissipating components on the LO board, because they impact the thermal behaviour the most. The locations of the most dissipating components are shown in figure 3.2 and table 3.2. The heat dissipated by these components, will be transferred away via the heat transfer mechanisms described above. The bracket is a passive way to conduct the heat away from the LO board. This heat is conducted into a heat sink, which is a large mass able to store the energy.

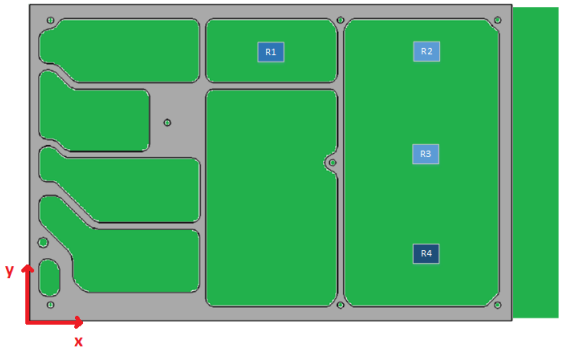

Figure 3.2: Location of the most dissipating components on the LO board.

Table 3.2: Location of the heaters on the LO board.

Heater	Dissipation [W]	x location [mm]	y location [mm]
R1	2.63	73.5	89.5
R2	1.95	120.0	89.5
R3	1.95	120.0	52.0
R4	3.22	120.0	9.5

To model the heat transfer mechanisms of the LO board, the board is divided into nodes. The location of these nodes is chosen to match with the heat sources, heat sink and the intersection of walls. The nodes are shown in figure 3.3, the x and y locations of the nodes in table 3.3. It should be noted that the axis system start at the bottom left of the bracket, while the bracket nodes are outlined from the top left. This results that the nodes of the first row have the highest y-distance. For example; heater R1 is located on (73.5,89.5) which corresponds with node (2,6).

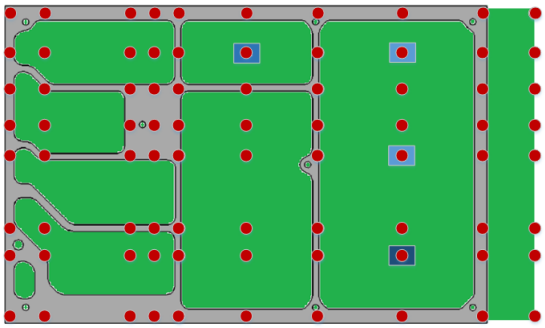

Figure 3.3: Nodes on the LO board.

Table 3.3: Locations of the nodes.

column/row number	1	2	3	4	5	6	7	8	9	10
x distance [mm]	1.5	11.5	37.5	45.75	54	73.5	97	120	148.5	158.5
y-distance [mm]	96.25	89.5	73.5	62.25	7 52.0	27.75	9.50	2.25		

The thermal model is a 2D model, temperature variations in the z-direction are assumed to be very small and are thus ignored. The ambient temperature is assumed to be constant. For each node, the conduction, convection and radiation components are identified. Nodes placed on the bracket (see figure 3.3) contain two parallel conduction terms, one for the conduction via the PCB and one for the conduction via the bracket. The heat sink is attached to the left side of the bracket. All these heat transfer components create a complex network, which will be solved using the software package LTSpice. LTSpice is built for electronic design, but the same principles hold for the thermal relations. The voltage can be replaced by temperature and the current by heat flow, to transform the electrical model into a thermal model. A detailed description of the LTSpice model is presented in appendix C.

3.3. MODEL RESULTS

The dissipation of the heaters is taken according to table 3.2, which means that 2.63 W will be dissipated by R1, 1.95 W by R2 & R3 and 3.22 W by R4. Two cases are simulated by the model, one with a pressure of 1013 $mbar$ and one with 20 $mbar$ (which is the pressure limit of the chamber). The temperature distributions for both cases are given in figures 3.4 and 3.9.

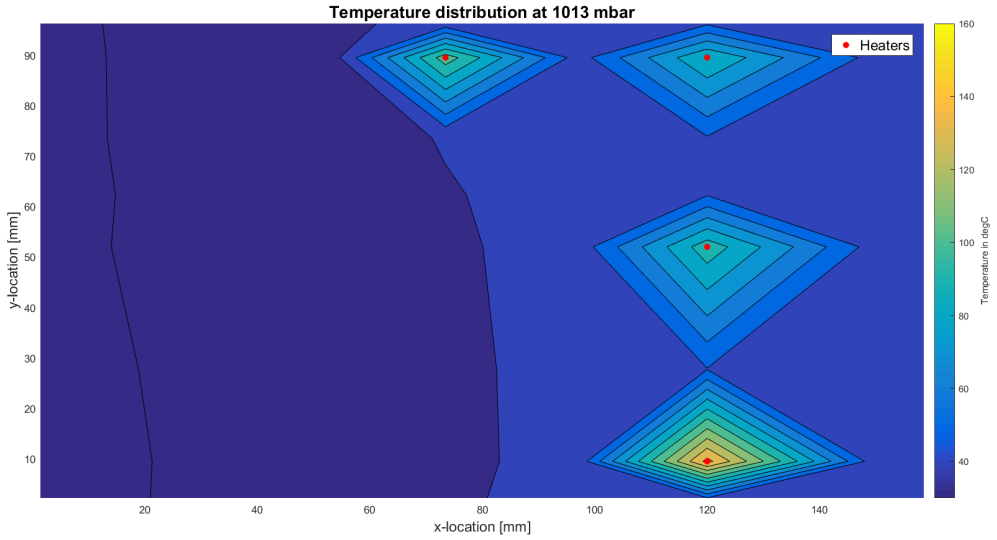

Figure 3.4: The temperature distribution at 1013$mbar$.

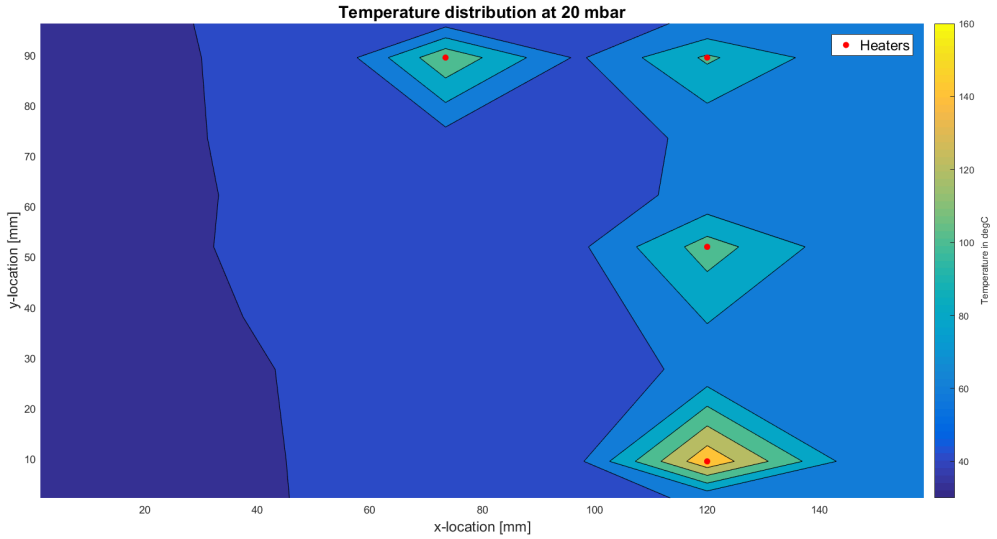

Figure 3.5: The temperature distribution at 20$mbar$.

Figures 3.4 and 3.9 clearly show the 4 locations of the heaters, because the heaters create temperature hot spots. For both situations, one can see that R4, the heater with the highest dissipation, reaches the highest temperature (141.9 $^{\circ}C$ at 1013 $mbar$ and 154.8 $^{\circ}C$ at 20 $mbar$). Although the dissipation of R2 and R3 is equal, they reach different temperatures. R2 reaches temperatures of 79.4 $^{\circ}C$ and 92.5 $^{\circ}C$, while R3 reaches temperatures of 94.9 $^{\circ}C$ and 108.5 $^{\circ}C$. This is because that heater is placed closer to the bracket, and can thus lose its heat more easily. The heat sink is attached to the left side, explaining the temperature gradient to that side. At the other side the heat can not conduct away, therefore this side will reach a constant temperature of 45.8 $^{\circ}C$ at 1013 $mbar$ and 60.5 $^{\circ}C$ at 20 $mbar$. When comparing the two situations, the effect of the loss of convection can be seen; higher temperatures at the heaters and a larger temperature gradient over the board. This larger gradient indicates that more energy is transferred via conduction.

3.4. TEST SETUP

Through reflow soldering, the bracket is soldered to the PCB. Details on the solder process are given in section 2.1.3. The test will not use actual dissipating amplifiers and regulators since this would imply a fully operational board which is not necessary at this stage of the research. Heaters will be used to simulate the major dissipating components of the board. A heater is a resistor, with values of 4.9 Ω for R1, 3.7 Ω for R2 and R3 and 5.8 Ω for R4. These heaters are glued using the Stycast 2850FT with catalyst 24 LV adhesive to the PCB.

The LO board is attached by 2 M2.5 screws to a support plate, which will act as the heat sink in this test setup. To avoid that conduction through the air will be the main heat path between the LO board and the heat sink, the LO board is attached in such a way that the LO board will extend to the side of the heat sink. A picture of the test setup is shown in figure 3.6.

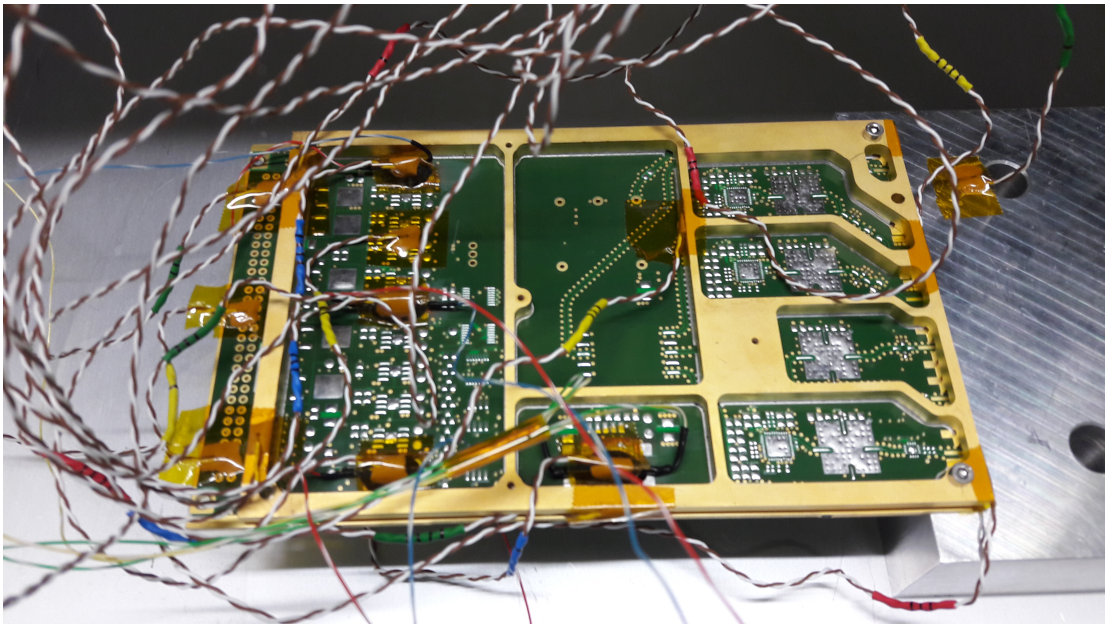

Figure 3.6: Thermal test setup.

The temperature measurements are performed by 16 T-type thermocouple sensors. To improve the connection between the thermocouple and the measurement spot, a PC94 non-silicone thermal conductive pad is used. This is attached to the bracket and PCB using Kapton tape. It is ensured that the cables of the thermocouples do not contact the Lo board on other points, to avoid disturbances in the measurements. The placement of the thermocouples is shown in figure 3.7. The temperature registration is done by a Netdaq. A Netdaq is a multi-input data acquisition device from Fluke which is able to sequentially measure multiple sensors and store the data on a PC.

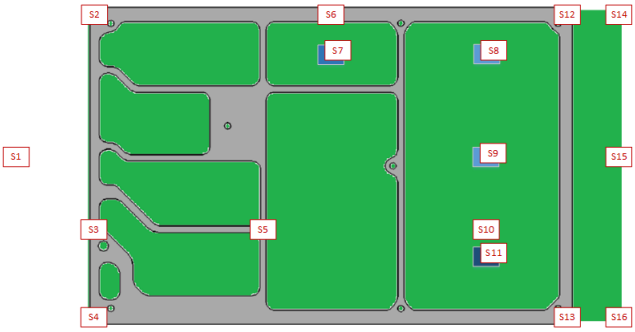

Figure 3.7: Thermocouple placement on the LO board.

The power for the heaters is supplied outside of the chamber, and is set for a constant current. The power source is positioned outside of the chamber, because it is not suited for vacuum conditions and the internal dissipation would disturb the measurements. The heaters are placed in series when the power is connected. Because the vacuum chamber has by design no feedthrough for cables, an improvised feedthrough is made by using a surgeon glove. The sensor and power cabling will be lead through a surgeon glove over the rubber sealing of the vacuum chamber. This surgeon glove is softer than the rubber seal of the vacuum chamber, and will fill up the gaps created by the cabling. A picture of this improvised feedthrough is shown in figure 3.8.

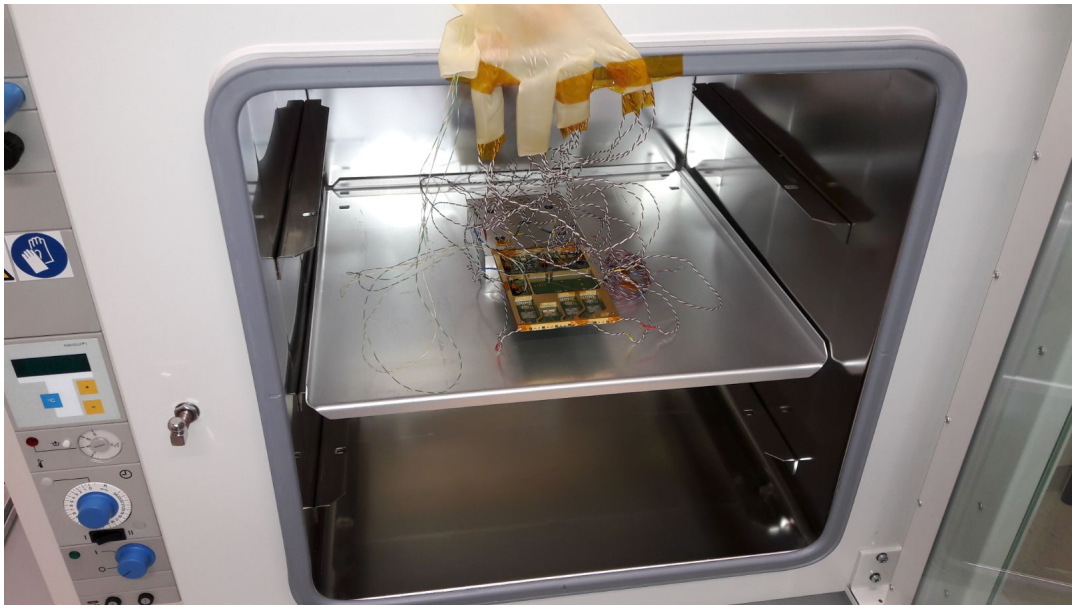

Figure 3.8: The surgeon glove used as improvised feedthrough.

3.5. TEST RESULTS

The test setup described above is tested at two conditions. First the temperatures of the thermocouples are measured at 1013 $mbar$, while in the second part of the test the temperatures are determined at 20 $mbar$. The resulting graphs for four thermocouples (S1,S4,S11,S13) are shown in figure 3.9. The heatsink temperature is given by S1, the bottom corner attached to the heat sink by S4, the opposite corner without any attachments by S13 and the hottest component by S11. These thermocouples represent the temperature distribution over the board. The graphs and exact measurement data for the other thermocouples can be found

in appendix C.3.

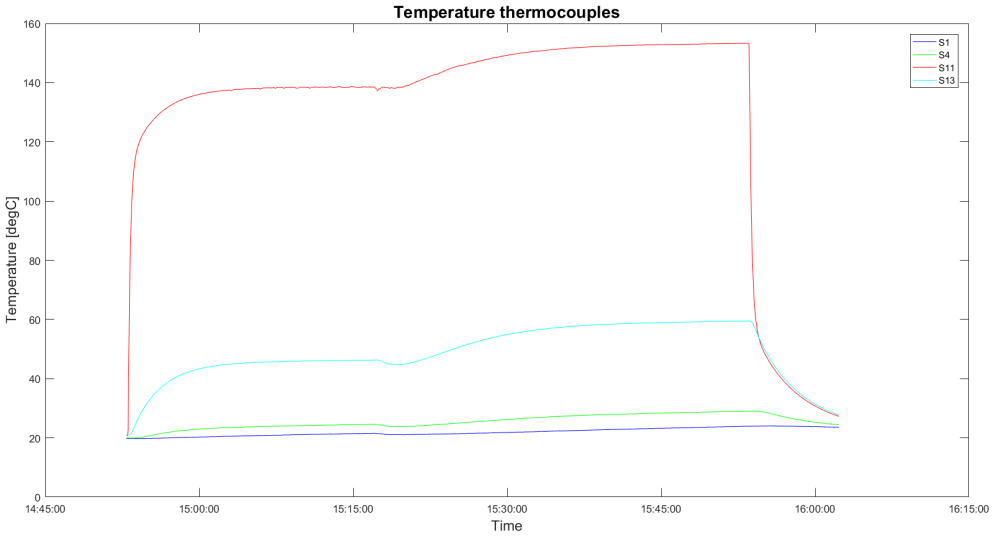

Figure 3.9: The temperature distribution at 1013 and 20 $mbar$.

The figure shows the temperatures measured by each thermocouple. At 14:52, the power is turned on at 1013$mbar$ causing the heaters to dissipate energy. The temperatures measured by the thermocouples start to rise and are stabilized after 25 minutes. The, by the heaters, generated heat flows will find thermal resistances on their way. How larger this resistance, how higher the temperature will be. The exact values, in combination with the model values are given in table 3.4. The exact measurement data for all other thermocouples can be found in appendix C.3.

Table 3.4: Temperatures of the thermocouples at 1013 $mbar$.

Location	Model Temperature [$°C$]	Measured Temperature [$°C$]	Error [$°C$]
S1	22.2	21.5	0.7
S4	24.6	24.5	0.1
S11	141.9	138.5	3.4
S13	47.1	46.3	0.8

At 15:19, the vacuum pump is turned on. The removal of pressure will cause due to thermodynamic relations a small dip in the temperature. According to O'Hanlon [10], the actual thermodynamic relation is difficult to describe: *"In a real system, the behaviour is neither isentropic nor isothermal, but lies somewhere in between these two regimes; the temperature will drop, then relax to its ambient temperature"*.

During the drawing of the vacuum, and when the 20 $mbar$ pressure is reached, the temperatures of the thermocouples will increase before stabilizing again. This is because of the loss of the convection component of the heat transfer mechanisms. The LO board has reached a stable temperature after roughly 30 minutes at 15:52, the exact values and model temperatures are given in table 3.5. The temperature values for the other thermocouples are given in appendix C.3.

Table 3.5: Temperatures of the thermocouples at 20 $mbar$.

Location	Model Temperature [$^\circ C$]	Measured Temperature [$^\circ C$]	Error [$^\circ C$]
S1	23.5	23.8	-0.3
S4	27.3	28.9	-1.6
S11	154.8	153.2	1.6
S13	60.7	59.4	1.3

The test results don't match the measurement results exactly. The main reason is that the model is an approximation of the actual bracket. Estimations on convection and radiation area's, the exact positioning of walls and the 2D simplification will all influence the model temperature.

This results, for all the thermocouples on the PCB and frame, in errors of around 3 $^\circ C$. For the heaters the error are larger, but also of less importance. In the test setup the heaters are glued to the PCB, and an estimation on the thermal resistance of the glue needs to be made. For electronic components however, the thermal resistance between the junction and lead are defined. This means that the actual resistance between the PCB and the hottest part of the electrical component is exactly known. The error made by the estimation on glue resistance, will thus not be present in the thermal model for the 2-4 GHz board design.

4

MATERIAL TRADE-OFF

4.1. MATERIAL REQUIREMENTS

4.1.1. DENSITY

The original 2-4 GHz bracket was made of gold-plated copper. The research goal is to design a lighter bracket, so for this thesis the focus will be on materials with a density lower than, or similar to, the density of copper. A rationale for this limitation needs to be applied here; because the mass of the bracket is determined by the density and the volume of the material. There might exist materials with a larger density but with much better material properties, requiring less volume. With such materials the bracket could become extremely thin-walled. This thesis however, focuses more on the thermal aspects of the bracket design. Therefore the impact of extremely thin-walled solutions can not be predicted accurately, and these solutions are excluded from this thesis. In further research these solutions should be included.

4.1.2. SOLDERABILITY

For the design of the 2-4 GHz board an new design solution is implemented; the bracket will be soldered to the PCB. Previous flight assemblies produced by SRON consisted of screwed connections between the PCB and the bracket. This new design philosophy results in an obvious, but important material requirement; the bracket material must be suitable for soldering after surface treatments.

4.1.3. EMI

Several high frequency components will be placed on the 2-4 GHz board. These components will emit electromagnetic waves at high frequencies. To avoid interference due to these electromagnetic waves, shielding is required. "Shielding involves placing a conductive surface around the critical parts of the circuit so that the electromagnetic field which couples to it is attenuated by a combination of reflection and absorption" [11]. Thus, Electromagnetic Interference (EMI) shielding requires the use of a conductive material.

Electromagnetic Compatibility (EMC) can be divided into four categories; conducted emissions, conducted susceptibility, radiated emissions and radiated susceptibility. The conducted EMC forms propagate via power lines, which will be accounted for by the electrical engineers in the PCB design. The radiated forms propagate via free space. Radiated susceptibility covers the effect of the environment on the performance of the board. Although this form of EMC is ideally minimized by shielding the board, shielding is not required. If the board can deliver the required performance without shielding, there is from the ESA perspective no need for shielding. However, for the radiated emissions (the influence of the board on the environment) this is different. ESA allows only limited radiations. This is achieved by case shielding, for which requirements are established. For example the requirements for the SCIAMACHY project are [12]:

Each equipment shall be enclosed in an electrically conductive and non-magnetic housing in order to prevent radiated emissions from penetrating from/to the electronic circuits. The housings shall be dimensioned and designed such that they attenuate radiated power about the following value:

- 150 kHz to 500 kHz: 40 dB
- 500 kHz to 40 GHz: 60 dB

At this point, restrictions for this thesis work need to be implemented. For this thesis the baseline is that the 2-4 GHz board will act as a "black box", for which the radiated emissions need to be attenuated. However, when looking at the larger system, the 2-4 GHz board will be part of an entire instrument. This instrument will be placed in an electronic box. In a final instrument design one could regard this electronic box as "black box" which needs to be shielded. From ESA's perspective, this would require shielding of the electronic box and not of the individual PCB assemblies. Thus, for a final instrument design different shielding solutions might be implemented. Such solutions however, provide challenges related to the internal EMI. More details on this will be given in section 5.1.3.

4.1.4. CONSTRAINING ECSS

As preparation on this thesis, a literature study on advanced electronic packaging materials was performed. Part of this study focused on the applicable ECSS for material selection. The study showed that most of the ECSS clauses do not restrict the material choice beforehand, but rather provide a compliance list afterwards (for example; ECSS-Q-ST-70-71C clause 5.1.2a states: "Material properties shall be compatible with the thermal environment to which they are exposed" [13]). The few clauses that restrict the material choice are shown in table 4.1.

Table 4.1: Constraining ECCS Clauses [13, 14].

ECSS Clause	Description
ECSS-Q-ST-70C-5.1.5a	Spacecraft and associated equipment shall be manufactured from materials and by processes that do not cause a hazard to personnel or hardware, whether on the ground or in space.
ECSS-Q-ST-70C-5.1.12b	Galvanic compatibilities shall be selected in conformance with Table 5-1 of ECSS-Q-ST-70C.
ECSS-Q-ST-70C-5.2.2a	Pure tin finish with more than 97 % purity shall not be used.
ECSS-Q-ST-70-71C-4.2.2b	Wrought alloys 5456, 5083 and 5086 shall be used only in controlled tempers for resistance to SCC and exfoliation.
ECSS-Q-ST-70-71C-4.2.2d	Black anodising shall not be used on 2000 and 7000 series of Aluminum.
ECSS-Q-ST-70-71C-4.2.16b	Composite materials made with polyester containing styrene shall not be used.
ECSS-Q-ST-70-71C-4.2.18o	Polyvinyl acetate shall not be used in space applications.
ECSS-Q-ST-70-71C-4.2.18p	Polyvinyl butyrate shall not be used in space applications.

4.1.5. OVERVIEW MATERIAL REQUIREMENTS

An overview of the material requirements, presented in sections 4.1.1 - 4.1.4, can be seen in the bullet list below:

- The selected material shall have a density lower than, or equal to, the density of copper
- The selected material shall be solderable after surface treatments
- The selected material shall be a conductive material
- The selected material shall comply with the ECSS clauses presented in table 4.1

4.2. MATERIALS

4.2.1. METAL ALLOYS

Traditionally, heat from electronic devices is dissipated to heat sinks by using high thermal conductivity housing materials (such as copper) [15, 16]. Electronic packaging materials conventionally used in the electronic industry are aluminum, Kovar and molybdenum [7, p.233]. For specific space applications Del Castillo [16] states that:*"Current housings for RF modules in space-based applications are most often made from either Kovar or 6061 Al"*. An overview of materials properties of several metal alloys frequently used in thermal packaging is shown in table 4.2.

Table 4.2: Metal alloys frequently used for electronic packaging.

	ρ $[g/cm^3]$	CTE $[ppm/K]$	E-modulus $[GPa]$	k $[W/mK]$
Copper (C11000) [5]	8.92	16.8	118	394
Aluminum (Al6061) [6]	2.7	23.6	68.9	167
Titanium [17]	3.76	5.5	107	17
Magnesium (AZ91D) [18]	1.81	25	45	72
Molybdenum [19]	10.22	5.2	320	126
Kovar [20]	8.36	4.9	138	17.3

4.2.2. METAL MATRIX COMPOSITES

In the literature study performed as preparation on this thesis, advanced electronic packaging materials were studied. This study showed that Metal Matrix Composites (MMCs) have promising capabilities. The need for MMCs lies in the achieved property combinations beyond those attainable in monolithic metals alone. Thus tailored composites resulting from the addition of reinforcements to a metal may provide enhanced specific material performance [21, Section 1 p.33]. This is specially advantageous for electronic packaging, because they can offer a combination of high thermal conductivity, relatively low density and a tailorable CTE to match the CTE of the substrate [7, p.234].

Typically, MMCs posses a metal matrix with one or more different reinforcements. The choice of a matrix alloy for an MMC is dictated by several considerations, but for high thermal conductivity applications the principal matrix choices are aluminum, copper and their alloys. Barcena 2008 [15] evaluates copper-diamond as possible packaging solution for space applications. Another study performed by Rawal 2001 [22], lists three composites of discontinuous reinforced aluminum with possible space applications. An overview of these materials and their material properties is presented in table 4.3.

Table 4.3: Possible MMCs for space applications.

	ρ $[g/cm^3]$	CTE $[ppm/K]$	E-modulus $[GPa]$	k $[W/mK]$
Copper Diamond [15]	6.3	6	222	430
Aluminum Silicon [22]	2.54	13.6	102	135
Aluminum Silicon Carbide [22]	2.8	15.5	115	150
Aluminum Graphite [22]	2.5	7.5	89	200

4.3. TRADE-OFF

4.3.1. TRADE-OFF PROCESS

The material trade-off is performed in two separate steps; in the first step a numerical trade-off focused on material performance will narrow the available material options. The baseline design for the performance is the aluminum LO bracket with a height of 5 mm and a PCB with an E-modulus of 33.4 GPa and a CTE

of 13.9 ppm/K. These PCB properties are determined in appendix D.1. A sensitivity analysis is performed on the criteria weights, and different design parameters. The sensitivity analysis can be found in appendix D.2.

The numerical trade-off yields a few material options. These materials will be investigated further, to determine the manufacturing aspects of these materials. The results are placed in a graphical trade-off, which will result in a final material choice.

4.3.2. TRADE-OFF CRITERIA: MATERIAL PROPERTIES

Before the numerical trade-off on material performance can be made, trade-off criteria need to be defined. The trade-off criteria are related to the density, and the performance of the materials in the models presented in chapter 2 and 3.

DENSITY

The density of the material directly influences the weight of the bracket. Materials were already selected on densities close to, or lower than, the density of copper. The density ratings are given in table 4.4, were the higher densities rate the lowest scores. The performance of the different materials for the baseline design is given in table 4.5.

Table 4.4: Density score table.

Density [g/cm^3]	>9	8-9	7-8	6-7	5-6	4-5	3-4	2-3	1-2	<1
Score	1	2	3	4	5	6	7	8	9	10

Table 4.5: Material density scores.

Material	Density [g/cm^3]	Score
Cu	8.92	2
Al	2.7	8
Ti	3.76	7
Mg	1.81	9
Mo	10.22	1
Kovar	8.36	2
Cu-Diamond	6.3	4
Al-Si	2.54	8
Al-SiC	2.8	8
Al-Graphite	2.5	8

CTE DEFLECTION

The first model presented, see chapter 2.1, describes the deflection of two strips of material bonded together. In this case, the materials are bonded to a strip of 1.6 mm thick PCB with length 16 cm. The PCB has a CTE of 13.9 ppm/K and its E-modulus is 33.4 MPa.

According to ECCS-Q-ST-70-38C [23], the maximum allowed deflection of a PCB is 1.6% of the length of the board. With a length of 16 cm (the PCB is 10mm longer than the bracket alone), this yields a maximum deflection of 2.56 mm. The resulting scoring scale is presented in table 4.6.

Table 4.6: CTE deflection scoring table.

Deflection	[mm]									
Range	>2.25	2-2.25	1.75-2	1.5-1.75	1.25-1.5	1-1.25	0.75-1	0.5-0.75	0.25-0.5	<0.25
Score	1	2	3	4	5	6	7	8	9	10

The deflection due to the CTE mismatch is determined for all the materials. The values and scores are given in table 4.7.

Table 4.7: Deflection scores.

Material	du [mm]	Score
Cu	0.14	10
Al	0.66	8
Ti	0.48	9
Mg	0.92	7
Mo	0.22	10
Kovar	0.44	9
Cu-Diamond	0.27	9
Al-Si	0.03	10
Al-SiC	0.01	10
Al-Graphite	0.41	9

As can be seen from table 4.7, the scores from deflection model yield similar deflections for all materials. The sensitivity analysis, see appendix D, shows even more clustered results for a different bracket height and for different PCB characteristics. All materials score very well and don't come close to the maximum deflection of 2.56 mm. Although this is comforting, this deflection criterion will not provide information regarding the material selection. Therefore, this criterion will be removed from the numerical trade-off.

SOLDER LAYER STRESS

An operational PCB assembly will experience load cycles (thermal and vibrational). These load cycles degrade the the solder layer until a point of failure; thus there is a maximum amount of load cycles the solder layer can handle. This maximum number of cycles decreases if, before the load cycling, stresses are already present in the solder layer. Therefore, solder layer stresses are undesired and should thus be minimized.

A model for the solder stress due to CTE mismatch is presented in chapter 2. This model will be used to evaluate the performance of the materials. The calculated maximum stress should be below the yield stress of the solder layer. For the used solder, Sn63Pb37, the yield strength is unknown. However, the ultimate normal and shear stresses are found to be 52 MPa and 37 MPa respectively[24]. Taking a factor 2 safety margin on the ultimate strengths, the maximum normal and shear stress are found to be 26 MPa and 18.5 MPa respectively. The scoring table 4.8 is based on these maxima. The performance of the materials is shown in table 4.9.

Table 4.8: Solder stress score table.

Normal	Stress	[Mpa]								
Range	>23.4	20.8-23.4	18.2-20.8	15.6-18.2	13-15.6	10.4-13	7.8-10.4	5.2-7.8	2.6-5.2	<2.6
Score	1	2	3	4	5	6	7	8	9	10
Shear	**Stress**	**[Mpa]**								
Range	>16.65	14.8-16.65	12.95-14.8	11.1-12.95	9.25-11.1	7.4-9.25	5.55-7.4	3.7-5.55	1.85-3.7	<1.85
Score	1	2	3	4	5	6	7	8	9	10

Table 4.9: Solder stress scores.

Material	Normal [Mpa]	Score	Shear [MPa]	Score	Combined Score
Cu	4.86	9	3.45	9	9
Al	16.25	4	12.66	4	4
Ti	17.52	4	12.63	4	4
Mg	16.10	4	13.89	3	3.5
Mo	19.24	3	12.48	4	3.5
Kovar	18.70	3	13.03	3	3
Cu-Diamond	19.23	3	12.79	4	3.5
Al-Si	1.33	10	0.96	10	10
Al-SiC	0.19	10	0.13	10	10
Al-Graphite	12.63	6	9.37	5	5.5

COMPONENT TEMPERATURE

As components dissipate power, their temperature starts to rise. These components have maximum temperature requirements, which need to be taken into account in the bracket design. The thermal heat transfer model presented in chapter 3 is able to predict the temperature of the components on the LO board, based on the thermal conductivity of the bracket material. For the trade-off the maximum component temperature is determined for each material. The scoring table 4.10 is based on the highest and lowest values of the calculated component temperatures. The performance of the materials is presented in table 4.11.

Table 4.10: Component temperature scoring table.

T [$^\circ C$]										
Range	>176	172-176	168-172	164-168	160-164	156-160	152-156	148-152	144-148	<144
Score	1	2	3	4	5	6	7	8	9	10

Table 4.11: Component temperature scores.

Material	T [$^\circ C$]	Score
Cu	151.4	8
Al	162.2	5
Ti	182.6	1
Mg	172.2	2
Mo	165.8	4
Kovar	182.5	1
Cu-Diamond	150.4	8
Al-Si	164.9	4
Al-SiC	162.8	5
Al-Graphite	159.9	6

4.3.3. MATERIAL CRITERIA WEIGHT FACTORS

To determine the weight factor of each criterion for the numerical trade-off, the Analytical Hierarchy Process (AHP) is used. This process is based on pairwise comparisons; each criterion is compared to the other criteria separately [25]. These pairwise comparisons create a matrix, of which the eigenvector associated with the largest eigenvalue represents the importance of each criterion.

The pairwise comparison for the numerical trade-off for material properties is given by table D.14.

Table 4.12: Pairwise comparison of the criteria.

	Density	Solder Stress	Temperature
Density	1	2	3
Solder Stress	1/2	1	2
Temperature	1/3	1/2	1

The objective of this thesis is to reduce the mass of the mechanical bracket, the density of materials will be the most important criterion. The solder stress should be as minimum as possible, to increase the number of load cycles it can withstand. This makes this the second most important criterion; the density is weighted twice as heavy as the solder stress. The temperature of the components is an important design aspect, however, the temperatures are determined for a fixed design of the LO board. In the 2-4 GHz bracket design, geometry can be changed, meaning that materials with lower scores might still be adequate. Therefore the density of materials is weighed trice as important than the temperature, while the solder stress is weighed twice as important.

For the pairwise comparison matrix in table D.14, the maximum eigenvalue λ_{max} is equal to 3.0092. The associated eigenvector w is equal to:

$$w = \begin{bmatrix} 0.54 \\ 0.30 \\ 0.16 \end{bmatrix} \tag{4.1}$$

This eigenvector shows the weight factors for each criterion; 0.54 for density, 0.30 for solder stress and 0.16 for the component temperature. However, for these weight factors to hold true the matrix should be consistent and contradictions should be limited.

As example, in this case the density is weighed twice as much as the solder stress and trice as much as the component temperature. One could conclude from this, that the solder stress should weigh one and a half times the component temperature. However, the matrix shows that the solder stress is weighed twice as much as the component temperature. Thus, there is a contradiction causing a inconsistent matrix.

However, creating a fully consistent matrix is difficult. For this reason the Consistency Index (CI) was introduced:

$$CI = \frac{\lambda_{max} - n}{n - 1} \tag{4.2}$$

Studies showed that this CI is not fair in comparing matrices of different order and needs to be re-scaled. For this purpose the Consistency Ratio (CR) is introduced. In this ratio, the CI is divided by a Random Index (RI), see equation 4.3. This RI is the estimation of the average CI obtained from a large enough set of randomly generated matrices. Matrices with an CR 10% should be accepted [25].

$$CR = \frac{CI}{RI} 100\% \tag{4.3}$$

For the matrix of table D.14, the λ_{max} is equal to 3.0092 and the number of elements n is equal to 3. This results in a CI of 0.0046. The RI for a 3x3 matrix is 0.52, which results in a CR of 0.88 %. This means that the matrix should be accepted, and that the weight factors can be used in the trade-off.

4.3.4. TRADE-OFF: MATERIAL PROPERTIES

With the weights factors of each criterion known, and the scores for each criteria known, the final trade-off table 4.13 can be made for the baseline design.

Table 4.13: Numerical trade-off table.

Material	Score	Density 0.54	Solder Stress 0.3	Temperature 0.16	Total
Cu		2	9	8	5.1
Al		8	4	5	6.3
Ti		7	4	1	5.1
Mg		9	3.5	2	6.2
Mo		1	3.5	4	2.2
Kovar		2	3	1	2.1
Cu-Diamond		4	3.5	8	4.5
Al-Si		8	10	4	8.0
Al-SiC		8	10	5	8.1
Al-Graphite		8	5.5	6	6.9

This trade-off is based on the baseline design, with a bracket height of 5 mm and in the calculated PCB properties. The PCB properties might not be exact, while the bracket height might differ in the 2-4 GHz design. Therefore, a sensitivity of these aspects in the trade-off is performed in appendix D.2. The results of this sensitivity analysis are shown in table 4.14.

Table 4.14: Final scores of all the materials.

Material	h=5mm	h=10mm	Reverse
Cu	5.1	5.1	5.4
Al	6.3	6.6	7.2
Ti	5.1	5.3	5.4
Mg	6.2	6.4	7.1
Mo	2.2	2.3	2.7
Kovar	2.1	2.0	2.6
Cu-Diamond	4.5	5.1	4.8
Al-Si	8.0	8.4	7.7
Al-SiC	8.1	8.4	8.1
Al-Graphite	6.9	7.1	7.1

The weight factors are determined using a pairwise comparison matrix, so small changes in these comparisons will lead to different weight factors. To determine the impact of different weight factors, a second sensitivity analysis is performed. This sensitivity analysis is for the baseline design, but with changed pairwise comparison matrices. The entire analysis can be found in appendix D.3, the results are shown in table 4.15.

Table 4.15: Sensitivity analysis of the AHP.

Material	Normal	Option1	Option2	Option3
Cu	5.1	4.3	5.9	5.3
Al	6.3	7.4	6.3	6.8
Ti	5.1	5.6	4.9	4.8
Mg	6.2	6.9	5.7	5.9
Mo	2.2	1.9	2.5	2.4
Kovar	2.1	2.1	2.3	2
Cu-Diamond	4.5	4.4	4.3	4.9
Al-Si	8.0	8.0	8.3	7.5
Al-SiC	8.1	8.1	8.4	7.8
Al-Graphite	6.9	7.2	6.6	6.9

The trade-off, including the sensitivity analysis, show that 2 materials score best; aluminum-silicon and aluminum-silicon carbide. These materials will be used in a second trade-off, which also focuses on manufacturing aspects. To give a feeling on the relative performance, aluminum also included in this second trade-off.

4.3.5. TRADE-OFF CRITERIA: MANUFACTURING

The second trade-off is used to converge to a final material choice. In this trade-off manufacturing aspects such as cost, availability, rework and risk will be added in the trade-off criteria. Because most of these aspects do not include specific numbers, the trade-off will be performed graphically. The trade-off criteria for the second trade-off are described below.

MATERIAL PERFORMANCE

A detailed trade-off for material performance was performed in the previous section. The material properties still remain the main selection criterion and are therefore also used in this second trade-off. However, in a graphical trade-off different aspects of the material performance can be highlighted.

PRODUCTION COST

The production cost are also a selection criterion for the material choice. The maximum production cost for the hardware is €10,000. This not a killer limit, production costs above this limit will still be considered only the weight factor will increase. Below this limit, the actual cost are small compared to an entire assembled PCB and are therefore of less importance. It should be noted that these production cost exclude the cost for the design personnel.

AVAILABILITY

Material availability is an criterion related to the time schedule. The PCB layout and bracket design will most likely performed simultaneously, and will be finished at the same moment. Because the assembly of the electrical components and bracket will be performed in one sweep, the maximum lead time of the bracket should be equal to the maximum lead time of electrical flight components. For flight components the lead time is typically 2 months, resulting in a maxium lead time for the bracket production of 2 months. This includes the order and delivery of the material, the time for the actual production and the time required for the coating of the bracket.

REWORK

During the assembly phase, last minute design changes to the bracket might occur. Electrical components might be changed, or are hard to access. Modification of the bracket should therefore be optional in the assembly phase. Modification can be done in-house or can be outsourced. Outsourcing means additional cost and a longer lead time, which are undesired. Therefore, SRON strongly prefers in-house rework capabilities with the existing machinery.

RISK

An important aspect for space products is the risk associated with the product. One way of assessing the risk associated with a product is assessing the maturity of the technology. The maturity of a product can be measured by the Technology Readiness Level (TRL). However, for materials it is difficult to find a TRL. This is because materials themselves are rarely space qualified because of the costs associated with the qualification. In most cases the qualification will be done for an entire product, rather than for only the material. To still gain an impression of the maturity of the material, an TRL will be estimated for this trade-off.

4.3.6. MANUFACTURING CRITERIA WEIGHT FACTORS

The weight factors of the criteria for this second graphical trade-off will also be determined by the AHP process. Table 4.16 shows the relative weights of the criteria.

Table 4.16: Relative weights of the manufacturing criteria.

	Material properties	Cost	Availability	Rework	Risk
Material properties	1	8	3	3	5
Cost	1/8	1	1/3	1/3	1/2
Availability	1/3	3	1	1	2
Rework	1/3	3	1	1	2
Risk	1/5	2	1/2	1/2	1

The main selection criteria, will still be the material properties because it is all about the performance of the material. For this reason, it has relative large pairwise comparison values. Production cost is considered to be the least important criterion, as long the maximum of €10,000 is not exceeded. If this this maximum would be exceeded, the criterion would become more important. The availability of the material and the rework criteria are equally scored. A good availability of the material allows for flexibility in the time schedule, while in-house rework capabilities allow for flexibility in the (re)design. In this thesis new materials for this kind of space application are considered, thus the risks should be kept in mind when selecting a material. The eigenvector of the pairwise comparison matrix 4.16.

$$w = \begin{bmatrix} 0.50 \\ 0.06 \\ 0.17 \\ 0.17 \\ 0.10 \end{bmatrix} \tag{4.4}$$

The maximum eigenvalue λ_{max} is equal to 5.0793. The RI for n=5 is equal to 1.11. These values are filled in equation 4.2 and 4.3, which gives a CI of 0.0198 and a CR of 1.79%. The matrix is thus consistent and the eigenvector can be used for the weights. This yields a weight of 50% for the material properties, 6% for the cost, 17% for the availability, 17% for the rework and 10% for the risk. The sensitivity of the pairwise comparison is analyzed in appendix D, and shows that changes to the matrix only result in minor changes in the weight factors for the criteria.

4.3.7. TRADE-OFF: MANUFACTURING

ALUMINUM

Aluminum is a widely used material in space flight, the TRL is therefore estimated on 9. The material has a large CTE mismatch with the PCB, causing large solder layer stresses. There are plenty of manufacturers available for delivery, with a lead time of 1 week and material costs of €100. The machining of the bracket will take 2 weeks and €300, for the application of the coating an additional 1 week and €150 should be reserved. SRON is used to work with Aluminum, machinery is on-site available thus the rework can be performed in-house.

ALUMINUM SILICON

The use of aluminum silicon is being studied and proposed for applications[16, 26], therefore the TRL is estimated to be 6. The material has an excellent CTE match with the PCB, combined with a good thermal performance. There are several manufacturers available world-wide, one of them in the Netherlands. The lead time for Aluminum Silicon is 3 weeks, with a material cost of €500. The production techniques used on this material are the same as for aluminum. This means that the production times, cost and in-house rework capabilities are identical to aluminum.

ALUMINUM SILICON CARBIDE

Aluminum silicon carbide is currently being used the thermal management of power semiconductors in spacecraft [27], only one reference for this was found thus the TRL is estimated on 7. The material performance of this material is similar to aluminum silicon. The number of manufacturers of aluminum silicon carbide is limited. The material cost is €500, with a lead time of 3 weeks. The production of the bracket can be done in 2 weeks, however the production cost are high; €1500. The reason for this is the hardness of the material, requiring special machining tools and causing high wear on them. Only one company was found who could machine aluminum silicon carbide in Europe. This also has as consequence that possible rework needs to be outsourced.

GRAPHICAL TRADE-OFF

The graphical trade-off table shows the advantages, in green, and disadvantages, in red, of each material. The column widths match the weight factor of each criteria, enabling a quick visual method to determine the performance of the material.

Table 4.17: Trade-off Manufacturing

Material	Material Properties	Cost	Availibilty	Lead Time	Risk
Al	Large CTE mismatch PCB	450	Plenty	4 weeks	TRL 9
AlSi	Excellent CTE match PCB	950	Several	6 weeks	TRL 6
AlSiC	Excellent CTE match PCB	2150	One	6 weeks	TRL 7

Comparing the Al-Si and Al-SiC shows a preference for Al-Si. This is because the hardness of the Al-SiC causes special tooling and high tooling wear, which results in few manufacturers and higher production cost. Aluminum is an easy available, low cost material to use. However, when compared to the Al-Si and Al-SiC it lacks the material performance. All in all, Al-Si shows the best material performance in combination with manufacturing aspects, without coming with a large drawback. The material choice for the 2-4 GHz bracket is therefore aluminum silicon.

5

2-4 GHz Board Design

5.1. Design Aspects

5.1.1. PCB Layout Limitations

One of the limitation in this thesis is that the PCB layout which will not be changed. Not changing the PCB layout means that the components, traces and screw holes are at fixed places. Figure 5.1 shows the location of these elements. To allow rework on the components the minimum distance between a bracket wall and component is 2 mm.

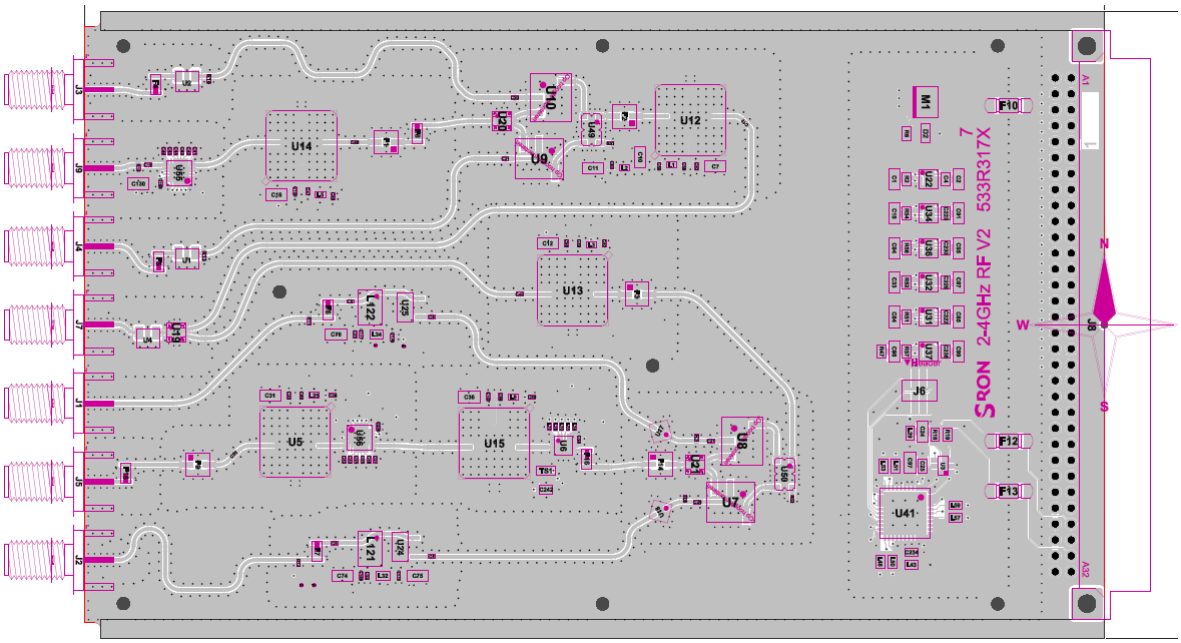

Figure 5.1: The PCB layout showing the components, traces and screw holes.

Another aspect of the PCB layout is the available solder area for the bracket. The bracket is soldered to the top copper layer of the PCB, thus the exposed copper areas determine the contour of the bracket. Within this contour, bracket walls can be made smaller, or even left out. Figure 5.2 shows the bare PCB of the 2-4 GHz board. The figure shows the gold plated copper which is available for soldering. One can identify the wall contour, traces, screw holes, smaller and larger components.

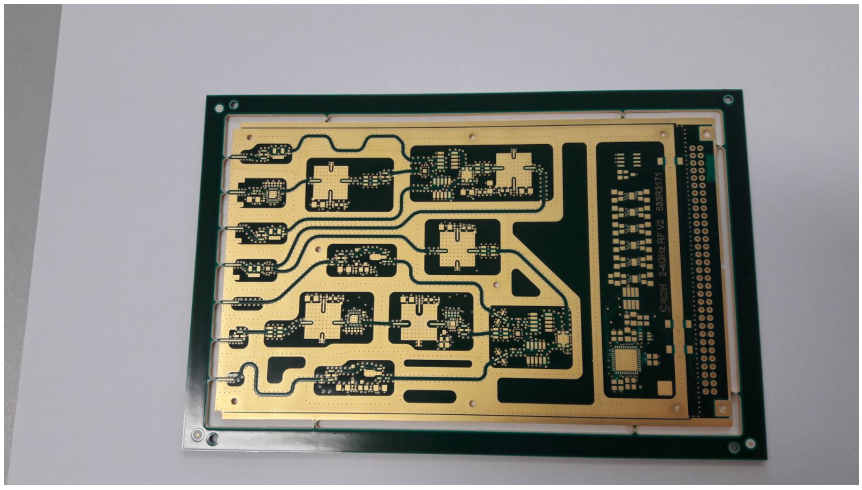

Figure 5.2: A picture of the bare PCB.

5.1.2. Geometrical Limitations

The height of the bracket is determined by the largest electrical component. As flight components can differ in size with test components, an actual flight component of TROPOMI is used as reference. This component has a height of 9 mm [28]. The lid should not touch the electrical components, therefore a 1 mm distance between lid and components is specified, resulting in a minimum bracket height of 10 mm.

During the machining of the bracket, when the milling cutter moves along the wall which is being cut out, the milling cutter exerts a small out of plane force on the wall. For thick walls this is not a problem, but for thin-walled structures this force might cause curvature of the wall. The length of the wall also impacts this effect; longer walls will experience larger curvatures. In consultation with the instrument makers and mechanical department at SRON, it was decided that the minimal wall thickness should be 1 mm.

The last geometrical aspect, is the groove at the outside of the bracket. This groove, shown on the LO-board in figure 5.3, is used to slide a PCB assembly into the framework used for testing. Because the 2-4 GHz board is still in development, it is required to have this groove. In a final flight-ready design this can be omitted.

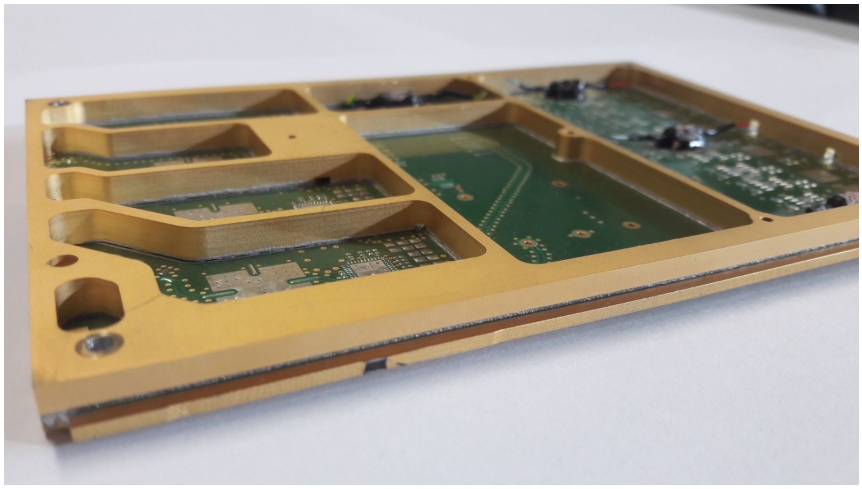

Figure 5.3: The groove on the outside of the LO-board.

5.1.3. EMC RESONANCES

To avoid interference between critical parts or components on the circuit, enclosures are placed around them. These enclosures are called cavities. Within such a cavity, resonance of the electromagnetic waves can occur; standing waves in the field can be formed between opposite sides, when the dimension between the sides is a multiple of $\lambda/2$, see figure 5.4 [11]. The electric field is enhanced in the middle of the cavity and due to the perpendicular nature of electromagnetic radiation the magnetic field is enhanced at the sides.

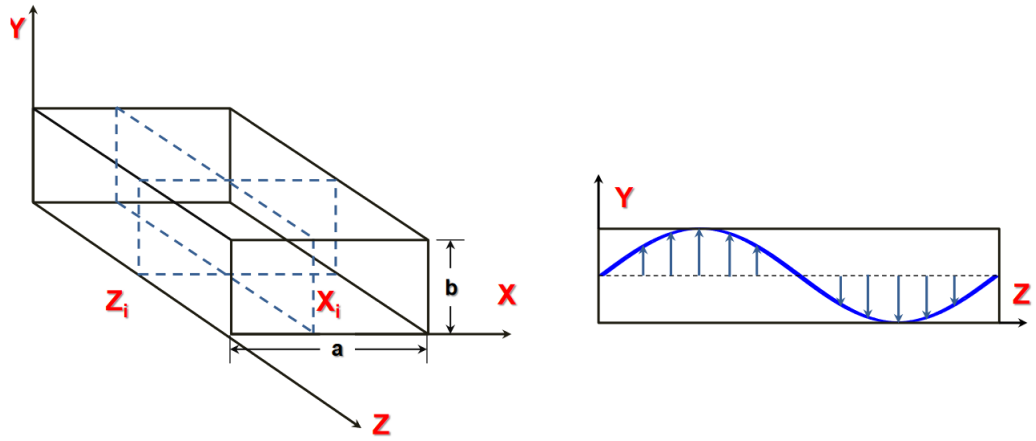

Figure 5.4: Resonance in cavities [29]

For an empty cavity, resonance occurs at [11]:

$$f = 150\sqrt{\left[\left(\frac{k}{l}\right)^2 + \left(\frac{m}{h}\right)^2 + \left(\frac{n}{w}\right)^2\right]} \tag{5.1}$$

With l, h and w (m) the enclosure dimensions, k, m and n wave modes (positive integers, but no more than one can be equal to 0 at the time) and the resonance frequency f (MHz) [11]. When a cavity is loaded with components however, equation 5.1 will not be valid. Thomas 1999 [30] showed that components and conducting structures will detune the resonances and reduce the amplitude. Equation 5.1 will be used to determine the maximum cavity enclosures, while loading the cavity with components further reduces the resonance effect. In this way a natural safety margin is created. For the 2-4 GHz board, the location of high frequency components, all with a maximum operating frequency of 4000 MHz, that require shielding are shown in figure 5.5.

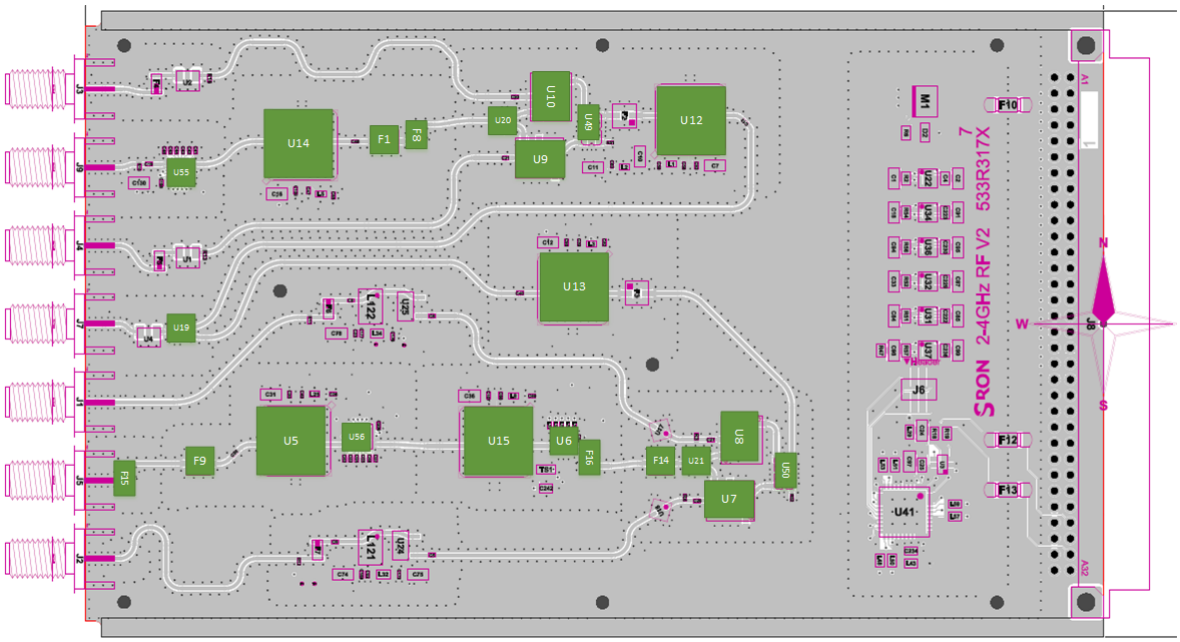

Figure 5.5: The high frequency components on the 2-4GHz board.

5.1.4. EMC Reflections

To prevent radiated emissions, requirements on the attenuation of the housing were specified in chapter 4. The PCB and bracket attenuate the radiated emissions to the bottom and sides. To attenuate the radiated emissions to the top, a lid will be necessary. Screwing a lid directly to the bracket leaves gaps, through which the emissions can travel. Placing a gasket between the bracket and lid will close these gaps, creating a sealed box. Another option would be to solder the lid to the bracket. However, this is an undesired solution because no rework can be done on the PCB.

Therefore, an EMC gasket needs to be placed on the outer edge of the bracket. The mechanical department of SRON is familiar with the use of Spirashield as EMC gasket for electronic housings, while for cryogenic projects Indium gaskets are used. Indium gaskets are slightly toxic, and require special regulations when used. Because ECSS-Q-ST-70C clause 5.1.5a states that no materials can be used that form a hazard to personell, this gasket is not considered further. The EMC gasket of choice is thus Spirashield. It should be noted that this thesis provides several rationales on EMC design, however no actual EMC analysis is performed. The performance of other types of EMC gaskets can therefore not properly be evaluated and will be left for further research.

Spirashield, shown in figure 5.6b, is a spiral which is wound out of spring temper beryllium copper [31]. This spiral is placed in a groove, and will be compressed by screwing the lid on. Ideally, Spirashield will be placed in a dovetail groove to prevent the compressed Spirashield from popping out when the lid is unscrewed.

(a) [31].

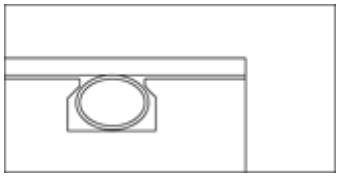

(b) [31].

To compress the Spirashield, a number of screws need to be used. Spirashield gives equation 5.2, which can be used to determine the screw spacing [31]

$$L = 0.80 \left[\frac{480 Y R t^3 d}{13F_1 + 2F_2} \right]^{1/4} \tag{5.2}$$

As Spirashield is an U.S. product, the units for equation 5.2 are imperial. In equation 5.2 Y [$inch$] is the width of the cover edge (which should be taken to 1 $inch$ if this is not distinct), t [$inch$] is the thickness of the cover edge, d [$inch$] the deflection of the gasket. The deflection of the gasket should be 20% of its diameter. The smallest available Spirashield has a diameter of 0.034 $inch$. F_1 and F_2 represent the minimum and maximum force of the gasket on the cover. These are predefined values, F_1 is 4 $pounds/inch$ and F_2 is 30 $pounds/inch$. The 0.80 before the equation expresses a safety factor advised by Spirashield. Converting the units to imperial, and back again, yields a screw distance of 46.0 mm.

With this outside gasket, the external emissions are attenuated. However, the addition of a lid will also create internal reflections. The impact of these internal reflections on the performance of the board is unknown and difficult to predict. Making female edges on the lid, shown in figure 5.7, will eliminate the direct reflections. This would provide an easy way to improve the performance. However, if such a solution is sufficient or if heavier EMC measurements are required can only be determined via test. Such a test can not be done within the time span of this project, but should be tested in further research.

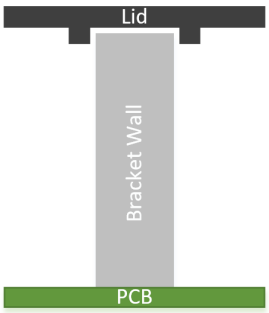

Figure 5.7: Female edges on the lid would increase the EMC performance and would thus provide a possible design solution for the lid.

5.2. 2-4 GHz DESIGN

5.2.1. THERMAL MODEL

DISSIPATING COMPONENTS

The most dissipating components are identified by an electrical engineer as input for the heat transfer model. The locations of the components are indicated in figure 5.8. For each component, a maximum junction temperature can be found in the component datasheet. The junction temperature is the highest temperature which the component is allowed to achieve. The junction temperature is derated according to ECSS-Q-ST-30-11C [32]. The component datasheets provide beside the maximum junction temperature also the thermal resistance between the junction and the PCB. The An overview of the components characteristics is given in table 5.1.

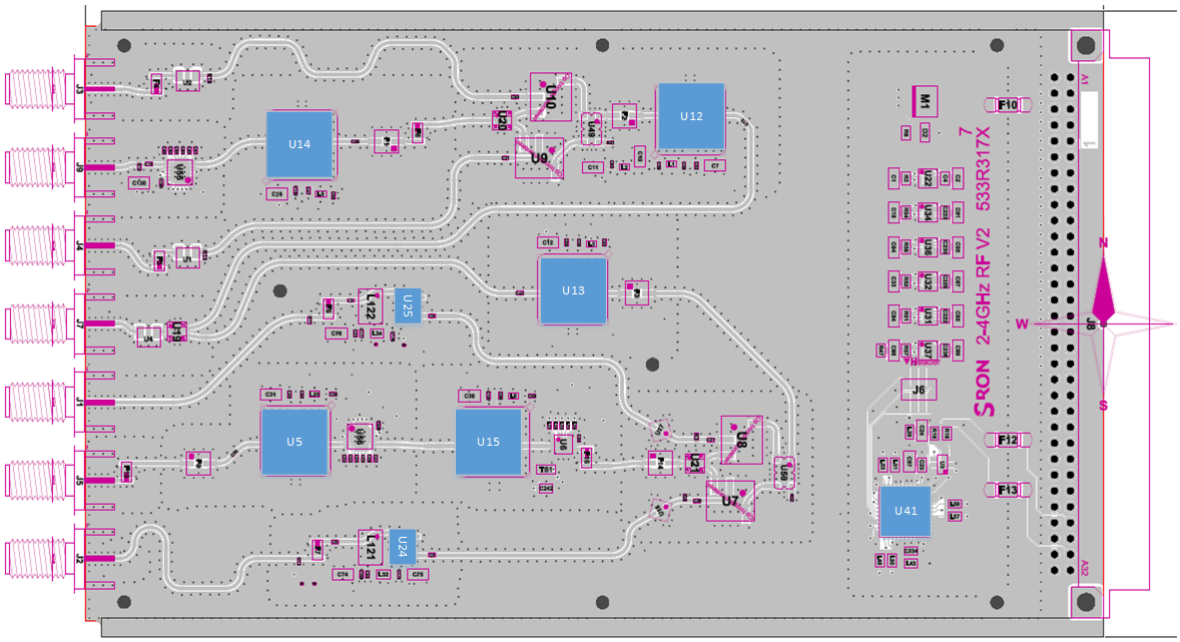

Figure 5.8: The most dissipating components on the 2-4GHz board.

Table 5.1: Most dissipating components of the 2-4 GHz board.

Component	Identifier	$P_{Dissipation}[W]$	$T_{Junction}[°C]$	$T_{Derated}[°C]$	$R_{Package}$[K/W]
HMC741ST89E [33]	U24,U25	0.72	150	110	97.83
SMA4011 [34]	U5, U12, U13, U14	0.56	125	100	47
TN9240 [35]	U15	1.3	-	110	52.5
PIC16f887 [36]	U41	1.2	150	110	24.4

Heat Transfer Model

The heat transfer model for the LO board, presented in chapter 3, is adapted for the 2-4 GHz board. Nodes are added to resemble the contour of the frame, which is determined by the available solder area as shown in section 5.1.1. The material used in the 2-4 GHz design is aluminum silicon, which has a thermal conductivity of 135 W/mK.

The thermal model of the LO board included the thermal resistance of the glue, which was used to attach the heaters. For the 2-4 GHz board this thermal resistance of the glue will be replaced by the actual thermal resistance $R_{Package}$ between the PCB and the junction of the component, as specified in table 5.1. The dissipation of the heaters is also matched with the dissipation of the components.

Table 5.1 also shows the derated junction temperature. Due to model inaccuracy, a safety margin of 5 $°C$ is taken on this derated junction temperature. The heat sink is attached to the four corners of the 2-4 GHz bracket.

5.2.2. Design Approach

The starting point for the design was the minimum bracket height of 10 mm, and the frame contour given by the solder area. Because the material was already chosen, the design approach was focused on minimizing the volume of the bracket while keeping the component temperature below the maximum temperature. Volume reduction is achieved by reducing the cross sectional areas of the bracket walls, or in some cases removing the wall entirely. During this volume reduction process EMC resonances within the cavities must

be taken into account. After several iterations, the final 2-4 GHz bracket design is shown in figure 5.9. This bracket has a mass of 74 gr.

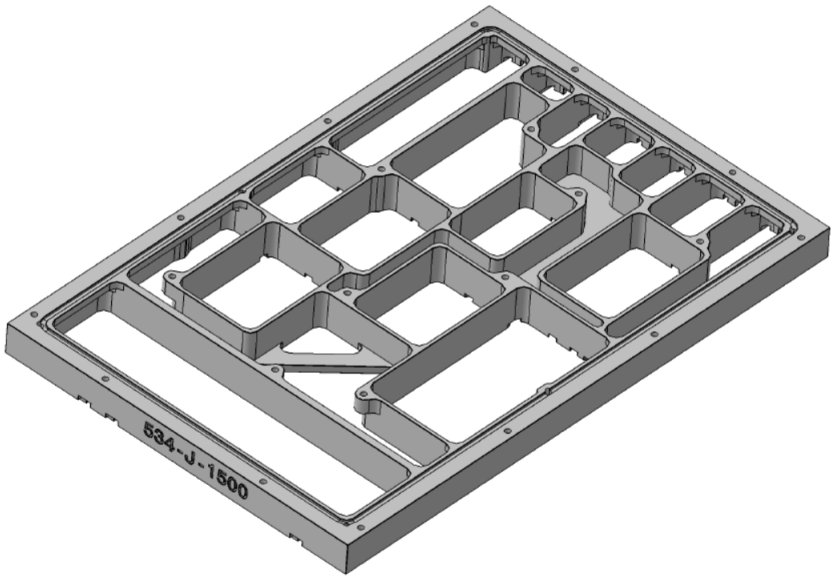

Figure 5.9: The final 2-4 GHz bracket design.

The component temperatures for this bracket are shown in table 5.2.

Table 5.2: Component temperatures on the 2-4 GHz board at 0 $mbar$..

Component	T Design [$°C$]	T model [$°C$]
U5	95	58.6
U12	95	56.8
U13	95	59.3
U14	95	57
U15	105	100.3
U24	105	95.3
U25	105	99.7
U41	105	61.3

During the design iterations for the bracket, it became clear that the bracket design does not influence the component temperature that much. The model showed that in vacuum, 78% of the dissipated heat is conducted and 22 % of the heat is radiated. Because most of the dissipation is through conduction, the component temperature is mostly determined by the total thermal resistance between the component and heat sink. In its most simple form, the the total thermal resistance for a component can be viewed as shown in figure 5.10.

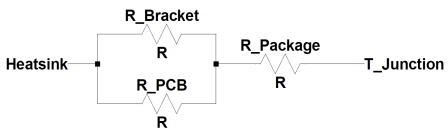

Figure 5.10: The most simple representation of the total thermal resistance.

Figure 5.10 shows that the package type of the component, which determines the $R_{Package}$, has a huge influence on the junction temperature. The hottest components of table 5.2 have the largest thermal resistances, shown in table 5.1. This means that changing the volume of the bracket, thus the thermal resistance of the bracket, has just little impact on the temperature of the component. This resulted in a design, were all the bracket walls are made as thin as possible. Even with this thin walled configuration, table 5.2 shows that the model temperature are lower than the design temperatures allow. This means that the components will not gain a too high temperature. However, due to the relative large temperature difference between the model temperatures and design temperatures one can conclude that the design is not thermally optimized.

5.2.3. DETAILS OF THE 2-4GHz BRACKET

This resulting 2-4 GHz bracket design contains a lot of details, which will be pointed out and described in the remainder of this section. Figure 5.11 shows the top view of the bracket, which will be used to show several details.

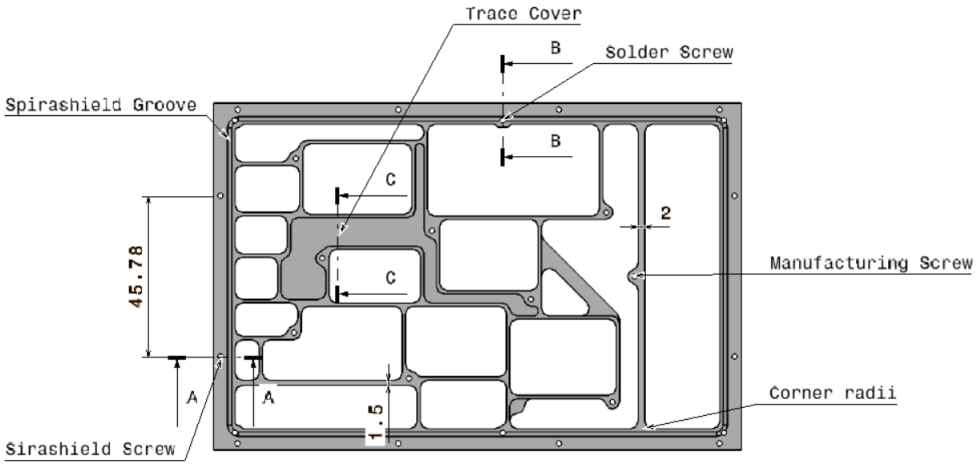

Figure 5.11: Top view of the 2-4 GHz bracket design.

SPIRASHIELD

The Spirashield is used to attenuate the radiated emissions. For increased shielding quality, the screws fixating the Spirashield should be located at the outside of the groove. Figure 5.11 also shows that the screw distance is 45.8 mm, which is below the required 46.0 mm. The cross section of such an outer bracket wall, view A-A in figure 5.11, is shown in figure 5.12. This cross section shows the screw hole with thread and the Spirashield groove. The minimum wall thickness of 1 mm is applied around the screw hole and groove, resulting in such a layered cross section.

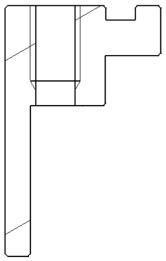

Figure 5.12: Cross section showing the Spirashield groove and screw hole including thread.

SOLDER SCREW

There is a slight difference between the screws used for fixating the Spirashield and the screws used for fixating the bracket during soldering. The thread of the screws for located for the Spirashield at the top of the bracket, while the thread for the for the soldering screws is located at the bottom of the bracket. This is shown in figure 5.13. In the bottom right corner of this figure one can also identify the cut out for the outside groove of the bracket, which will be used the slide the 2-4 GHz into its testing framework.

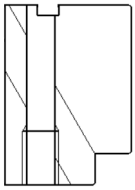

Figure 5.13: Cross section showing the solder screw hole including thread.

TRACE COVER

Traces carry electronic signals, thus electromagnetic waves, from one functional group to another. Therefore traces need to be treated as components, thus ensuring that different traces do not interfere with each other. Also, EMC resonance is applicable for traces. Due to these EMC aspects, traces need to be shielded. An example of such a trace cover is shown in figure 5.14.

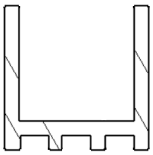

Figure 5.14: Cross section of a trace covers.

MANUFACTURING ASPECTS

The thermal model showed that cavity walls with a 1 mm thickness would be sufficient to stay below the design temperature of the components. However, the out of plane force exerted by the milling cutter, could cause curvature of the longer walls. In consultation with the instrument makers at SRON it was decided to prevent this, by increasing the thickness of these longer walls. This resulted in thickness changes of two walls, the thicknesses are indicated in figure 5.11. As extra precaution, an extra screw hole (the 'Manufacturing Screw') is added. This can be used to screw the bracket to the milling machine, creating a fixed point, which reduces the effective length of the wall.

Brackets of this size are typically machined using milling cutter with a 2 mm radius. During the machining, the milling cutter forms a line contact with the surface being cut away. If the radius of the corners would also be 2 mm, the milling machine would temporally stop in the corner. This would create a surface contact with the milling cutter, in which scratches due to the vibration of the milling machine would be visible. To create a smooth surface in the corners, a line contact is desired. This is achieved by slightly increasing the corner radii to 2.1 mm.

EMC RESONANCES

The location of the high frequency components is shown in figure 5.5. These components will be situated in cavities 1-9, as indicated in figure 5.15. The resonance frequency of these cavities is determined using equation 5.1; by varying the integers k, m and n in this equation the minimum resonance frequency is determined.

Waves with a higher frequency, will experience resonance in the cavity. Therefore, the maximum operating frequency of the components should be below the minimum resonance frequency. Table 5.3 shows that with the cavity dimensions of the final design EMC resonances are avoided.

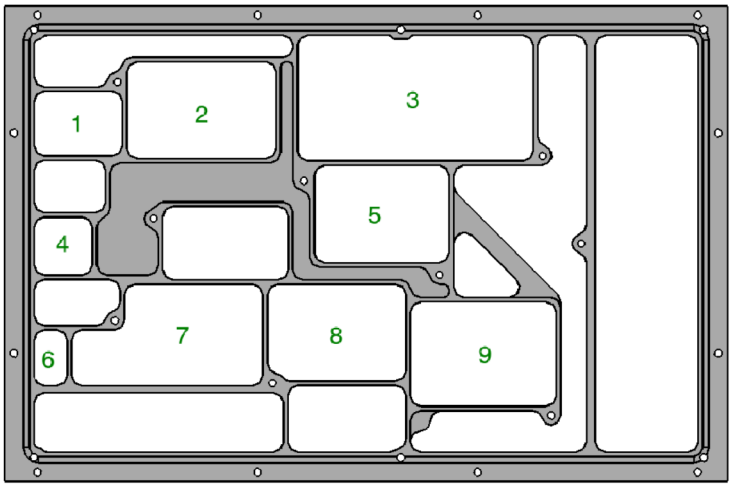

Figure 5.15: Cavities containing high frequency components.

Table 5.3: Cavity resonances.

Cavity	l [mm]	w [mm]	h [mm]	$f_{Resonance}$[GHz]	$f_{operating}$[GHz]
1	23.7	13.5	10	12.787	4.000
2	31.2	20.2	10	8.846	4.000
3	49.2	29.3	10	5.966	4.000
4	17.5	12.2	10	15.002	4.000
5	28.2	20.4	10	9.075	4.000
6	12.2	11.7	10	17.763	4.000
7	40.00	21.2	10	8.010	4.000
8	29.00	20.2	10	8.957	4.000
9	30.5	21.8	10	8.460	4.000

5.3. Testing

5.3.1. Test Setup

For the testing of the 2-4 GHz, a test setup similar to the test setup presented in chapter 3.4 will be used. Although designed for actual dissipating amplifiers and regulators, using a fully operational board would increase the complexity and cost of the test drastically. Protocols to ensure that the amplifiers and regulators are used at their designed intensity and the power supply to the board are some of the aspects that would need to be considered.

The test setup of chapter 3.4 will therefore be replicated as much as possible. Minor changes will be incorporated to further improve the test setup. The heaters in the LO board testing were resistors, with a round external surface. This made the estimation for the thermal resistance of the glue difficult. To improve this, SMD resistors will be used. The difference between the resistors is shown in figures 5.16a and 5.16b.

(a) Resistor attachment to the LO board.

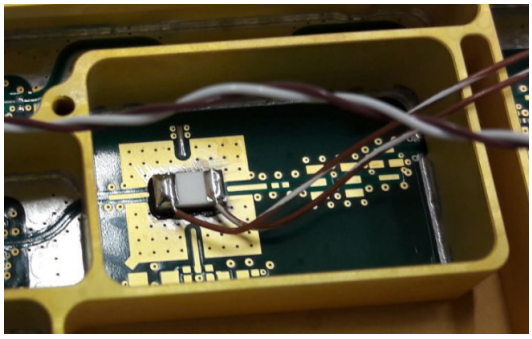

(b) SMD attachment to the 2-4 GHz board.

The SMD resistors will act as heaters during the test. The location of the heaters is shown in figure 5.17. Heaters R6 and R8 will dissipate 1.2 W, while the other heaters will dissipate 0.6 W. These dissipations should resemble the actual dissipation of the components, shown in table 5.1.

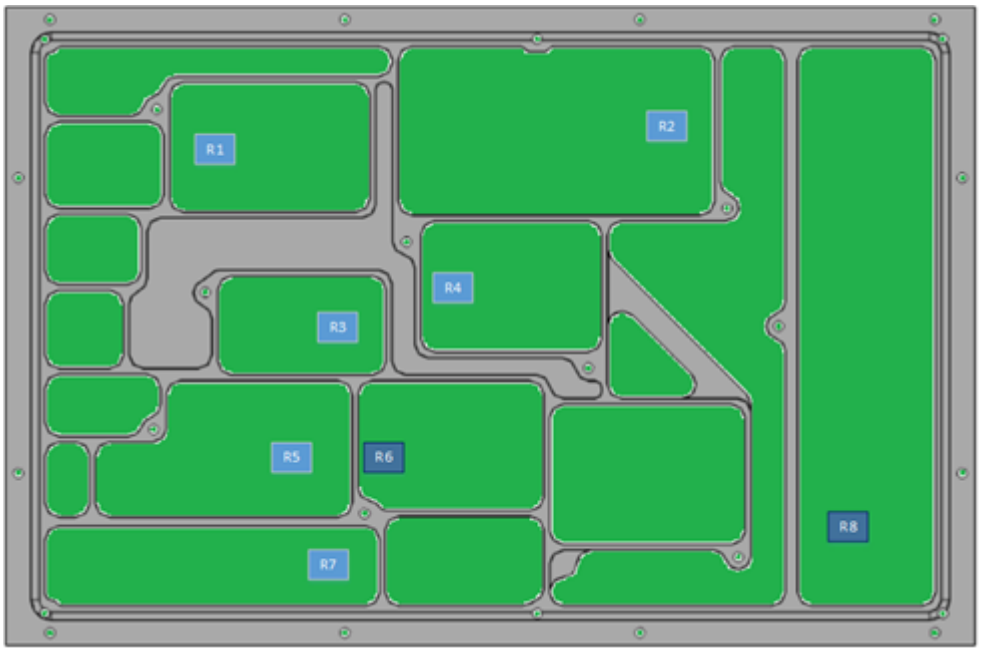

Figure 5.17: The location of the heaters on the 2-4 GHz board.

During the LO board testing, thermal pads were used to improve the connection between the thermocouple and measurement spot. The thermocouple is pushed into the soft thermal pad. Movements of the thermocouple would create voids in the soft pad, which decreases the connection between thermocouple and measurement spot. If these voids were to large, the pad would require replacement. This is avoided by gluing the thermocouple to the measurement spot. A drawback of this method is the decreasing flexibility; thermocouples can not be relocated. To avoid extra tension on the glue connection when connecting the test setup, a cabling support structure is added to the PCB. A picture of this cabling support structure is shown in figure 5.18.

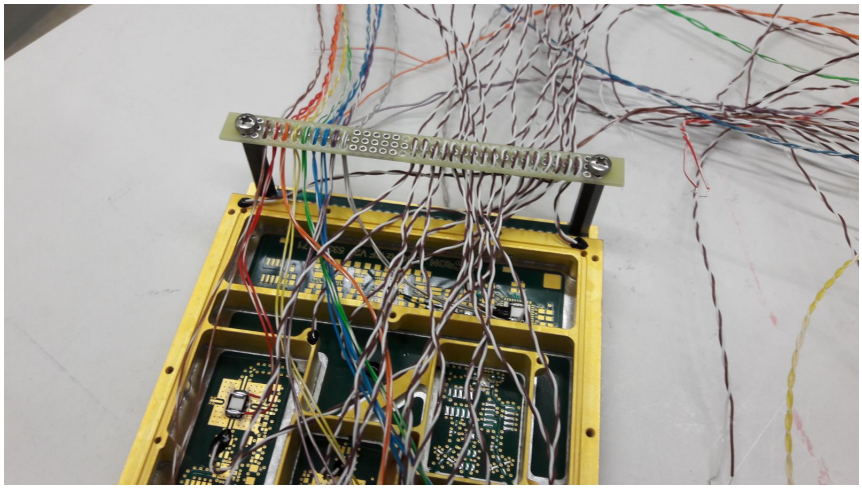

Figure 5.18: Cabling support structure on the test setup.

The location of the thermocouples on the 2-4 GHz board is shown in figure 5.19. Several thermocouples are attached next to the heater, and not on top. The reason for this is the large difference between the thermal resistance of the packaging type of the actual component, and the thermal resistance of the glue used to attach the heaters. The measured temperature on the heater would not resemble the temperature of the component. However, the combined thermal resistance of the PCB and bracket should be the same in both cases. The PCB and bracket are after all not changed. This means that the temperature of the PCB, measured close to the heater, should be similar in both cases.

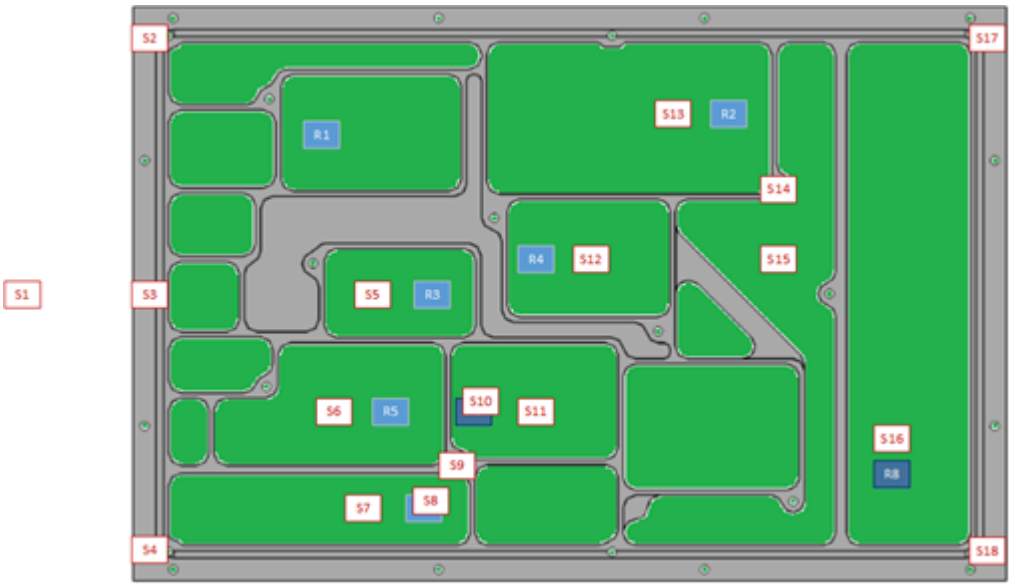

Figure 5.19: The location of the thermocouples on the 2-4 GHz board.

The test setup will be placed in the same vacuum chamber which was used for the LO board testing. During the test, the heaters will be placed in series and are connected to a constant current source located outside the vacuum chamber. A picture of the entire test setup is shown in figure 5.20.

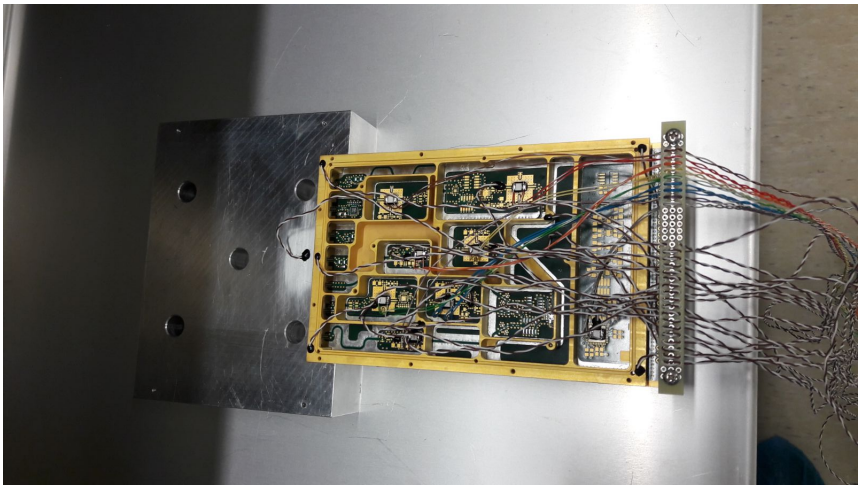

Figure 5.20: The test setup for the 2-4 GHz board.

THERMAL MODEL

To above described test setup changes will cause differences in the thermal model of the 2-4 GHz board, described in section 5.2.1. The bracket will not be changed, however the inputs will vary. The dissipation of the components shown in table 5.1 will be replaced by the dissipation of the SMD resistors. The junction to lead thermal resistance of the components is not valid anymore, which will be replaced by the thermal resistance of the glue used to attach the SMD resistor.

5.3.2. TEST RESULTS

The predicted and measured temperatures of the 2-4 GHz board are shown in table 5.4 for a pressure of 1013 $mbar$ and in table 5.5 for a pressure of 20 $mbar$. A selection of thermocouple measurements which should represent the temperature distrubtion over the 2-4 GHz board are shown, the measurements of all the thermocouples can be found in appendix E.

Table 5.4: Temperatures of the thermocouples at 1013 $mbar$.

Location	Model Temperature [$^\circ C$]	Measured Temperature [$^\circ C$]	Error [$^\circ C$]
S1	21.6	21.4	0.2
S4	23.7	26.3	-2.6
S9	30.5	33.1	-2.6
S10	40.6	46.2	-5.6
S17	29.7	30.8	-1.1

Table 5.5: Temperatures of the thermocouples at 20 $mbar$.

Location	Model Temperature [$^\circ C$]	Measured Temperature [$^\circ C$]	Error [$^\circ C$]
S1	22.2	23.4	-1.2
S4	25.1	30.5	-5.4
S9	34.2	37.9	-3.7
S10	45.9	51.2	-5.3
S17	35	36.4	-1.4

The first thing that can be noticed is the much lower temperature of the heater, when compared to the expected temperature of the component specified in table 5.2. This can be contributed to the large difference in thermal resistance between the thermal resistance of the packaging type of the actual component, and the thermal resistance of the glue used to attach the heaters.

Both models show that the measured temperature is higher than the model temperature. For a pressure of 1013 $mbar$ this error is about 3 $^{\circ}C$ while for a 20 $mbar$ pressure this error increases to 4 $^{\circ}C$. The negative errors are an indication that the conduction of the bracket in the model is overestimated, leading to lower expected temperatures.

There are several factors that contribute to this. An factor of importance is the connection between the 2-4 GHz and the heatsink. Errors in estimating the thermal resistance between the 2-4 GHz board and the heatsink will cause temperature deviations over the entire board. It seems that the LO board had a better connection to the heat sink, the measured temperature difference between the S1 and S4 thermocouples is about 2 $^{\circ}C$ lower. Because the 2-4 GHz board used the same settings as the LO board, this difference of 2 $^{\circ}C$ will be propagate over the entire board.

Further, the LTSpice model uses nodes the determine the heat flows. The actual geometry of the bracket is thus forced into the LTSpice grid. For the LO board, which was a relatively easy structure, this yielded little problems. The design of the 2-4 GHz board however, contains more cavities and and complex shapes. Forcing the 2-4 GHz geometry will lead to larger errors.

Although there might be an overestimation on the conduction capabilities of the 2-4 GHz board which needs to be sorted out, the overall performance of the bracket will be adequate. The 2-4 GHz bracket was not temperature optimized due to the minimum wall thickness, which resulted in large error margins; the maximum temperature of the hottest component, U15, was expected to be 100.3 $^{\circ}C$ while its derated component temperature is 110 $^{\circ}C$. This shows that even though the measured temperatures are higher than the expected values, they are still within the large design margin.

6

CONCLUSIONS AND RECOMMENDATIONS

6.1. CONCLUSIONS

As the introduction stated, the research objective of this thesis is to improve the current design of the RF-system by redesigning the mechanical bracket to significantly reduce its mass, while keeping similar performance with respect to the current bracket design. This is done by answering the research questions, the sub questions will be answered first followed by the answer to the main research question.

What is the effect of a CTE mismatch between bracket and PCB?
An important structural aspect is the CTE mismatch between bracket and PCB. When the PCB assembly is cooled down from its solder temperature to room temperature, the CTE mismatch will cause bending of the PCB assembly. The deflection of such a CTE mismatch is analyzed for two bonded strips of material with different CTE. Analysis showed that besides the CTE, the thickness ratio impacts the deflection. A higher thickness ratio shows lower deflections.

Another model was formulated, aimed at describing the solder layer stresses caused by the CTE mismatch. This model showed that the normal and shear stresses will peak towards the end of the strip, were higher thickness ratios show higher peak stresses. Comparing both model results, indicates a connection between the deflection and the solder layer stresses. The energy which is added by the temperature difference, is either reflected in a larger deflection or higher peak stresses in the solder layer.

It should be noted that the analytical model for determining the shear stress in the solder layer showed deficiencies at low thickness ratios. The reason for this has yet to be determined. However, at higher thickness ratios the model seems accurate. Typically, the bracket is much thicker than the PCB, causing high thickness ratios. Therefore, the influence of this deficiency on the remainder of this thesis is little.

What is the impact of the mechanical bracket on the thermal housekeeping?
In vacuum, 78 % of the heat flow will be via conduction. This means, that temperature gradient of the electrical component will be mainly determined by the thermal resistance between the component and heat sink. For the 2-4 GHz board, the largest temperature would be gained by decreasing the thermal resistance of the package type of the electronic component. The thermal resistance of the package type is taken as a component property in this thesis, and could thus not be changed. The effect of the bracket design, was thermally speaking, not of great importance for the maximum temperatures of the components on the 2-4 GHz board. However, for actual flight components it can be expected that the thermal resistance of the packaging type will be much lower. In such cases, the bracket design will be more important for the temperature gradients.

Which material is best suited for the mechanical bracket?
A material selection is made based on a numerical trade-off and a graphical trade-off. The by industry frequently used metal alloys and new advanced composites are analyzed on their material performance. The material performance is analyzed using the deflection, solder layer stress and thermal heat transfer models. These results were compared in a numerical trade-off, which showed that aluminum silicon and aluminum silicon carbide would perform best. These materials showed a low density, good thermal conductivity and excellent CTE match with the PCB.

Both materials are compared in a second, graphical trade-off which included manufacturing criteria. As reference material, normal aluminum was included in this trade-off as well. This showed the the aluminum silicon carbide is an extremely hard material which is difficult to machine, while the machining of aluminum silicon can be done by equipment used for regular aluminum machining. Therefore, aluminum silicon is selected as bracket material.

Which electromagnetic compatibility aspects influence the design of the mechanical bracket?
The contour of the mechanical bracket is large determined by the EMC resonances. High frequency components can interfere with other components, and components should therefore be shielded from each other. This is done by placing the high frequency components in cavities. Within these cavities, EMC resonances can occur. By designing the dimension of the cavity such that the resonance frequency of the cavity is larger than the frequency of the components, EMC resonances can be avoided. This design principle was already used in the original bracket, thus the EMC performance of both brackets will be similar because they are built according to the same design philosophy.

However, ESA requires that radiated emissions should be attenuated. Both designs are open structures, which means that for a flight ready board a lid needs to be added. Screwing a lid directly to the bracket leaves gaps, through which the emissions can travel. Placing a gasket between the bracket and lid will close these gaps, creating a sealed box. The bracket design accounts for the use of Spirashield as a gasket to attenuate radiated emissions.

How can all design aspects be incorporated in the structural design of a low mass mechanical bracket?
Because the material was already chosen, the design approach could be focused on minimizing the volume of the bracket while keeping the component temperature below the maximum temperature. Volume reduction is achieved by reducing the cross sectional areas of the bracket walls, or in some cases removing the wall entirely. During this design process EMC resonances, manufacturing and assembly aspects are taken into account.

With all the sub-questions answered, the main research question can be addressed.

How much mass reduction can be achieved by redesigning the mechanical bracket without compromising on structural, thermal and electromagnetic compatibility performance?
The starting point of this thesis was the original copper bracket with a mass of 920 g. By selecting aluminum silicon, a material with a much lower density than copper, the first step of the mass reduction was achieved. By applying the design approach described above, a thin walled bracket was designed which has similar performance when compared to the original bracket. This new bracket has a mass of 74 g, which is only 8 % of the mass of the original bracket. The mass reduction is thus 846 g, or 92 % of the original mass.

6.2. RECOMMENDATIONS

The analytical model for the shear stress in the solder layer is not accurate at low thickness ratios. This was not of great influence for the design of the 2-4 GHz bracket, but there is still an unexplained error in the analytical model which should be addressed.

During the testing the ambient temperature decreased by 1 $^{\circ}C$ when a vacuum was drawn in the chamber. Although the effect is minimal, an exact formulation of this thermodynamic phenomena was not found in this thesis.

For the material selection a condition was implied that the density of the materials should be lower than that of copper. There might exist materials with a larger density but with much better material properties, requiring less volume and thus provide a possibly lighter bracket. Also, the materials should be electrically conductive for EMC performance and thermally conductive for the thermal performance. A hybrid solution, separating both functions, should also be investigated.

The thermal heat transfer model presented in this thesis is made in the software package LTSpice. Although thermal modelling in LTSpice is possible and gives great insights, LTSpice is impractical to use. The software package can be used for thermal analysis of simple 2D structures. But as soon as the structures become more complex, or the model would become 3D, the thermal analysis would become extremely difficult. The use of actual thermal modelling software, with a more user friendly interface, would provide an alternative.

This thesis focussed on the thermal aspects of the bracket design. A few rationales were applied for EMC design, but this should of course be modeled and tested as well. The same goes for an extensive structural analysis; SRON engineers expect that the solder layer should hold vibrations and shock loads, which are aspects that also need to be proven to create a flight ready 2-4 Ghz board.

BIBLIOGRAPHY

[1] J. van Rantwijk, M. Grim, D. van Loon, S. Yates, A. Baryshev, and J. Baselmans, *Multiplexed readout for 1000-pixel arrays of microwave kinetic inductance detectors,* IEEE Transactions on Microwave Theory and Techniques **64**, 1876 (2016).

[2] S. Timoshenko, *Analysis of bi-metal thermostats,* JOSA **11**, 233 (1925).

[3] W. Chen and C. Nelson, *Thermal stress in bonded joints,* IBM Journal of Research and Development **23**, 179 (1979).

[4] M. Grim, *Projects within SRON,* Company presentation (2016).

[5] Antimicrobial Copper, *A Guido to Working With Copper and Copper Alloys,* url = https://www.copper.org/publications/pub_list/pdf/a1360.pdf (Visited on 16-03-18).

[6] Glemco, *6061-t6 aluminum,* url = http://www2.glemco.com/pdf/NEW_MARTERIAL_LIST/Alumina%20 6061-T6.pdf (Visited on 16-03-18).

[7] X. C. Tong, *Advanced materials for thermal management of electronic packaging,* Vol. 30 (Springer Science & Business Media, 2011).

[8] A. Jamnia, *Practical guide to the packaging of electronics: thermal and mechanical design and analysis* (CRC Press, 2008).

[9] *Cooling of electronic equipment,* url=http://highered.mheducation.com/sites/dl/free/0073398187/835 451/Chapter15.pdf (Visited on 16-03-18).

[10] J. F. O'Hanlon, *A user's guide to vacuum technology* (John Wiley & Sons, 2005).

[11] T. Williams, *EMC for product designers* (Newnes, 2016).

[12] C. Kalde, *SCIAMACHY EMC REQUIREMENTS SPECIFICATION*, SRON Netherlands Institute for Space Research.

[13] European Cooperation for Space Standardization, *ECSS-Q-ST-70-71C Space product assurance: Materials, processes and their data selection,* (15 October 2014).

[14] European Cooperation for Space Standardization, *ECSS-Q-ST-70C Space product assurance: Materials, mechanical parts and processes,* (6 March 2009).

[15] J. Barcena, J. Maudes, M. Vellvehi, X. Jorda, I. Obieta, C. Guraya, L. Bilbao, C. Jimenez, C. Merveille, and J. Coleto, *Innovative packaging solution for power and thermal management of wide-bandgap semiconductor devices in space applications,* Acta Astronautica **62**, 422 (2008).

[16] L. Del Castillo, J. P. Hoffman, and G. Birur, *Advanced housing materials for extreme space applications,* in *Aerospace Conference, 2011 IEEE* (IEEE, 2011) pp. 1–6.

[17] Flowserve, *Titanium alloy data sheet,* url = https://www.flowserve.com/sites/default/files/2016-07/bulletin_A11.pdf (Visited on 16-03-18).

[18] Wellcharter, *Magnesium alloy material data sheet,* url = http://www.wellcharter.com/Magnesium/Mag _Data_Sheet.htm (Visited on 16-03-18).

[19] MatWeb, *Goodfellow TZM Molybdenum High Temperature Alloy,* url = http://www.matweb.com/search/datasheettext.aspx?matguid=26a71059c46d4e09ba1ad9b933b35354 (Visited on 16-03-18).

[20] MatWeb, *Carpenter kovar alloy,* url = http://www.matweb.com/search/datasheettext.aspx?matguid=c2fa45c3446f485692fc97b4b0962ac9 (Visited on 16-03-18).

[21] DoD, *Composite Materials Handbook Volume 4: Metal Matrix Composites* (Department of Defence, 2002).

[22] S. P. Rawal, *Metal-matrix composites for space applications,* JOM Journal of the Minerals, Metals and Materials Society **53**, 14 (2001).

[23] European Cooperation for Space Standardization, *ECSS-Q-ST-70-38C Space product assurance: High-reliability soldering for surface-mount and mixed technology,* (31 July 2008).

[24] MatWeb, *Eutectic solder (63sn-37pb),* url = http://www.matweb.com/search/datasheetText.aspx?bassnum=MLSS63 (Visited on 16-03-18).

[25] M. Brunelli, *Introduction to the analytic hierarchy process* (Springer, 2014).

[26] S. Weinshanker, *High performance, lightweight, hermatic alsi packages for military, aerospace and space applications,* Workshop (2004).

[27] A. B. Pandey, K. L. Kendig, and T. J. Watson, *Affordable Metal Matrix Composites for High Performance Applications II* (John Wiley & Sons, 2013).

[28] Maxwell Technologies, *7809lp,* url=http://www.maxwell.com/images/documents/7809lp_09_10_12_rev_11.pdf, Component Datasheet.

[29] E. V. Colla, *Microwave cavaties,* University of Illinois Physics 401 (2015).

[30] D. W. Thomas, A. Denton, T. Konefal, T. Benson, C. Christopoulos, J. Dawson, A. Marvin, and J. Porter, *Characterisation of the shielding effectiveness of loaded equipment enclosures,* in *Electromagnetic Compatibility, 1999. EMC York 99. International Conference and Exhibition on (Conf. Publ. No. 464)* (IET, 1999) pp. 89–94.

[31] Spira, *Spirashield,* url=http://www.spira-emi.com/products/sshield.htm (Visited on 16-03-18), Spirashield product information.

[32] European Cooperation for Space Standardization, *ECSS-Q-ST-30-11C Derating - EEE Components,* (4 October 2011).

[33] Analog Devices, *Ad9754,* url=http://www.analog.com/media/en/technical-documentation/data-sheets/AD9754.pdf, Component Datasheet.

[34] Macom, *Sma4011,* url=https://cdn.macom.com/datasheets/A4011_SMA4011.pdf, Component Datasheet.

[35] Api technologies corp., *Tn9240,* url=http://micro.apitech.com/pdf/amplifier/tn9240.pdf, Component Datasheet.

[36] Microchip, *Pic16f882,* url=http://ww1.microchip.com/downloads/en/DeviceDoc/41291D.pdf, Component Datasheet.

[37] J. Gao, *The physics of superconducting microwave resonators* (California Institute of Technology, 2008).

[38] J. Baselmans, *Microwave kinetic inductance detectors,* Company presentation (2016).

[39] FLIR, *Emissivity pcb, url=http://flir.custhelp.com/app/answers/detail/a_id/1281/̃emissivity-settings-when-imaging-pcbs-and-electronics,* (Visited on 16-03-18).

[40] Emerson & Cuming, *Stycast 2850,* url=https://lartpc-docdb.fnal.gov/0000/000059/001/stycas2850.pdf, Material Datasheet.

[41] C. Decolon, *Analysis of composite structures* (Butterworth-Heinemann, 2004).

A

MICROWAVE KINETIC INDUCTANCE DETECTORS

Over the last decades, low temperature detectors (temperatures below 1K) have been of great interest for the astronomy community. These low temperature detectors have ultra-high sensitivity, which gave astronomers revolutionary new observational capabilities [37]. One of these detectors, is the Microwave Kinetic Inductance Detector (MKID).

The working principle of the MKID is based on breaking up Cooper pairs in a resonance circuit. In a superconductor, Cooper pairs can move freely without being scattered . These Cooper pairs carry the supercurrent. At small temperatures, a small fraction of the electrons are thermally excited from the Cooper pair state. These thermally excited Cooper pairs are called quasiparticles [37]. These quasiparticles carry a normal current [38]. The ratio of Cooper pairs to quasiparticles characterize the resonance of the incoming spectrum.

If the incoming spectrum changes, for example it becomes lighter. If the Cooper pairs are hit by a photon with sufficient energy from this brighter spectrum, the Cooper pair will break up. This absorption causes an excess of quasiparticles, which changes the ratio of Cooper pairs to quasiparticles. This results in a change in resonance peak and resonance frequency [38]. This is visualized in figure A.1.

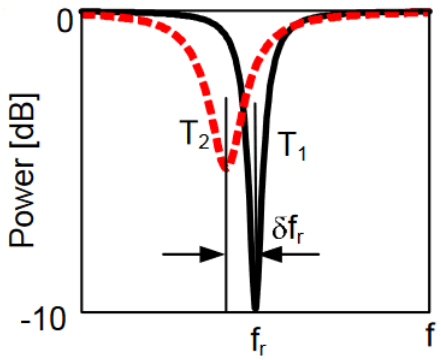

Figure A.1: The transmission through a resonance circuit [37]. The black line indicates a darker spectrum and the red dotted line indicates a lighter spectrum.

A single MKID is built out of an antenna, a central line and a resonator as can be seen in figure A.2. The antenna focuses the incoming spectrum, which is send through the central line. In this central line, the breaking up of the Cooper pairs occurs due to the radiation absorption. the breaking up of Cooper pairs happens in this central line. At the end of the central line is the resonator, which configures the resonance frequency of a single MKID. By changing the length of the resonator, one can set the specific resonance frequency. In a MKID array, all these individual MKIDs are tuned for a different resonance frequency and connected to a feedline. By tuning the resonance frequencies of the individual MKIDs, one can analyze the spectrum over the desired frequency range.

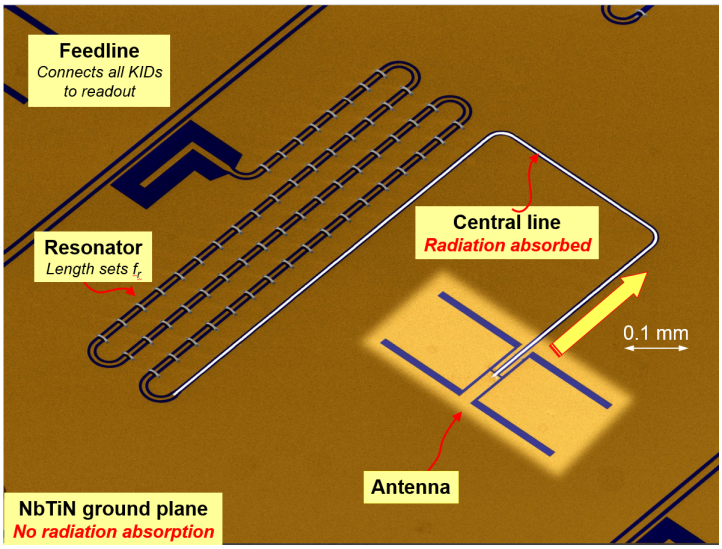

Figure A.2: Individual elements of a KID [38].

SRON developed such a MKID operating in the 2-4 GHz band. The read out principle of these MKID are described by van Rantwijk et al. [1], however these exact electronic workings are beyond the scope of this thesis. In this paper the system architecture is presented which visualizes nicely the connection between the MKID and the RF-board, which is the topic of my thesis. Figure A.3 shows this system architecture which shows the required (electronic) steps for the operation of the MKID array. To operate the MKID one needs four different electronic boards; a Digital-Analog Converter (DAC) board, an Analog-Digital Converter (ADC) board, a Local Oscilator (LO) board and a Radio Frequency (RF) board. In this thesis the existing LO board will be used to built the thermal heat transfer model, which in turn will be used to design a mechanical bracket for the RF board.

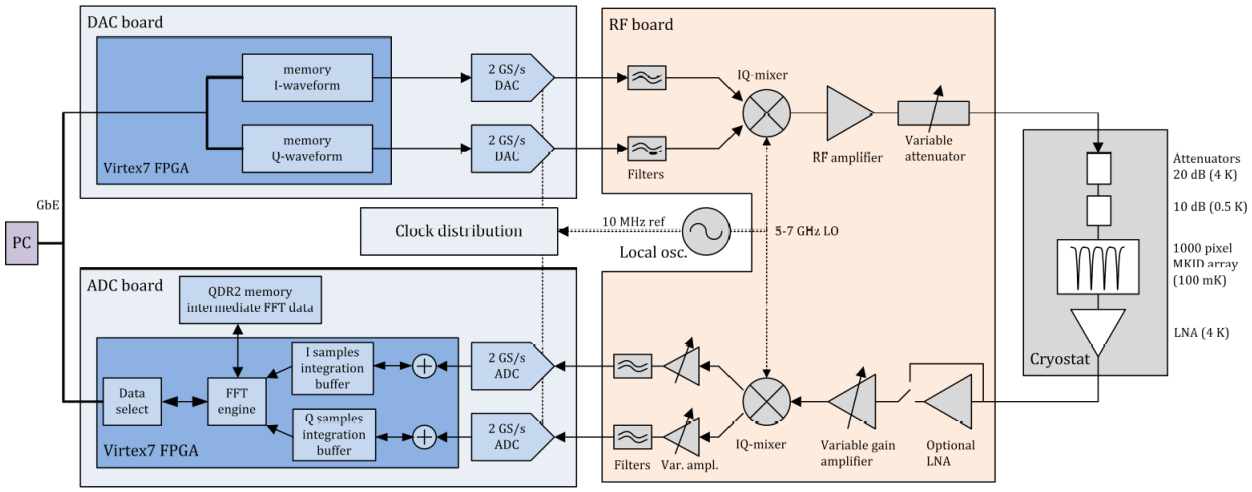

Figure A.3: The SRON MKID architecture, the digital electronics are shown in blue, the RF electronics in orange and the cryostat with MKID array in grey [1]

B

CTE ANALYSIS

B.1. TIMOSHENKO DERIVATION

In this section the entire derivation of the deflection du of bonded strips, presented in chapter 2.1, is shown. The analysis of the deflection of a strip containing two bonded materials, with different CTE, is based on the analysis of Timoshenko [2]. This theory is based on several ideal conditions; such as a constant CTE of the materials during heating, friction at the supports can be neglected and the width of the strip is considered to be very small. A narrow strip of two metals is bonded together and uniformly heated. Due to the difference in CTE between the two metals the strip will experience bending, as can be seen in figure B.1

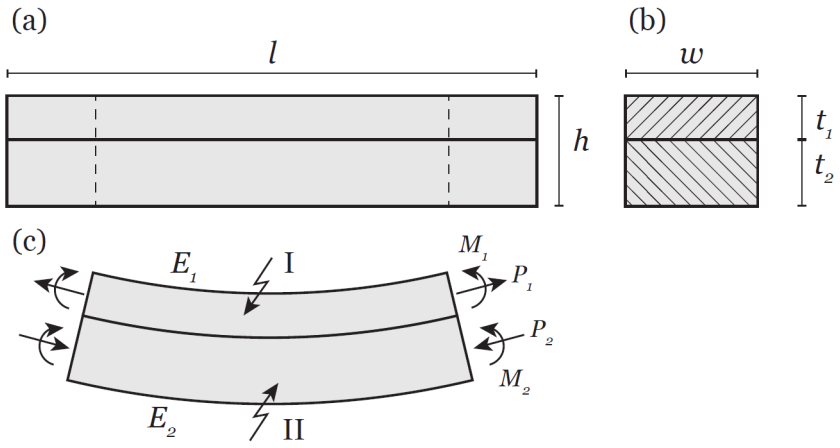

Figure B.1: Deflection of a bi-metal strip while uniformly heated. [2]

In the following analysis α_1 and α_2 denote the CTE of the two metals, E_1 and E_2 their Young's moduli, t_1 and t_2 their thickness and h the height of the strip.

To simplify the analysis, the width of the strip is taken to be unity. There are no external forces acting on the strip, thus there must be a force and moment equilibrium:

$$P_1 = P_2 = P \tag{B.1}$$

$$\frac{Ph}{2} = M_1 + M_2 \tag{B.2}$$

The moments can be expressed as:

$$M_i = \frac{E_i I_i}{\rho} \tag{B.3}$$

Where M_i denotes the moment on material i, E_i the Young's modulus of material i, I_i the moment of inertia of material i and ρ the radius of curvature of the bonded strip. Substituting equation B.3 in equation B.2 yields:

$$\frac{Ph}{2} = \frac{E_1 I_1 + E_2 I_2}{\rho} \tag{B.4}$$

Considering the deformation of the strip, another equation for the force P and the radius of curvature ρ can be found. The unit elongation occurring at the bearing surface of each layer in the longitudinal direction of the strip must be equal:

$$\alpha_1 \Delta T + \frac{P_1}{E_1 t_1} + \frac{\alpha_1}{2\rho} = \alpha_2 \Delta T + \frac{P_2}{E_2 t_2} + \frac{\alpha_2}{2\rho} \tag{B.5}$$

To visualize this equation, consider that the thermal expansion induces bending and internal tensile and compressing forces. $\alpha \Delta T$ expresses the internal tensile force, the $\frac{P}{Et}$ the internal compressing force and the $\frac{\alpha}{2\rho}$ shows the bending forces. The radius of curvature ρ can be found by substituting equations B.1 and B.4 in B.5 and rewriting for ρ:

$$\frac{1}{\rho} = \frac{(\alpha_2 - \alpha_1)}{\frac{h}{2} + \frac{2(E_1 I_1 + E_2 I_2}{h}\left(\frac{1}{E_1 t_1} + \frac{1}{E_2 t_2}\right)} \tag{B.6}$$

Remembering that the moment of inertia of layer i is given by:

$$I_i = \frac{t_i^3}{12} \tag{B.7}$$

Substituting equations B.7 in equation B.6, results in a general equation for the radius of curvature of a bi-metal strip:

$$\frac{1}{\rho} = \frac{6(\alpha_2 - \alpha_1)(1+m)^2 \Delta T}{h\left(3(1+m)^2 + (1+mn)\left(m^2 + \frac{1}{mn}\right)\right)} \tag{B.8}$$

To simply the expression of the radius of curvature, the following constants were introduced:

$$m = \frac{t_1}{t_2}, n = \frac{E_1}{E_2} \tag{B.9}$$

The last step is to convert this radius of curvature to a deflection of the bonded strip. Figure 2.2 depicts the bending of the bonded strip.

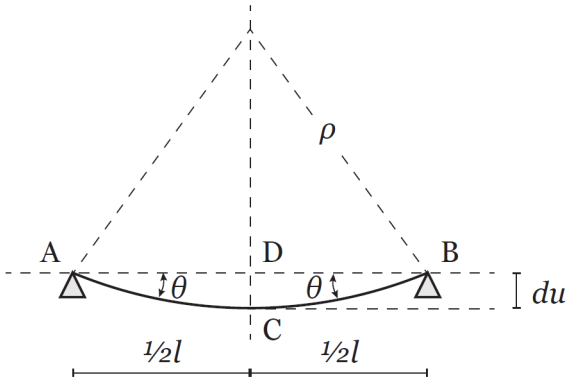

Figure B.2: Deflection of a strip. [2]

The deflection of the strip will be small when compared to the length of the strip. Therefore the small angle approximation is applied, which assumes that the arc length of the strip is equal to the horizontal length of the strip. With this assumption, the deflection du [m] can be determined by equation B.10.

$$du = \rho - \sqrt{\rho^2 - l^2} \tag{B.10}$$

B.2. TIMOSHENKO MATLAB CODE

```
clear all
close all
clc
%% Input
% Solder
w = 170e-3; %[m]
l = w/2; %[m]


% Material 1
E1 = 118e3; %[MPa]
t1 = 2e-3; %[m]
alpha1 = 16.8e-6; %[-]
I1 = (t1^3)/12;


% Material 2
E2 = 68.9e3; %[MPa]
t2 = 1.5e-3; %[m]
alpha2 = 23.6e-6; %[-]
I2 = (t2^3)/12;


% Temperature
T = 183-25; %[degC]
```

```
%% Timoshenko
m = t1/t2;
n = E1./E2;
h = t1+t2;
rho1 = ( 6*(alpha2-alpha1)*T*(1+m)^2 )./( h*(3*((1+m)^2)+(1+m.*n).*((m^2)+(1./(m.*n)))) );
rho = 1./rho1;


% Moment and Forces
M1 = E1*I1/rho;
M2 = E2*I2/rho;
F = (2/h)*(M1+M2);


% Deflection
x = [-l:1e-3:l];
dv_max = rho - sqrt(rho.^2 - l^2);
dv_max_mm = dv_max*1e3;
```

B.3. CHEN DERIVATION

Chen considers the case where the layers are separated by an amount η. This gap is filled with a material capable of deforming under shear and tension, figure B.3(a) shows the model setup.

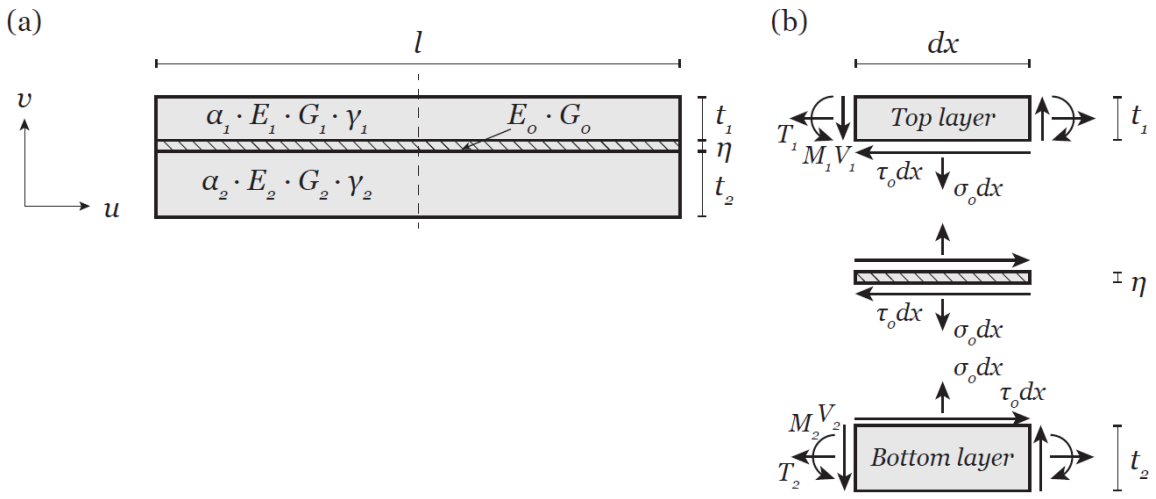

Figure B.3: (a) Chen's model setup. (b) The forces and moments acting on each a section dx. (c) The applicable axis system. [3]

Because there are no external forces acting on the strip, the force and moment equations are in equilibrium for both layers. this results in:

Formulation of stress analyis problem
Moment equilibrium:

$$\frac{dM_1}{dx} - V_1 + \tau_0 \frac{t_1}{2} = 0 \tag{B.11}$$

$$\frac{dM_2}{dx} - V_2 + \tau_0 \frac{t_2}{2} = 0 \tag{B.12}$$

Horizontal forces:

$$\frac{dT_1}{dx} - \tau_0 = 0 \tag{B.13}$$

$$\frac{dT_2}{dx} + \tau_0 = 0 \tag{B.14}$$

Vertical forces:

$$\frac{dV_1}{dx} - \sigma_0 = 0 \tag{B.15}$$

$$\frac{dV_2}{dx} + \sigma_0 = 0 \tag{B.16}$$

Displacements in u-direction:

$$\frac{du_1}{dx} = \frac{\left(1-\gamma_1^2\right)T_1}{E_1 t_1} - \frac{6\left(1-\gamma_1^2\right)M_1}{E_1 t_1^2} + \left(1+\gamma_1\right)\alpha_1 \Delta T \tag{B.17}$$

$$\frac{du_2}{dx} = \frac{\left(1-\gamma_2^2\right)T_2}{E_2 t_2} + \frac{6\left(1-\gamma_2^2\right)M_2}{E_2 t_2^2} + \left(1+\gamma_2\right)\alpha_2 \Delta T \tag{B.18}$$

Displacements in v-direction:

$$\frac{d^2 v_1}{dx^2} = -\frac{M_1}{D_1} \tag{B.19}$$

$$\frac{d^2 v_2}{dx^2} = -\frac{M_2}{D_2} \tag{B.20}$$

where

$$D_i = \frac{E_i t_i^3}{12\left(1-\gamma_i^2\right)} \tag{B.21}$$

Stress in joint:

$$\frac{\tau_0}{G_0} = \frac{u_1 - u_2}{\eta} \tag{B.22}$$

and

$$\frac{\sigma_0}{E_0} = \frac{v_1 - v_2}{\eta} \tag{B.23}$$

Shear stress analysis
Rewrite equation B.22

$$\frac{\eta}{G_0}\tau_0 = u_1 - u_2 \tag{B.24}$$

Differentiate

$$\frac{\eta}{G_0}\frac{d\tau_0}{dx} = \frac{du_1}{dx} - \frac{du_2}{dx} \tag{B.25}$$

Implement equations B.17 and B.18

$$\frac{\eta}{G_0}\frac{d\tau_0}{dx} = \frac{\left(1-\gamma_1^2\right)}{E_1 t_1} T_1 - \frac{6\left(1-\gamma_1^2\right)}{E_1 t_1^2} M_1 + \left(1+\gamma_1\right)\alpha_1 \Delta T - \frac{\left(1-\gamma_2^2\right)}{E_2 t_2} T_2 - \frac{6\left(1-\gamma_2^2\right)}{E_2 t_2^2} M_2 - \left(1+\gamma_2\right)\alpha_2 \Delta T \tag{B.26}$$

Differentiate

$$\frac{\eta}{G_0}\frac{d^2\tau_0}{dx^2} = \frac{\left(1-\gamma_1^2\right)}{E_1 t_1}\frac{dT_1}{dx} - \frac{6\left(1-\gamma_1^2\right)}{E_1 t_1^2}\frac{dM_1}{dx} - \frac{\left(1-\gamma_2^2\right)}{E_2 t_2}\frac{dT_2}{dx} - \frac{6\left(1-\gamma_2^2\right)}{E_2 t_2^2}\frac{dM_2}{dx} \tag{B.27}$$

Rewrite equations B.13 and B.14

$$\frac{dT_1}{dx} = \tau_0 \tag{B.28}$$

$$\frac{dT_2}{dx} = -\tau_0 \tag{B.29}$$

Implement equations B.28 and B.29 in equation B.27

$$\frac{\eta}{G_0}\frac{d^2\tau_0}{dx^2} = \frac{\left(1-\gamma_1^2\right)}{E_1 t_1}\tau_0 - \frac{6\left(1-\gamma_1^2\right)}{E_1 t_1^2}\frac{dM_1}{dx} + \frac{\left(1-\gamma_2^2\right)}{E_2 t_2}\tau_0 - \frac{6\left(1-\gamma_2^2\right)}{E_2 t_2^2}\frac{dM_2}{dx} \tag{B.30}$$

Rewrite equation B.30

$$\frac{\eta}{G_0}\frac{d^2\tau_0}{dx^2} = \left[\frac{\left(1-\gamma_1^2\right)}{E_1 t_1} + \frac{\left(1-\gamma_2^2\right)}{E_2 t_2}\right]\tau_0 - \frac{6\left(1-\gamma_1^2\right)}{E_1 t_1^2}\frac{dM_1}{dx} - \frac{6\left(1-\gamma_2^2\right)}{E_2 t_2^2}\frac{dM_2}{dx} \tag{B.31}$$

Rewrite equations B.11 and B.12

$$\frac{dM_1}{dx} = V_1 - \tau_0\frac{t_1}{2} \tag{B.32}$$

$$\frac{dM_2}{dx} = V_2 - \tau_0\frac{t_2}{2} \tag{B.33}$$

Implement equations B.32 and B.33 in equation B.31

$$\frac{\eta}{G_0}\frac{d^2\tau_0}{dx^2} = \left[\frac{\left(1-\gamma_1^2\right)}{E_1 t_1} + \frac{\left(1-\gamma_2^2\right)}{E_2 t_2}\right]\tau_0 - \frac{6\left(1-\gamma_1^2\right)}{E_1 t_1^2}\left[V_1 - \tau_0\frac{t_1}{2}\right] - \frac{6\left(1-\gamma_2^2\right)}{E_2 t_2^2}\left[V_2 - \tau_0\frac{t_2}{2}\right] \tag{B.34}$$

Rewrite

$$\frac{\eta}{G_0}\frac{d^2\tau_0}{dx^2} = \left[\frac{4\left(1-\gamma_1^2\right)}{E_1 t_1} + \frac{4\left(1-\gamma_2^2\right)}{E_2 t_2}\right]\tau_0 - \frac{6\left(1-\gamma_1^2\right)}{E_1 t_1^2}V_1 - \frac{6\left(1-\gamma_2^2\right)}{E_2 t_2^2}V_2 \tag{B.35}$$

Define constant c

$$c = 4\left[\frac{\left(1-\gamma_1^2\right)}{E_1 t_1} + \frac{\left(1-\gamma_2^2\right)}{E_2 t_2}\right] \tag{B.36}$$

Implement constant c in equation B.35:

$$\frac{\eta}{G_0}\frac{d^2\tau_0}{dx^2} = c\tau_0 - \frac{6\left(1-\gamma_1^2\right)}{E_1 t_1^2}V_1 - \frac{6\left(1-\gamma_2^2\right)}{E_2 t_2^2}V_2 \tag{B.37}$$

Differentiate

$$\frac{\eta}{G_0}\frac{d^3\tau_0}{dx^3} = c\frac{d\tau_0}{dx} - \frac{6\left(1-\gamma_1^2\right)}{E_1 t_1^2}\frac{dV_1}{dx} - \frac{6\left(1-\gamma_2^2\right)}{E_2 t_2^2}\frac{dV_2}{dx} \tag{B.38}$$

Rewrite

$$\frac{\eta}{G_0}\frac{d^3\tau_0}{dx^3} - c\frac{d\tau_0}{dx} = -\frac{6\left(1-\gamma_1^2\right)}{E_1 t_1^2}\frac{dV_1}{dx} - \frac{6\left(1-\gamma_2^2\right)}{E_2 t_2^2}\frac{dV_2}{dx} \tag{B.39}$$

Rewrite equations B.15 and B.16.

$$\frac{dV_1}{dx} = \sigma_0 \tag{B.40}$$

$$\frac{dV_2}{dx} = -\sigma_0 \tag{B.41}$$

Implement equations B.40 and B.41 in equation B.39.

$$\frac{\eta}{G_0}\frac{d^3\tau_0}{dx^3} - c\frac{d\tau_0}{dx} = -\frac{6\left(1-\gamma_1^2\right)}{E_1 t_1^2}\sigma_0 + \frac{6\left(1-\gamma_2^2\right)}{E_2 t_2^2}\sigma_0 \tag{B.42}$$

Rewrite

$$\frac{\eta}{G_0}\frac{d^3\tau_0}{dx^3} - c\frac{d\tau_0}{dx} = \left[-\frac{6\left(1-\gamma_1^2\right)}{E_1 t_1^2} + \frac{6\left(1-\gamma_2^2\right)}{E_2 t_2^2}\right]\sigma_0 \tag{B.43}$$

Define constant a:

$$a = 6\left[\frac{\left(1-\gamma_1^2\right)}{E_1 t_1^2} - \frac{\left(1-\gamma_2^2\right)}{E_2 t_2^2}\right] \tag{B.44}$$

Implement constant a in equation B.43:

$$\frac{\eta}{G_0}\frac{d^3\tau_0}{dx^3} - c\frac{d\tau_0}{dx} = -a\sigma_0 \tag{B.45}$$

Rewrite

$$\frac{d^3\tau_0}{dx^3} = \frac{G_0 c}{\eta}\frac{d\tau_0}{dx} - \frac{G_0 a}{\eta}\sigma_0 \tag{B.46}$$

Normal stress analysis

Rewriting equation B.23

$$\frac{\eta}{E_0}\sigma_0 = v_1 - v_2 \tag{B.47}$$

Differentiate

$$\frac{\eta}{E_0}\frac{d\sigma_0}{dx} = \frac{dv_1}{dx} - \frac{dv_2}{dx} \tag{B.48}$$

Differentiate

$$\frac{\eta}{E_0}\frac{d^2\sigma_0}{dx^2} = \frac{d^2v_1}{dx^2} - \frac{d^2v_2}{dx^2} \tag{B.49}$$

Implement equations B.19 and B.20 in equation B.49

$$\frac{\eta}{E_0}\frac{d^2\sigma_0}{dx^2} = -\frac{M_1}{D_1} + \frac{M_2}{D_2} \tag{B.50}$$

Implement equation B.21 in equation B.50

$$\frac{\eta}{E_0}\frac{d^2\sigma_0}{dx^2} = -\frac{12\left(1-\gamma_1^2\right)}{E_1 t_1^3}M_1 + \frac{12\left(1-\gamma_2^2\right)}{E_2 t_2^3}M_2 \tag{B.51}$$

Differentiate

$$\frac{\eta}{E_0}\frac{d^3\sigma_0}{dx^3} = -\frac{12\left(1-\gamma_1^2\right)}{E_1 t_1^3}\frac{dM_1}{dx} + \frac{12\left(1-\gamma_2^2\right)}{E_2 t_2^3}\frac{dM_2}{dx} \tag{B.52}$$

Implement equations B.32 and B.33 in equation B.52

$$\frac{\eta}{E_0}\frac{d^3\sigma_0}{dx^3} = -\frac{12\left(1-\gamma_1^2\right)}{E_1 t_1^3}\left[V_1 - \tau_0\frac{t_1}{2}\right] + \frac{12\left(1-\gamma_2^2\right)}{E_2 t_2^3}\left[V_2 - \tau_0\frac{t_2}{2}\right] \tag{B.53}$$

Rewrite

$$\frac{\eta}{E_0}\frac{d^3\sigma_0}{dx^3} = 6\left[\frac{\left(1-\gamma_1^2\right)}{E_1 t_1^2} - \frac{\left(1-\gamma_2^2\right)}{E_2 t_2^2}\right]\tau_0 - \frac{12\left(1-\gamma_1^2\right)}{E_1 t_1^3}V_1 + \frac{12\left(1-\gamma_2^2\right)}{E_2 t_2^3}V_2 \tag{B.54}$$

Implement constant a (equation B.44) in equation B.54

$$\frac{\eta}{E_0}\frac{d^3\sigma_0}{dx^3} = a\tau_0 - \frac{12\left(1-\gamma_1^2\right)}{E_1 t_1^3}V_1 + \frac{12\left(1-\gamma_2^2\right)}{E_2 t_2^3}V_2 \tag{B.55}$$

Differentiate

$$\frac{\eta}{E_0}\frac{d^4\sigma_0}{dx^4} = a\frac{d\tau_0}{dx} - \frac{12\left(1-\gamma_1^2\right)}{E_1 t_1^3}\frac{dV_1}{dx} + \frac{12\left(1-\gamma_2^2\right)}{E_2 t_2^3}\frac{dV_2}{dx} \tag{B.56}$$

Implement equations B.40 and B.41 in equation B.56

$$\frac{\eta}{E_0}\frac{d^4\sigma_0}{dx^4} = a\frac{d\tau_0}{dx} - \frac{12\left(1-\gamma_1^2\right)}{E_1 t_1^3}\sigma_0 - \frac{12\left(1-\gamma_2^2\right)}{E_2 t_2^3}\sigma_0 \tag{B.57}$$

Rewrite

$$\frac{\eta}{E_0}\frac{d^4\sigma_0}{dx^4} = a\frac{d\tau_0}{dx} - 12\left[\frac{\left(1-\gamma_1^2\right)}{E_1 t_1^3} + \frac{\left(1-\gamma_2^2\right)}{E_2 t_2^3}\right]\sigma_0 \tag{B.58}$$

Define constant b

$$b = 12\left[\frac{\left(1-\gamma_1^2\right)}{E_1 t_1^3} + \frac{\left(1-\gamma_2^2\right)}{E_2 t_2^3}\right] \tag{B.59}$$

Implement constant b in equation B.58

$$\frac{\eta}{E_0}\frac{d^4\sigma_0}{dx^4} + b\sigma_0 = a\frac{d\tau_0}{dx} \tag{B.60}$$

Differentiate

$$\frac{\eta}{E_0}\frac{d^5\sigma_0}{dx^5} + b\frac{d\sigma_0}{dx} = a\frac{d^2\tau_0}{dx^2} \tag{B.61}$$

Differentiate

$$\frac{\eta}{E_0}\frac{d^6\sigma_0}{dx^6} + b\frac{d^2\sigma_0}{dx^2} = a\frac{d^3\tau_0}{dx^3} \tag{B.62}$$

Implement equation B.46 in equation B.62

$$\frac{\eta}{E_0}\frac{d^6\sigma_0}{dx^6}+b\frac{d^2\sigma_0}{dx^2}=a\left[\frac{G_0c}{\eta}\frac{d\tau_0}{dx}-\frac{G_0a}{\eta}\sigma_0\right] \tag{B.63}$$

Rewrite

$$\frac{\eta}{E_0}\frac{d^6\sigma_0}{dx^6}+b\frac{d^2\sigma_0}{dx^2}+\frac{G_0a^2}{\eta}\sigma_0=\frac{G_0c}{\eta}a\frac{d\tau_0}{dx} \tag{B.64}$$

Implement equation B.60 in equation B.65

$$\frac{\eta}{E_0}\frac{d^6\sigma_0}{dx^6}+b\frac{d^2\sigma_0}{dx^2}+\frac{G_0a^2}{\eta}\sigma_0=\frac{G_0c}{\eta}\left[\frac{\eta}{E_0}\frac{d^4\sigma_0}{dx^4}+b\sigma_0\right] \tag{B.65}$$

Rewrite

$$\frac{\eta}{E_0}\frac{d^6\sigma_0}{dx^6}-\frac{G_0c}{E_0}\frac{d^4\sigma_0}{dx^4}+b\frac{d^2\sigma_0}{dx^2}+\frac{G_0(a^2-bc)}{\eta}\sigma_0=0 \tag{B.66}$$

Rewrite

$$\frac{d^6\sigma_0}{dx^6}-\frac{G_0c}{\eta}\frac{d^4\sigma_0}{dx^4}+\frac{E_0b}{\eta}\frac{d^2\sigma_0}{dx^2}-\frac{G_0E_0(bc-a^2)}{\eta^2}\sigma_0=0 \tag{B.67}$$

With:

$$a=6\left[\frac{\left(1-\gamma_1^2\right)}{E_1t_1^2}-\frac{\left(1-\gamma_2^2\right)}{E_2t_2^2}\right] \tag{B.68}$$

$$b=12\left[\frac{\left(1-\gamma_1^2\right)}{E_1t_1^3}+\frac{\left(1-\gamma_2^2\right)}{E_2t_2^3}\right] \tag{B.69}$$

$$c=4\left[\frac{\left(1-\gamma_1^2\right)}{E_1t_1}+\frac{\left(1-\gamma_2^2\right)}{E_2t_2}\right] \tag{B.70}$$

This sixth-order differential equation matches the differential equation given [3]. This differential equation has roots of $+\beta_1$, $-\beta_1$, $\beta_H+i\beta_V$, $\beta_H-i\beta_V$, $-\beta_H+i\beta_V$ and $-\beta_H-i\beta_V$. The general solution for the normal stress is then given by:

$$\begin{aligned}\sigma_0 = {} & A_1cosh\left(\beta_1x\right)+A_2sinh\left(\beta_1x\right)+A_3cosh\left(\beta_Hx\right)cos\left(\beta_Vx\right)\\ & +A_4sinh\left(\beta_Hx\right)cos\left(\beta_Vx\right)+A_5sinh\left(\beta_Hx\right)sin\left(\beta_Vx\right)+A_6cosh\left(\beta_Hx\right)sin\left(\beta_Vx\right)\end{aligned} \tag{B.71}$$

Due to symmetry around the plane x=0, this equation can be reduced to:

$$\sigma_0=A_1cosh\left(\beta_1x\right)+A_3cosh\left(\beta_Hx\right)cos\left(\beta_Vx\right)+A_5sinh\left(\beta_Hx\right)sin\left(\beta_Vx\right) \tag{B.72}$$

The three constants A_1, A_2 and A_3 are determined from the following equations:

$$\begin{aligned}&\beta_1^2cosh\left(\beta_1l\right)A_1+\left[\left(\beta_H^2-\beta_V^2\right)cosh\left(\beta_Hl\right)cos\left(\beta_Vl\right)-2\beta_H\beta_Vsinh\left(\beta_Hl\right)sin\left(\beta_Vl\right)\right]A_3\\ &+\left[\left(\beta_H^2-\beta_V^2\right)sinh\left(\beta_Hl\right)sin\left(\beta_Vl\right)+2\beta_H\beta_Vcosh\left(\beta_Hl\right)cos\left(\beta_Vl\right)\right]A_5=0\end{aligned} \tag{B.73}$$

$$\frac{sinh(\beta_1 l)}{\beta_1} A_1 + \left[\frac{\beta_V}{(\beta_H^2 + \beta_V^2)} cosh(\beta_H l) sin(\beta_V l) + \frac{\beta_H}{(\beta_H^2 + \beta_V^2)} sinh(\beta_H l) cos(\beta_V l) \right] A_3 + \left[\frac{\beta_H}{(\beta_H^2 + \beta_V^2)} cosh(\beta_H l) sin(\beta_V l) - \frac{\beta_V}{(\beta_H^2 + \beta_V^2)} sinh(\beta_H l) cos(\beta_V l) \right] A_5 = 0 \quad \text{(B.74)}$$

$$\left[\left(\beta_1^4 + \frac{E_0 b}{\eta} \right) cosh(\beta_1 l) \right] A_1 + \left[(\beta_H^2 - \beta_V^2) - 4\beta_H^2 \beta_V^2 + \frac{E_0 b}{\eta} \right] cosh(\beta_H l) cos(\beta_V l) - 4\beta_H \beta_V (\beta_H^2 - \beta_V^2) sinh(\beta_H l) sin(\beta_V l) A_3 + \left[(\beta_H^2 - \beta_V^2)^2 - 4\beta_H^2 \beta_V^2 + \frac{E_0 b}{\eta} \right] sinh(\beta_H l) sin(\beta_V l) + 4\beta_H \beta_V (\beta_H^2 - \beta_V^2) cosh(\beta_H l) cos(\beta_V l) A_5 = \left(\frac{E_0 b}{\eta} \right) \left(\frac{G_0 c}{\eta} \right) \left(\frac{9}{bc} \right) [(1+\gamma_1)\alpha_1 - (1+\gamma_2)\alpha_2] T \quad \text{(B.75)}$$

The shear stress is given by:

$$\tau_0 = C_1 sinh(\beta_1 x) + C_2 sinh(\beta_H x) cos(\beta_V x) + C_3 cosh(\beta_H x) sin(\beta_V x) \quad \text{(B.76)}$$

The three constants C_1, C_2 and C_3 are determined from the following equations:

$$C_1 = \frac{1}{\beta_1} \left(\frac{\eta}{E_0 b} \right) \left(\frac{b}{a} \right) \left(\beta_1^4 + \frac{E_0 b}{\eta} \right) A_1 \quad \text{(B.77)}$$

$$C_2 = \left(\frac{\eta}{E_0 b} \right) \left(\frac{b}{a} \right) [\gamma_1 A_3 - \gamma_2 A_5] \quad \text{(B.78)}$$

$$C_3 = \left(\frac{\eta}{E_0 b} \right) \left(\frac{b}{a} \right) [\gamma_1 A_5 + \gamma_2 A_3] \quad \text{(B.79)}$$

With:

$$\gamma_1 = \beta_H \left[\frac{E_0 b}{\eta (\beta_H^2 + \beta_V^2)} + \beta_H^2 - 3\beta_V^2 \right] \quad \text{(B.80)}$$

$$\gamma_2 = \beta_V \left[\frac{E_0 b}{\eta (\beta_H^2 + \beta_V^2)} + \beta_V^2 - 3\beta_H^2 \right] \quad \text{(B.81)}$$

B.4. CHEN MATLAB CODE

```
clear all
close all
clc

%% Input
count = 0;
for i = [1.5e-3 3e-3 5e-3]
count = count + 1;

% Solder
w = 150e-3; %[m]
l = w/2; %[m]
x = [0:1e-3:l]; %[m]
```

E0 = 32e3; %[MPa]
G0 = 12e3; %[MPa]
eta = 75e-6; %[m]

% Material 1 (SF-Cu)
E1 = 118e3; %[MPa]
t1 = 2e-3; %[m]
alpha1 = 17.6e-6; %[-]
gamma1 = 0.34; %[-]
I1 = (t1^3)/12;

% Material 2 (Al-6082)
E2 = 70e3; %[MPa]
t2 = i; %[m]
alpha2 = 24e-6; %[-]
gamma2 = 0.33; %[-]
I2 = (t2^3)/12;

% Temperature
T = (183-25); %[degC]

%% Bending Calculations
% Constants abc
Bending.a = 6 * ((1-gamma1^2)/($E1 * t1^2$) − (1 − $gamma2^2$)/($E2 * t2^2$));
$Bending.b = 12 * ((1 - gamma1^2)/(E1 * t1^3) + (1 - gamma2^2)/(E2 * t2^3))$;
$Bending.c = 4 * ((1 - gamma1^2)/(E1 * t1) + (1 - gamma2^2)/(E2 * t2))$;

% Constants ABCD
A = 1;
B = - G0*Bending.c/eta;
C = E0*Bending.b/eta;
D = - G0*E0*(Bending.b*Bending.c-Bending.a^2)/(eta^2);
%$beta$
$R = roots([A0 B0 C0 D])$
%$R = round(R,10)$
$im = imag(R)$;

B1 = find(im==0);
B1real = R([B1]);
beta1 = max(B1real)

BHim = max(im);
BH = find(im==BHim);
BHreal = real(R([BH]));
betaH = abs(max(BHreal))

betaV = max(im)
clear A B C D %im B1 B1real BHim BH BHreal R

% Constans A1 A3 A5
% System of equations AX=B, where X=[A1 A3 A5]: X=A/B
A11 = (beta1^2) $* cosh(beta1 * l)$;
$A12 = (((betaH^2) - (betaV^2)) * cosh(betaH * l) * cos(betaV * l) - 2 * betaH * betaV * sinh(betaH * l) * sin(betaV * l))$;
$A13 = (((betaH^2) - (betaV^2)) * sinh(betaH * l) * sin(betaV * l) + 2 * betaH * betaV * cosh(betaH * l) * cos(betaV * l))$;
$A21 = (sinh(beta1 * l)/beta1)$;

$A22 = ((betaV/((betaH^2)+(betaV^2)))*cosh(betaH*l)*sin(betaV*l)+(betaH/((betaH^2)+(betaV^2)))*sinh(betaH*l)*cos(betaV*l));$
$A23 = ((betaH/((betaH^2)+(betaV^2)))*cosh(betaH*l)*sin(betaV*l)-(betaV/((betaH^2)+(betaV^2)))*sinh(betaH*l)*cos(betaV*l));$
$A31 = (((beta1^4)+(E0*Bending.b/eta))*cosh(beta1*l));$
$A32 = ((((betaH^2)-(betaV^2))-4*(betaH^2)*(betaV^2)+(E0*Bending.b/eta))*cosh(betaH*l)*cos(betaV*l)-4*betaH*betaV*((betaH^2)-(betaV^2))*sinh(betaH*l)*sin(betaV*l));$
$A33 = ((((betaH^2)-(betaV^2))^2-4*(betaH^2)*(betaV^2)+(E0*Bending.b/eta))*sinh(betaH*l)*sin(betaV*l)+4*betaH*betaV*((betaH^2)-(betaV^2))*cosh(betaH*l)*cos(betaV*l));$
$A = [A11\,A12\,A13; A21\,A22\,A23; A31\,A32\,A33];$
$clear\,A11\,A12\,A13\,A21\,A22\,A23\,A31\,A32\,A33$
$B = [0;0;(E0*Bending.b/eta)*(G0*Bending.c/eta)*(9/(Bending.b*Bending.c))*((1+gamma1)*alpha1-(1+gamma2)*alpha2)*T];$
$X = mldivide(A,B);$
$Bending.A1 = X(1);$
$Bending.A3 = X(2);$
$Bending.A5 = X(3);$
$clear\,A\,B\,X$

% Constans y1 y2
y1 = betaH * ((E0*Bending.b)/(eta*((betaH^2) + ($betaV^2$))) + ($betaH^2$) − 3 * ($betaV^2$));
$y2 = betaV*((E0*Bending.b)/(eta*((betaH^2)+(betaV^2)))+(betaV^2)-3*(betaH^2));$
$\%Constants\,C1\,C2\,C3$
$Bending.C1 = (1/beta1)*(eta/(E0*Bending.b))*(Bending.b/Bending.a)*(beta1^4+(E0*Bending.b)/eta)*Bending.A1;$
$Bending.C2 = (eta/(E0*Bending.b))*(Bending.b/Bending.a)*(y1*Bending.A3-y2*Bending.A5);$
$Bending.C3 = (eta/(E0*Bending.b))*(Bending.b/Bending.a)*(y1*Bending.A5+y2*Bending.A3);$
$clear\,y1\,y2$

% Tensile stress
Bending.sigma0(count,:) = Bending.A1*cosh(beta1.*x) + Bending.A3*cosh(betaH.*x).*cos(betaV.*x) + Bending.A5*sinh(betaH.*x).*sin(betaV.*x);
% Shear stress
Bending.tau0(count,:) = Bending.C1*sinh(beta1.*x) + Bending.C2*sinh(betaH.*x).*cos(betaV.*x) + Bending.C3*cosh(betaH.*x).*sin(

% Structure
Bending.beta1 = beta1;
Bending.betaH = betaH;
Bending.betaV = betaV;
%clear beta1 betaH betaV y
end

B.5. NORMAL STRESS FEM RESULTS

Figures B.4 and B.5 show the normal stress for the cases of 1.5 *mm* aluminum soldered to 2 *mm* copper and 3 *mm* aluminum soldered to 2 *mm* copper. For the shear stress these cases caused difficulties for the analytical model, however these normal stress figures are similar to the FEM results.

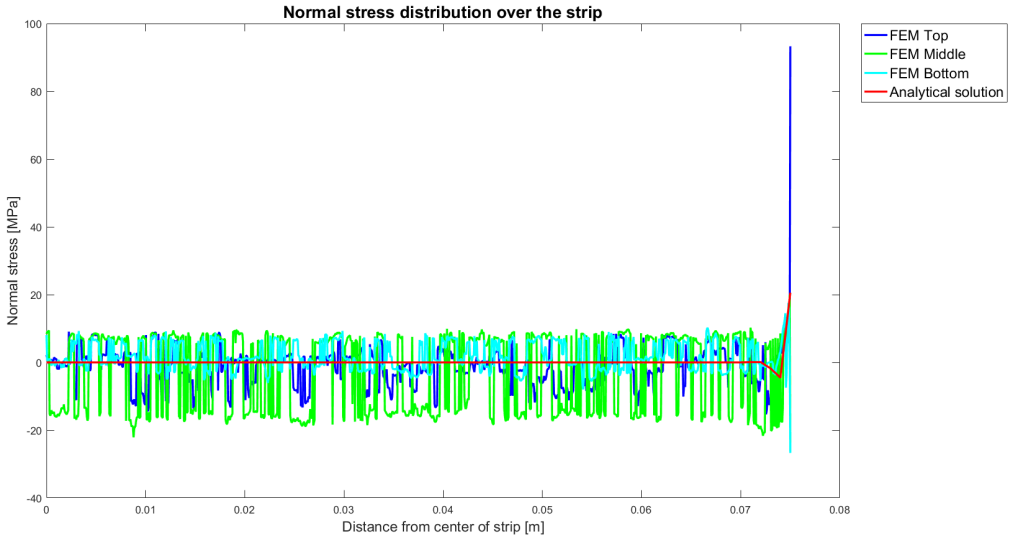

Figure B.4: Analytical and FEM results for the normal stress of the solder layer for an aluminum thickness of 1.5 mm, copper thickness of 2 mm and solder layer thickness of 75 μm.

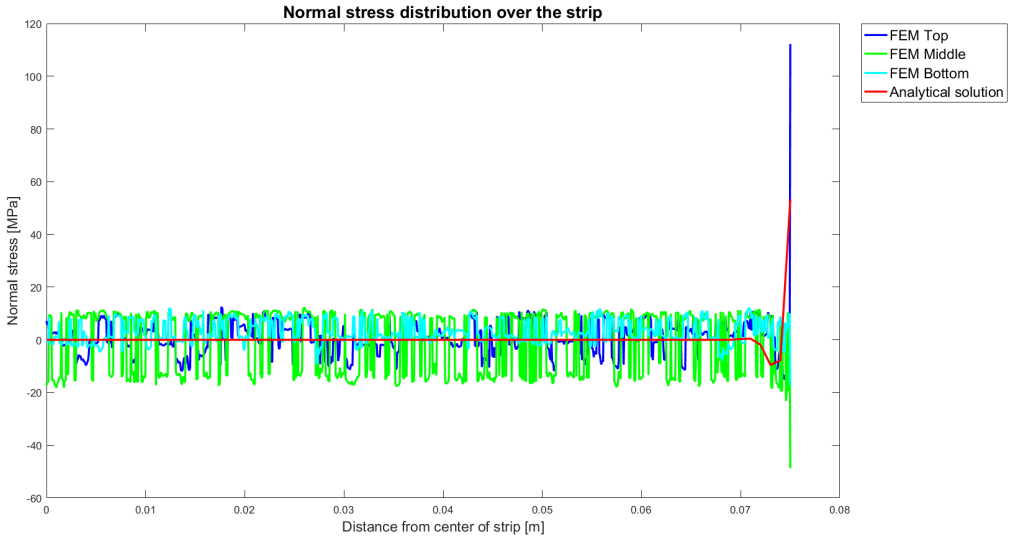

Figure B.5: Analytical and FEM results for the shear normal of the solder layer for an aluminum thickness of 3 mm, copper thickness of 2 mm and solder layer thickness of 75 μm.

C

THERMAL HEAT TRANSFER

C.1. LO BRACKET LAYOUT

In this section the layout of the bracket for the LO board is presented. The bracket is made of aluminum (Al 6061). Figures C.1 - C.4 show a 3D view, the top view, the side view and the bottom view. In the bottom view one can see the cutouts for the traces.

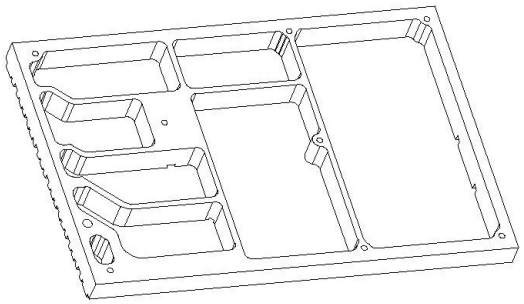

Figure C.1: The layout of the LO bracket.

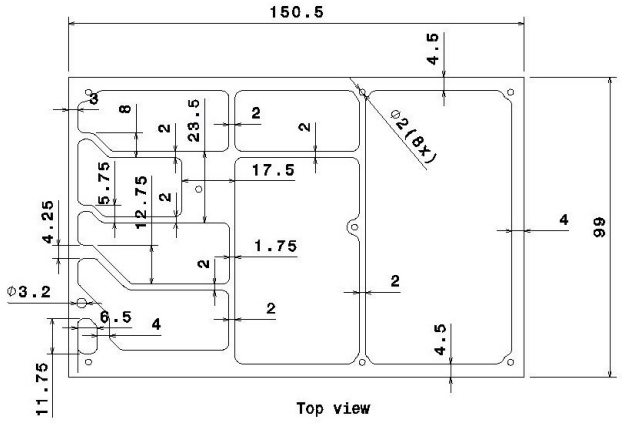

Figure C.2: The top view of the LO bracket.

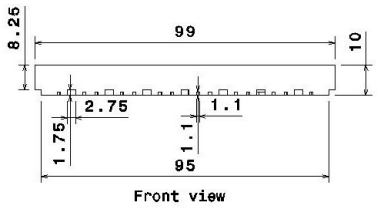

Figure C.3: The side view of the LO bracket.

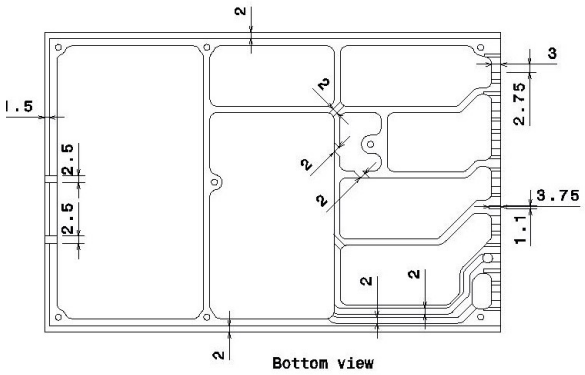

Figure C.4: The bottom view of the LO bracket.

C.2. THERMAL HEAT TRANSFER MODEL SPECIFICATIONS

The conduction, convection and radiation equations used in the thermal model of the LO board are presented in chapter 3. To model these heat transfer mechanisms, the board is divided into nodes. The location of these nodes is chosen to match with the heat sources, heat sink and the intersection of walls, this was shown in figure 3.3 of chapter 3.2. This section describes the details of the thermal model. The thermal model is built in LT Spice, which is normally used for electronic design. However, thermal relations can be transferred to electrical relations making LTSpice suitable for thermal analysis. The voltage can be replaced by temperature and the current by heat flow, to transform the electrical model into a thermal model. To give an impression, the entire model is shown in figure C.5. Because the entire model is to large to explain at once, details will be provided in sections C.2.1 - C.2.5. This model is the result of an iterative process between model building and thermal testing.

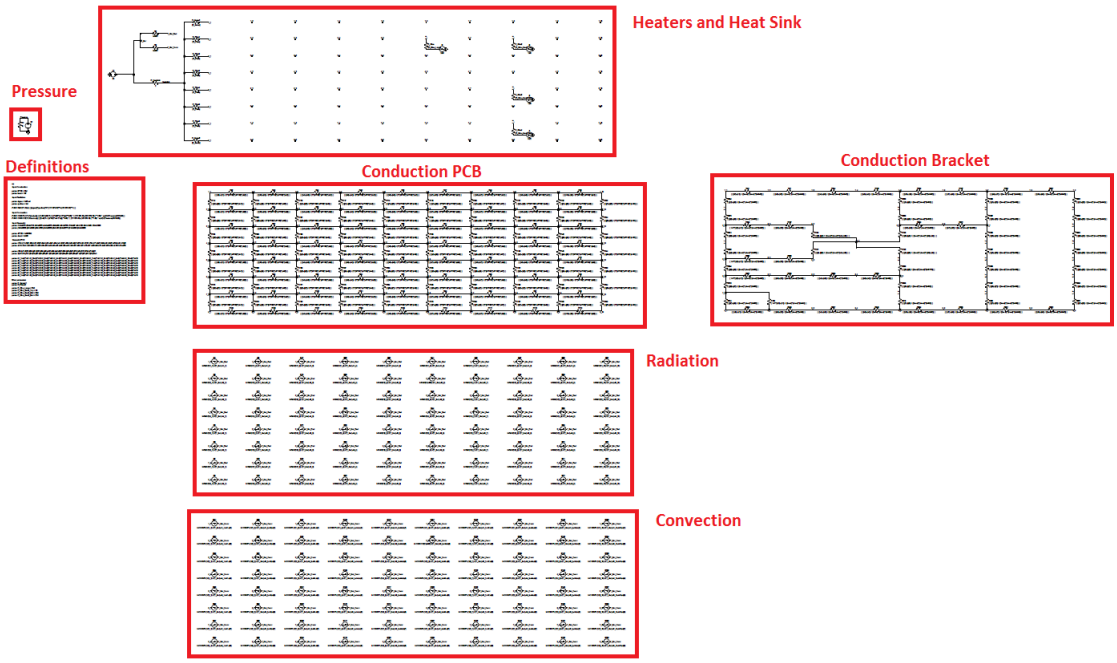

Figure C.5: Overview of the LTSpice model.

The figure indicates the sections which make up the entire model. The function and details of these sections will be shown below. First the definition of several parameters and functions are shown. This is followed by the heat transfer mechanisms; conduction, convection and radiation. The heaters and heat sink section combines all different aspects of the thermal model.

C.2.1. DEFINITIONS

HEAT TRANSFER MECHANISMS

The first set of definitions belong to the heat transfer mechanisms, and are shown in figure C.6. For the conduction equations the material properties of the PCB and the material need to be defined. The thermal conductivity for the PCB is 394 W/mK, which is the thermal conductivity of copper [5]. Here it is assumed that only the copper layers (without to many disruptions by the traces) will contribute to the conductivity of the PCB. The thermal conductivity of the aluminum is 167 W/mK [6].

```
Input Conduction
.param kPCB = 394
.param kmat = 167

Input Radiation
.param sigma = 5.67e-8
.param epsilon = 0.9
.FUNC RAD(V1,V2,A) { {sigma}*{epsilon}*A*( (V1+273.15)**4-(V2+273.15)**4 ) }

Input Convection
.FUNC CONVPL(V1,V2,A,dx,dy) { ((1.32+0.59)*A / ((4*A/(2*dx+2*dy))**0.25) * ( (V1+273.15)-(V2+273.15) )**1.25) * sqrt(V(Pressure)/1013.25) }
.FUNC CONVCO(V1,V2,A,dx,dy) { ((2.44)*A / ((4*A/(2*dx+2*dy))**0.25) * ( (V1+273.15)-(V2+273.15) )**1.25) * sqrt(V(Pressure)/1013.25)}
```

Figure C.6: LTSpice heat transfer mechanisms parameters.

For the radiation, the inputs are the Stefan-Boltman constant σ (5.67e-8 $W/m^2/K^4$) and the emisivity ϵ 0.9 of the PCB [39]. Next, equation C.1 is defined as function with as input parameters the voltages V1 and V2 and

area A. Keep in mind that LTSpice is an electronic design tool, thus that the voltages represent temperatures; V1 is T_{loc} and V2 is T_{amb}.

$$q = A\epsilon\sigma(T_{loc}^4 - T_{amb}^4) \tag{C.1}$$

The last heat transfer mechanism is the convection. For this, a function has been defined representing equations C.2 - C.6. A difference is made between the component and PCB convection because of the slightly different different definitions of the heat transfer coefficients. The input parameters for this function are the voltages V1 and V2 (which represent the local and ambient temperature), and distances dx and dy. These distances are used to determine the perimeter p of equation C.6. More details on the geometry of the PCB are presented in the section Geometry. Because convection (by air) is a air-pressure related phenomena, a pressure dependency is defined in the convection function. This dependency will be explained in the section Pressure.

$$q = h_{conv}A(T_{loc} - T_{amb}) \tag{C.2}$$

Table C.1: Convection heat transfer coefficients [9]

Geometry	$[W/m^2K]$
Horizontal Plate	
a) Hot surface facing up	$h_{conv} = 1.32\left(\frac{\Delta T}{L_c}\right)^{0.25}$ (C.3)
b) Hot surface facing down	$h_{conv} = 0.59\left(\frac{\Delta T}{L_c}\right)^{0.25}$ (C.4)
Components on a circuit board	$h_{conv} = 2.44\left(\frac{\Delta T}{L_c}\right)^{0.25}$ (C.5)

$$L_c = \frac{4A}{p} \tag{C.6}$$

PRESSURE

The loss of air-pressure affects the convection heat transfer. Less pressure means less air particles, thus less convection. This can mathematically be expressed by equation C.7, which gives the heat flow by convection at pressure p_x.

$$q_{conv_{px}} = \sqrt{\frac{p_x}{p_{atm}}}q_{conv} \tag{C.7}$$

With $q_{conv_{px}}$ the convection heat flow at pressure x, p_x the pressure x, p_{atm} the standard atmospheric pressure of 1013.25 mbar and q_{conv} the convection heat flow (given by equation 3.3). This equation is incorporated in the convection component of the LTSpice model. The pressure is modelled by a simple circuit separated from the heat transfer mechanisms. This circuit is shown in figure C.7, and allows the vary the pressure of the entire system by changing the voltage (pressure) at the source. The pressure in the figure is set to 20 $mbar$.

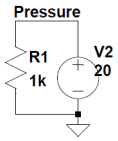

Figure C.7: LTSpice model of the pressure.

GEOMETRY

```
Input Geometry
.param x1=0.0015 x2=0.0115 x3=0.0375 x4=0.04575 x5=0.054 x6=0.0735 x7=0.097 x8=0.120 x9=0.1485 x10=0.1585
.param y1=0.09625 y2=0.0895 y3=0.0735 y4=0.06225 y5=0.052 y6=0.02775 y7=0.0095 y8=0.00225

.param dPCB = 0.000108
.param dmat = 0.005

Geometry PCB

.param x12=(x1+x2)/2 x23=(x2+x3)/2 x34=(x3+x4)/2 x45=(x4+x5)/2 x56=(x5+x6)/2 x67=(x6+x7)/2 x78=(x7+x8)/2 x89=(x8+x9)/2 x910=(x9+x10)/2
.param dx1=x12-0 dx2=x23-x12 dx3=x34-x23 dx4=x45-x34 dx5=x56-x45 dx6=x67-x56 dx7=x78-x67 dx8=x89-x78 dx9=x910-x89 dx10=0.16-x910

.param y12=(y1+y2)/2 y23=(y2+y3)/2 y34=(y3+y4)/2 y45=(y4+y5)/2 y56=(y5+y6)/2 y67=(y6+y7)/2 y78=(y7+y8)/2
.param dy1=0.10-y12 dy2=y12-y23 dy3=y23-y34 dy4=y34-y45 dy5=y45-y56 dy6=y56-y67 dy7=y67-y78 dy8=y78-0

.param A1_1=dy1*dx1 A1_2=dy1*dx2 A1_3=dy1*dx3 A1_4=dy1*dx4 A1_5=dy1*dx5 A1_6=dy1*dx6 A1_7=dy1*dx7 A1_8=dy1*dx8 A1_9=dy1*dx9 A1_10=dy1*dx10
.param A2_1=dy2*dx1 A2_2=dy2*dx2 A2_3=dy2*dx3 A2_4=dy2*dx4 A2_5=dy2*dx5 A2_6=dy2*dx6 A2_7=dy2*dx7 A2_8=dy2*dx8 A2_9=dy2*dx9 A2_10=dy2*dx10
.param A3_1=dy3*dx1 A3_2=dy3*dx2 A3_3=dy3*dx3 A3_4=dy3*dx4 A3_5=dy3*dx5 A3_6=dy3*dx6 A3_7=dy3*dx7 A3_8=dy3*dx8 A3_9=dy3*dx9 A3_10=dy3*dx10
.param A4_1=dy4*dx1 A4_2=dy4*dx2 A4_3=dy4*dx3 A4_4=dy4*dx4 A4_5=dy4*dx5 A4_6=dy4*dx6 A4_7=dy4*dx7 A4_8=dy4*dx8 A4_9=dy4*dx9 A4_10=dy4*dx10
.param A5_1=dy5*dx1 A5_2=dy5*dx2 A5_3=dy5*dx3 A5_4=dy5*dx4 A5_5=dy5*dx5 A5_6=dy5*dx6 A5_7=dy5*dx7 A5_8=dy5*dx8 A5_9=dy5*dx9 A5_10=dy5*dx10
.param A6_1=dy6*dx1 A6_2=dy6*dx2 A6_3=dy6*dx3 A6_4=dy6*dx4 A6_5=dy6*dx5 A6_6=dy6*dx6 A6_7=dy6*dx7 A6_8=dy6*dx8 A6_9=dy6*dx9 A6_10=dy6*dx10
.param A7_1=dy7*dx1 A7_2=dy7*dx2 A7_3=dy7*dx3 A7_4=dy7*dx4 A7_5=dy7*dx5 A7_6=dy7*dx6 A7_7=dy7*dx7 A7_8=dy7*dx8 A7_9=dy7*dx9 A7_10=dy7*dx10
.param A8_1=dy8*dx1 A8_2=dy8*dx2 A8_3=dy8*dx3 A8_4=dy8*dx4 A8_5=dy8*dx5 A8_6=dy8*dx6 A8_7=dy8*dx7 A8_8=dy8*dx8 A8_9=dy8*dx9 A8_10=dy8*dx10
```

Figure C.8: LTSpice geometry parameters.

Figure C.8 shows the geometry parameters used in the model. The entire PCB surface is divided over the different nodes. Because the nodes are not equally distributed over the LO board, this is shown in figure C.9, the area used in the heat transfer mechanisms equations will change per node. Figure C.10 illustrates the definitions for node 6_3. Note that the figure shows equally distributed nodes, which is not the case for the model.

sections.png

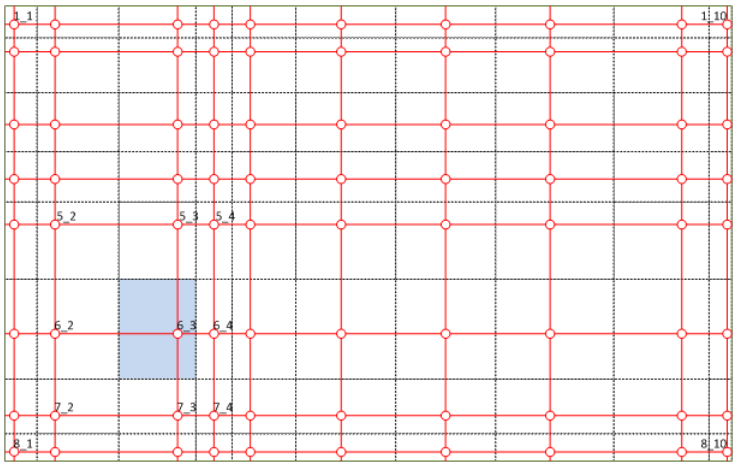

Figure C.9: Node distribution over the PCB.

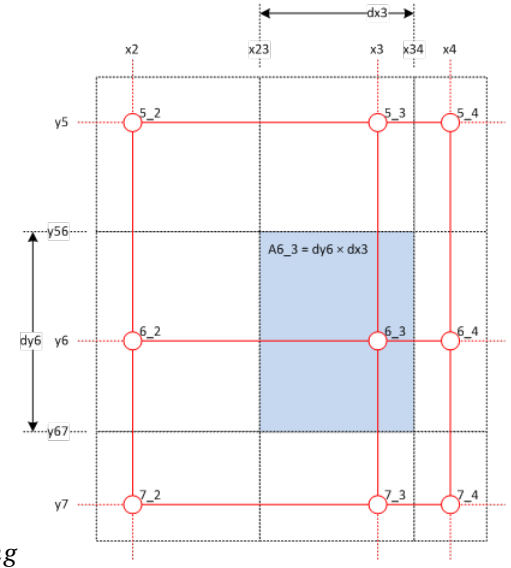

section $6_3.png$

Figure C.10: Area determination for each node.

The input for the geometry of the LO board are the node locations, and the thicknesses of the PCB and bracket material. The node locations were already presented in table C.2. It should be noted that the axis system start at the bottom left of the bracket, while the bracket nodes are outlined from the top left. This results that the nodes of the first row have the highest y-distance. The PCB thickness consists of the combined thickness of the conducting copper layers within the PCB, and is equal to 108 μm (6 plane layers of 18 μm each). The thickness of the bracket is 5 mm.

Table C.2: Locations of the nodes.

column/row number	1	2	3	4	5	6	7	8	9	10
x distance [mm]	1.5	11.5	37.5	45.75	54	73.5	97	120	148.5	158.5
y-distance [mm]	96.25	89.5	73.5	62.25	7 52.0	27.75	9.50	2.25		

OTHER PARAMETERS

The last part of the definition section in the model covers all the other parameters. These are related to the connection between the LO board and the heat sink, and the connection between the heaters and the PCB. These parameters are presented in figure C.11. The corners of the LO board will be screwed to the heatsink, optimization with the thermal test showed that the thermal resistance of the screw will be 3 K/W. For the thermal resistance of the contact surface between LO board with the heatsink this is determined to be 4 K/W.

```
Other parameters
.param R_Screw=3
.param R_Plate=4
.param R_Glue_Large = 22.5
.param R_Glue_Small_Top = 15
.param R_Glue_Small_Mid = 22.5
.param R_Glue_Small_Bot = 27.5
```

Figure C.11: LTSpice other parameters.

The heaters are glued with Stycast to the PCB. This glue will have a thermal resistance, which needs to be estimated. The thermal conductivity is Stycast is 1.25 W/mK [40], the length and area over which it conducts is estimated based on visual inspection of the glued heaters. These heaters were manually glued, thus the glue layers will not be identical resulting in different thermal resistances glue layer. The thermal resistance should be in the rough order of 22.5 K/W, but calculations show that small length and area variations can yield thermal resistance values between 15 - 30 K/W. The selected thermal resistance values give the best result when matched with the thermal test.

C.2.2. CONDUCTION

The conduction section of the model is made up by the conduction of the PCB and the conduction of the bracket. The thermal resistance between two points is given by equation C.8.

$$R = \frac{L}{kA} \tag{C.8}$$

This is modelled in LTSpice by placing a resistance between two nodes. As example, the conduction of the PCB and bracket are given for node 6_3 (the node on x = 37.5mm and y = 27.75 mm) in figures C.12 and C.13 (this node selected arbitrary for descriptive purposes). In this way, a network can be created covering all the nodes.

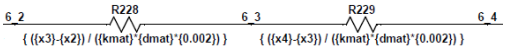

Figure C.12: LTSpice model of the bracket conduction of node 6_3.

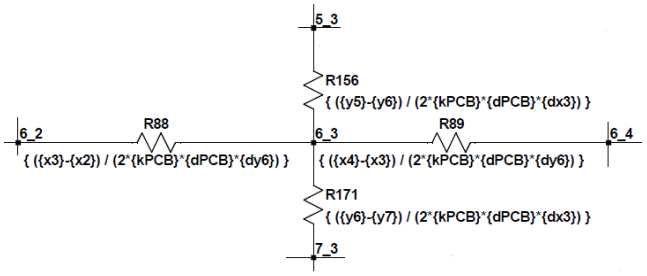

Figure C.13: LTSpice model of the PCB conduction of node 6_3.

One can see that the parameters defined in the section C.2.1 are used. For the conduction of the PCB a comment should be made; Equation C.8 shows the thermal resistance of a volume of material, in one direction. However, for the PCB the heat can flow in two directions (the z-directions is neglected). To compensate for this, only half of the volume is taken in each direction. The rationale is that when both directions are added, one ends up with the original volume and thus the thermal resistance of that volume. This compensation causes the factor 2 in the denominator of the PCB conduction.

C.2.3. CONVECTION

Convection is a heat flow, which can be modelled in LTSpice as a variable current source. The variable current source should be connected between the node and the ambient temperature. Figure C.14 shows the convection of node 6_3. One can see that the variable current source is attached to the node at one side, and the T_Sur_Conv at the other (details on this parameter are described below). The input for the function are the temperature of the node (V(6_3)), the ambient temperature (V(T_Sur)), and the convective areas and distances of that particular node. For nodes containing heaters, the heater temperature is taken as input instead

of the node temperature. This ensures that the heater is accounted for as a local hot spot in the convection calculations.

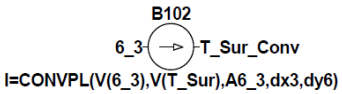

Figure C.14: LTSpice model of the convection of node 6_3.

C.2.4. RADIATION

Similar to the convection, the radiation components are modelled as variable current sources. These variable current sources should also be connected between the node and the ambient temperature. Figure C.15 shows the radiation of node 6_3. Also here one can see that the current source is connected to T_Sur_Rad, which is a parameter that will be explained in the next section. The inputs for this function are the local temperature (V(6_3)), the ambient temperature (V(T_Sur)), and the radiation area of that node. Again, the ensure that the heaters will be treated as local hot spots, the heater temperature will be taken at nodes with heaters attached.

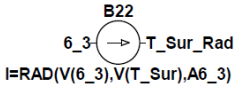

Figure C.15: LTSpice model of the convection of node 6_3.

C.2.5. HEATERS AND HEATSINK

The last section of the LTSpice model, heaters and heat sink, contains the input and output settings which bring all other section together. The input of the thermal analysis are the heaters, which can be modelled with a current source in LTSpice. The heaters are glued to the PCB, thus a thermal resistance is placed between the current source (heater) and node. Figure C.16 shows an example of the heater R4 attached to node 7_8 (x = 120 mm, y = 9.50 mm). The R4 heater dissipates 3.2 W, which is shown as current in the LTSpice model. For the other heaters, the same principle of current source and thermal resistance of the glue is applied.

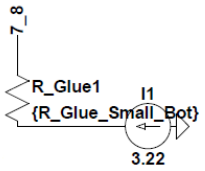

Figure C.16: LTSpice model of a heater.

The output settings defines how the ambient temperature is connected to the heat transfer mechanisms. The details of the LTSPice model are shown in figure C.17.

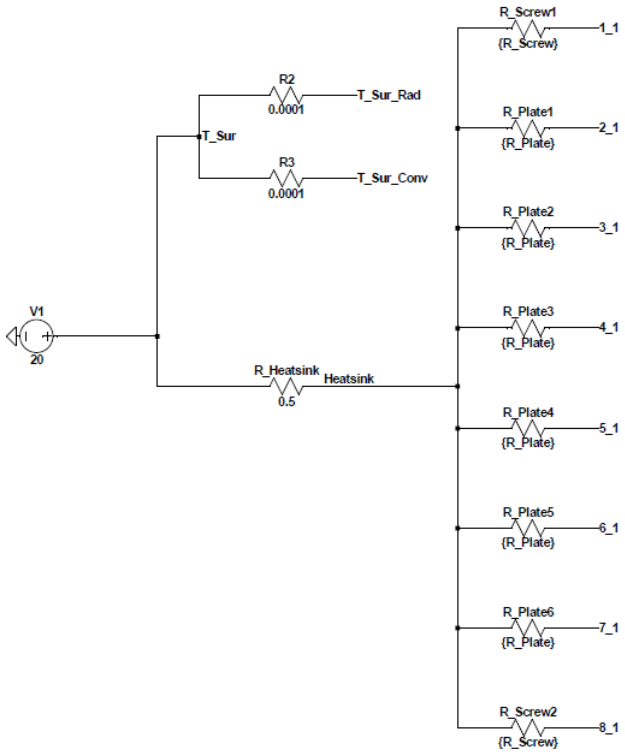

Figure C.17: LTSpice model of the heat sink.

On the right side of the figure, one can see the connection of the LO board to the heatsink. The corners are attached using screws, the rest of the side of the LO board just touches with the heat sink. This is modelled with thermal resistances, with the values for the screw and plate contacts defined in section C.2.1. The heatsink itself is connected to the ambient temperature, which is assumed to be constant at a temperature of 20 $^{\circ}C$. This is modelled in LTSpice with a constant voltage source shown at the left of the figure. The heatsink is modelled as a thermal resistance, however the heat sink itself will have radiation and convection components as well. In this model these are neglected, not because they do not exists, but because the interest of this model lies in the thermal behaviour of the LO board. By assuming that the heatsink has a low thermal resistance with its environment, one can easily reduce the complexity of the model without decreasing its performance.

As explained in sections C.2.3 and C.2.4, the heat generated by each node due to convection and radiation is stored in T_Sur_Conv and T_Sur_Rad respectively. These heat flows are connected to the ambient temperature through extremely low thermal resistances. These resistances are so low that they do not influence the temperature, but they are used to determine the total heat flow generated by convection and radiation. This is done by measuring the current (which represents the heat flow) through these resistances.

Measuring these heat flows, creates insight into the performance of the system. Because this is a closed system, the heat flows generated by conduction, convection and radiation should add up to the total dissipated power by the heaters. It also allows to see how much heat is conducted, which gives an indication on the effectiveness of the bracket as means for passive thermal control.

Table C.3: Total power radiated, convected and conducted at 1013 and 20 $mbar$.

	1013 $mbar$	20 $mbar$
Radiation [W]	1.75	2.55
Convection [W]	3.6	0.76
Conduction [W]	4.4	6.44

C.3. LO BOARD TEST RESULTS

This section shows all the thermocouple measurements, from the test described in chapter 3.5, are shown in tables C.4 and C.5. Both tables show that the model can predict the temperatures, with an uncertainty of around $\pm 3^{\circ}C$. The larger errors occur at the heaters, and can be contributed to the unknown thermal resistance of the glue. The only larger

Table C.4: Temperatures of the thermocouples at 1013 $mbar$.

Location	Model Temperature [$^{\circ}C$]	Measured Temperature [$^{\circ}C$]	Error [$^{\circ}C$]
S1	22.2	21.5	0.7
S2	24.5	25.2	-0.7
S3	24.2	25.1	-1.1
S4	24.6	24.5	0.1
S5	31.2	30.5	0.7
S6	41.3	42.8	-1.5
S7	104.1	110.6	-6.5
S8	79.4	73.6	5.8
S9	94.9	90.1	4.8
S10	48.2	46.1	2.1
S11	141.9	138.5	3.4
S12	46.2	43.9	2.4
S13	47.1	46.3	0.8
S14	45.7	42.2	3.5
S15	45.8	41.3	4.5
S16	46.5	44.8	1.7

Table C.5: Temperatures of the thermocouples at 20 $mbar$.

Location	Model Temperature [$^\circ C$]	Measured Temperature [$^\circ C$]	Error [$^\circ C$]
S1	23.5	23.8	-0.3
S2	27.0	29.7	-2.7
S3	26.7	29.9	-3.2
S4	27.3	28.9	-1.6
S5	37.9	37.5	0.4
S6	51.1	52.2	-1.1
S7	114.3	120.2	-5.9
S8	92.5	85.9	6.6
S9	108.5	102.9	5.6
S10	61.5	58.9	2.6
S11	154.8	153.2	1.6
S12	60.0	56.1	3.9
S13	60.7	59.4	1.3
S14	59.9	54.6	5.4
S15	60.3	54.3	6.0
S16	60.5	57.7	2.8

D

TRADE-OFF SENSITIVITY ANALYSIS

D.1. PCB CHARACTERISTICS

The PCB is a laminate, consisting of copper laminated into non-conductive substrates. The CTE and E-modulus of the PCB are not specified, and need to be determined. This is done in two ways, via literature and via testing.

CALCULATED PROPERTIES

According to Decolon [41] the E-modulus and CTE can be determined using equations D.1 and D.2.

$$E = V_f E_f + V_M E_M \tag{D.1}$$

$$\alpha = \frac{V_f E_f \alpha_f + V_M E_M \alpha_M}{V_f E_f + V_M E_M} \tag{D.2}$$

The PCB is built out of layers of copper and layers of FR-4. In this PCB, there are 8 layers of copper; 2 layers of 36 μm and 6 layers of 18 μm. The FR-4 consists of a total of 7 layers; 2 of 190 μm , 2 of 240 μm and 3 of 200 μm. The material properties of copper, FR-4 and the calculated PCB properties are given in table

Table D.1: The calculated PCB properties

	Copper	FR-4	PCB
Thickness [mm]	0.18	1.46	1.64
E-modulus [GPa]	118	23	33.4
CTE [$1/K$]	1.68E-05	1.20E-05	1.39E-05

TESTING

Strips of PCB and aluminum are soldered together, and were deflected due to the CTE mismatch. Using the deflection model presented in chapter 2, and the known material properties of aluminum, the PCB properties can be reverse engineered. This yielded an E-modulus of 25 GPa and a CTE of 16E-6 $1/K$.

Table D.2

Al [mm]	PCB [mm]	Deflection [mm]
1.5	1.6	2.05
5	1.6	0.45

D.2. SENSITIVITY OF MATERIAL PROPERTIES

In this section, the sensitivity analysis of the material properties is shown. The baseline design has a height of 5 mm and uses the calculated PCB properties (E modulus of 33.4 [GPa] and CTE of 1.39E-05 [$1/K$]). In this sensitivity analysis the results of changing the bracket height to 10 mm and, the results of changing the PCB properties to the reverse engineered values (E modulus of 25 [GPa] and CTE of 16E-06 [$1/K$]).

D.2.1. BRACKET HEIGHT OF 10mm

The first sensitivity analysis is performed for a bracket height of 10 mm.

CTE DEFLECTION

Table D.3: CTE Deflection for a height of 10 mm

Material	du [mm]	Score
Cu	0.04	10
Al	0.21	10
Ti	0.14	10
Mg	0.32	9
Mo	0.05	10
Kovar	0.12	10
Cu-Diamond	0.07	10
Al-Si	0.01	10
Al-SiC	0.00	10
Al-Graphite	0.12	10

SOLDER LAYER STRESS

Table D.4: Solder layer stress for a height of 10 mm

Material	Normal [Mpa]	Score	Shear [MPa]	Score	Combined Score
Cu	5.30	8	3.43	9	8.5
Al	17.81	4	11.99	4	4
Ti	16.92	4	11.03	5	4.5
Mg	19.87	3	14.01	3	3
Mo	22.46	2	14.03	3	2.5
Kovar	23.00	2	14.78	3	2.5
Cu-Diamond	15.82	4	9.97	5	4.5
Al-Si	1.34	10	0.87	10	10
Al-SiC	0.19	10	0.12	10	10
Al-Graphite	14.59	5	9.63	5	5

COMPONENT TEMPERATURE

Table D.5: The component temperature for a height of 10 mm

Material	T [$^{\circ}C$]	Score
Cu	144.4	9
Al	153.4	7
Ti	178.7	1
Mg	164.1	4
Mo	156.9	6
Kovar	178.6	1
Cu-Diamond	143.7	10
Al-Si	156	7
Al-SiC	153.9	7
Al-Graphite	151.3	8

TRADE-OFF

Table D.6: The resulting trade off for a height of 10 mm

h=10mm Material	Score	Density 0.54	CTE Stress 0.3	T_comp 0.16	Total
Cu		2	8.5	9	5.1
Al		9	4	7	7.2
Ti		7	4.5	1	5.3
Mg		9	3	4	6.4
Mo		1	2.5	6	2.3
Kovar		2	2.5	1	2.0
Cu-Diamond		4	4.5	10	5.1
Al-Si		8	10	7	8.4
Al-SiC		8	10	7	8.4
Al-Graphite		8	5	8	7.1

D.2.2. PCB REVERSE ENGINEERING

The second material properties sensitivity analysis is performed for the reverse engineered PCB properties (E modulus of 25 [GPa] and CTE of 16E-06 [$1/K$]).

CTE DEFLECTION

Table D.7: CTE deflections for the reverse engineered PCB properties

Material	du [mm]	Score
Cu	0.03	10
Al	0.46	9
Ti	0.48	9
Mg	0.68	8
Mo	0.20	10
Kovar	0.42	9
Cu-Diamond	0.26	9
Al-Si	0.11	10
Al-SiC	0.07	10
Al-Graphite	0.44	9

SOLDER LAYER STRESS

Table D.8: The solder layer stresses for the reverse engineered PCB properties

Material	Normal	Score	Shear	Score	Combined Score
Cu	0.95	10	0.62	10	10
Al	9.38	7	6.69	7	7
Ti	14.97	5	10.01	5	5
Mg	9.80	7	7.61	6	6.5
Mo	15.47	5	9.49	5	5
Kovar	15.65	4	10.18	5	4.5
Cu-Diamond	16.01	4	10.02	5	4.5
Al-Si	3.38	9	2.28	9	9
Al-SiC	2.44	10	1.62	10	10
Al-Graphite	11.41	6	7.82	6	6

TRADE-OFF

Table D.9: The trade-off for the reverse engineered material properties

Reverse	Score	Density	CTE Stress	T_comp	Total
Material		0.54	0.3	0.16	
Cu		2	10	8	5.4
Al		9	7	5	7.8
Ti		7	5	1	5.4
Mg		9	6.5	2	7.1
Mo		1	5	4	2.7
Kovar		2	4.5	1	2.6
Cu-Diamond		4	4.5	8	4.8
Al-Si		8	9	4	7.7
Al-SiC		8	10	5	8.1
Al-Graphite		8	6	6	7.1

D.3. SENSITIVITY ANALYSIS OF MATERIAL PROPERTIES AHP

In this section a sensitivity analysis on the pairwise comparison matrix for the material trade-off is performed. Three cases are considered; the first with more emphasis on density, the second with more emphasis on solder stress and the third with more emphasis on the component temperature.

D.3.1. EMPHASIS ON DENSITY

Table D.10: Pairwise comparison of the criteria.

	Density	Solder Stress	Temperature
Density	1	3	5
Solder Stress	1/3	1	2
Temperature	1/5	1/2	1

$$w = \begin{bmatrix} 0.65 \\ 0.23 \\ 0.12 \end{bmatrix} \tag{D.3}$$

λ_{max} = 3.0037
CI = 0.0018
CR = 0.3552 %

Table D.11: Trade-off table

h=5mm Material	Score	Density 0.65	Solder Stress 0.23	Temperature 0.12	Total
Cu		2	9	8	4.3
Al		9	4	5	7.4
Ti		7	4	1	5.6
Mg		9	3.5	2	6.9
Mo		1	3.5	4	1.9
Kovar		2	3	1	2.1
Cu-Diamond		4	3.5	8	4.4
Al-Si		8	10	4	8.0
Al-SiC		8	10	5	8.1
Al-Graphite		8	5.5	6	7.2

D.3.2. EMPHASIS ON SOLDER LAYER STRESS

Table D.12: Pairwise comparison of the criteria.

	Density	Solder Stress	Temperature
Density	1	1	3
Solder Stress	1	1	3
Temperature	1/3	1/3	1

$$w = \begin{bmatrix} 0.43 \\ 0.43 \\ 0.14 \end{bmatrix} \tag{D.4}$$

λ_{max} = 3
CI = 0
CR = 0

Table D.13: Trade-off table

h=5mm Material	Score	Density 0.43	Solder Stress 0.43	Temperature 0.14	Total
Cu		2	9	8	5.9
Al		9	4	5	6.3
Ti		7	4	1	4.9
Mg		9	3.5	2	5.7
Mo		1	3.5	4	2.5
Kovar		2	3	1	2.3
Cu-Diamond		4	3.5	8	4.3
Al-Si		8	10	4	8.3
Al-SiC		8	10	5	8.4
Al-Graphite		8	5.5	6	6.6

D.3.3. EMPHASIS ON TEMPERATURE

Table D.14: Pairwise comparison of the criteria.

	Density	Solder Stress	Temperature
Density	1	2	2
Solder Stress	1/2	1	1
Temperature	1/2	1	1

$$w = \begin{bmatrix} 0.50 \\ 0.25 \\ 0.25 \end{bmatrix} \tag{D.5}$$

$\lambda_{max} = 3$
CI = 0
CR = 0

Table D.15: Trade-off table

h=5mm Material	Score	Density 0.5	CTE Stress 0.25	T_comp 0.25	Total
Cu		2	9	8	5.3
Al		9	4	5	6.8
Ti		7	4	1	4.8
Mg		9	3.5	2	5.9
Mo		1	3.5	4	2.4
Kovar		2	3	1	2.0
Cu-Diamond		4	3.5	8	4.9
Al-Si		8	10	4	7.5
Al-SiC		8	10	5	7.8
Al-Graphite		8	5.5	6	6.9

D.4. SENSITIVITY ANALYSIS OF MANUFACTURING PROPERTIES AHP

This section contains the sensitivity analysis for the manufacturing properties. The selection criteria are; material properties, cost, availability, rework and risk. Because the material properties are already the most important criterion, there is no need to emphasis it even more. As long as the production cost and the lead time stay within the given margins, these criteria can be considered of minor performance. The sensitivity analysis is thus performed for two cases; more emphasis on rework and more emphasis on risk.

D.4.1. EMPHASIS ON REWORK

Table D.16: Pairwise comparison of the manufacturing criteria.

	Material properties	Cost	Availability	Rework	Risk
Material properties	1	8	3	2	5
Cost	1/8	1	1/4	1/3	1/2
Availability	1/3	3	1	1/2	2
Rework	1/2	4	2	1	3
Risk	1/5	2	1/2	1/3	1

The eigenvector of this matrix is equal to:

$$w = \begin{bmatrix} 0.45 \\ 0.06 \\ 0.15 \\ 0.25 \\ 0.09 \end{bmatrix} \tag{D.6}$$

λ_{max} = 5.059
CI = 0.0147
CR = 1.33%

D.4.2. EMPHASIS ON RISK

Table D.17: Pairwise comparison of the manufacturing criteria.

	Material properties	Cost	Availability	Rework	Risk
Material properties	1	8	3	3	4
Cost	1/8	1	1/3	1/3	1/3
Availability	1/3	3	1	1	1
Rework	1/3	3	1	1	1
Risk	1/4	3	1	1	1

The eigenvector of this matrix is equal to:

$$w = \begin{bmatrix} 0.48 \\ 0.05 \\ 0.16 \\ 0.17 \\ 0.14 \end{bmatrix} \tag{D.7}$$

λ_{max} = 5.0837
CI = 0.0209
CR = 1.89%

E

2-4 GHz Board Test Results

This appendix shows the measurement results of the thermocouples placed on the 2-4 GHz board. First, the location of the thermocouples is shown in figure E.1. This is followed by the measurement results at 1013 $mbar$ in table E.1 and at 20 $mbar$ in table E.2.

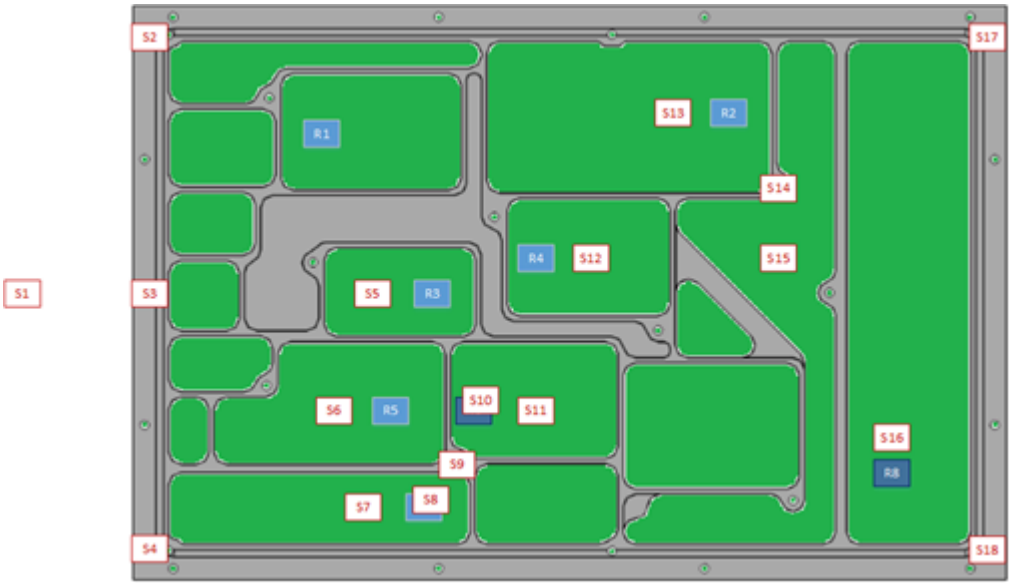

Figure E.1: The location of the thermocouples on the 2-4 GHz board.

Table E.1: Temperatures of the thermocouples at 1013 $mbar$.

Location	Model Temperature [$^{\circ}C$]	Measured Temperature [$^{\circ}C$]	Error [$^{\circ}C$]
S1	21.6	21.4	0.2
S2	23.3	24.8	-1.5
S3	23.4	25.3	-1.9
S4	23.7	26.3	-2.6
S5	30	32.6	-2.6
S6	28.6	31.9	-3.3
S7	27.7	32.3	-4.6
S8	35	38.8	-3.8
S9	30.5	33.1	-2.6
S10	40.6	46.2	-5.6
S11	32.8	34.9	-2.1
S12	30.9	33.9	-3
S13	31.2	33.2	-2
S14	30	32.2	-2.2
S15	30	32.7	-2.7
S16	42.3	47.2	-4.9
S17	29.7	30.8	-1.1
S18	31.3	32.5	-1.2

Table E.2: Temperatures of the thermocouples at 20 $mbar$.

Location	Model Temperature [$^{\circ}C$]	Measured Temperature [$^{\circ}C$]	Error [$^{\circ}C$]
S1	22.2	23.4	-1.2
S2	24.7	28.5	-3.8
S3	24.6	29.5	-4.9
S4	25.1	30.5	-5.4
S5	33.3	37.4	-4.1
S6	31.2	36.5	-5.3
S7	30.5	37.6	-7.1
S8	39.4	43.6	-4.2
S9	34.2	37.9	-3.7
S10	45.9	51.2	-5.3
S11	36.7	40	-3.3
S12	35.3	39.3	-4
S13	35.9	38.2	-2.3
S14	35	37.4	-2.4
S15	35.1	37.9	-2.8
S16	49.3	53	-3.7
S17	35	36.4	-1.4
S18	36.7	38.1	-1.4